Journal of
Materials Chemistry C

ROYAL SOCIETY
OF CHEMISTRY

PERSPECTIVE

View Article Online
View Journal | View Issue

Open Access Article. Published on 20 January 2025. Downloaded on 1/21/2026 10:55:07 PM.
This article is licensed under a Creative Commons Attribution-NonCommercial 3.0 Unported Licence.

Check for updates

Cite this: *J. Mater. Chem. C*, 2025, **13**, 3721

Received 10th November 2024,
Accepted 17th January 2025

DOI: 10.1039/d4tc04766d

rsc.li/materials-c

The intriguing case of cyclic triimidazole: an emerging scaffold for the preparation of multiemissive, bio-medical and hybrid inorganic–organic materials

Alessandra Forni, [a] Daniele Malpicci, [ab] Daniele Maver, [ab] Elena Lucenti [a] and Elena Cariati *[ab]

Among organic small molecules characterized by multifaceted behaviour, triimidazo[1,2-*a*:1′,2′-*c*:1″,2″-*e*][1,3,5]triazine, **TT**, having a triazinic central ring with three annelated imidazoles, represents a fascinating but still underinvestigated scaffold endowed with intriguing luminescence and coordination properties. Here we comprehensively gather studies, mainly conducted by our research group, on several fully organic or hybrid inorganic–organic **TTs** revealing their AIE, RTP, mechanochromic and excitation dependent photoluminescence behaviours. Preliminary applications of **TTs** in sensing and bio-medicine are also reported, opening avenues for further studies in these fields and widening the potentiality of **TT** and its derivatives. On the whole, the results shown here clearly demonstrate that cyclic triimidazole can be rightfully included in the toolbox of powerful scaffolds inspiring the preparation of multifunctional molecular materials.

1. Introduction

The engineering of organic small molecules characterized by multifaceted properties is certainly a longstanding research goal. In this regard, nitrogen-containing heterocyclic compounds represent an appealing class for different reasons: (i) they are important building blocks to generate bio-probes with significant therapeutic potential;[1–3] (ii) they can be used to obtain organic and hybrid inorganic–organic polymeric materials;[4–6] and (iii) they present structural features exploitable for the preparation of supramolecular assemblies through intermolecular interactions. In particular, several luminescent systems have been obtained by π–π stacking interactions and hydrogen or halogen bonds.[7–11]

Among different nitrogen-heterocycles, imidazoles and triazines represent versatile scaffolds, which have been used to develop several bioactive compounds with anticancer, antibacterial, antifungal, antitubercular, analgesic, and anti-HIV activities.[12–17] Moreover, imidazole and its derivatives have been frequently employed in the synthesis of metal compounds, *e.g.* numerous luminescent M(I, II) d^{10} complexes and coordination polymers (CPs), due to the electron-rich nature of the five-membered imidazole ring.[18–21] Besides, the triazine moiety with its three N atoms has been exploited to build molecules able to establish multiple supramolecular interactions resulting in rigidified structures with enhanced emissive features.[22–25] Importantly, triazine cores have also gained significant attention in the past few decades as building blocks for the preparation of covalent triazine frameworks (CTFs) as promising porous organic materials.[26–28]

In this regard, triimidazo[1,2-*a*:1′,2′-*c*:1″,2″-*e*][1,3,5]triazine or cyclic triimidazole (hereafter **TT**) represents an intriguing molecule formed by a triazinic central ring with three annelated imidazoles (see Scheme 1a). It possesses C_{3h} molecular symmetry and three nitrogen atoms available for coordination. While **TT** is known since 1973,[29] its properties and reactivity remained mainly unexplored until the recent publication of a convenient synthetic procedure.[30] This is the reason why studies on **TT** are still limited despite its promising potentialities as highlighted in the past few years mainly through investigations performed by our research group. Specifically, **TT** and a large family of its derivatives (**TTs**) have been prepared and characterized for their emissive and coordination features. The multicomponent fluorescence and phosphorescence behaviours of most **TTs** have been discovered but only preliminarily exploited for sensing and bioimaging.

In this perspective, after a brief overview of fused π-extended nitrogen rich cores exploited for the preparation of multifunctional materials, we focus on the **TT** family detailing the

---

[a] *Institute of Chemical Sciences and Technologies "Giulio Natta" (SCITEC) of CNR, via Golgi 19, 20133 Milano, Italy*

[b] *Department of Chemistry, Università degli Studi di Milano, via Golgi 19, 20133 Milano, Italy. E-mail: elena.cariati@unimi.it*

Open Access Article. Published on 20 January 2025. Downloaded on 1/21/2026 10:55:07 PM.
This article is licensed under a Creative Commons Attribution-NonCommercial 3.0 Unported Licence.

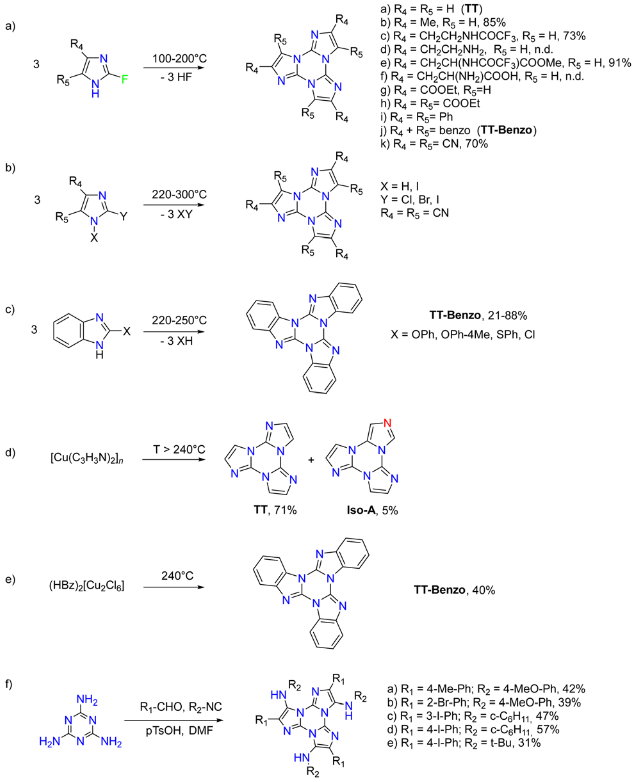

Scheme 1 Synthesis of **TT** derivatives.

synthetic procedures and the outstanding emissive features of the core itself and its many fully organic or hybrid inorganic–organic derivatives. Specifically, a deep photophysical investigation of **TT** functionalized with halogens, ethynyl, carboxyl and chromophoric (including pyrene, pyridines, carbazole and thiophene) groups has been conducted in previous works and summarized and rationalized here together with results obtained for selected hybrid metal compounds with **TTs** as ligands. Finally, an additional paragraph related to the use of **TTs** as sensors and biomolecules is included.

It is our belief that the present perspective could be a spring of inspiration for other researchers so that the potentiality of the **TT** scaffold could be more deeply exploited.

2. Overview of selected π-extended fused aza-heterocycles

In the past few decades, polycyclic aromatic hydrocarbons based on fused nitrogen-rich heterocycles have attracted increasing attention from the scientific community for their possible applications in various fields of supramolecular chemistry and materials science. The introduction of the nitrogen heteroatom in combination with the annealing of the aromatic rings has proven to be an efficacious strategy to prepare stable compounds. Fused aza-heterocycles are, in fact, characterized by a lower susceptibility to degradation through oxidation or dimerization in comparison with their nitrogen-free counterparts.[31] Consequently, the rigid, planar and electron deficient aromatic scaffolds of heptazine (Hz), quinazoline (Qn), hexaazatriphenylene (HAT) and benzotristriazine (BTT) have been exploited as cores for the preparation of promising functional materials, including covalent organic and metal–organic frameworks, to be used in different areas spanning from liquid crystals, n-type semiconductors, sensors, non-linear optical chromophores, gas absorption, energy storage, and catalysts to photo- and electro-luminescence (Fig. 1).[32–38]

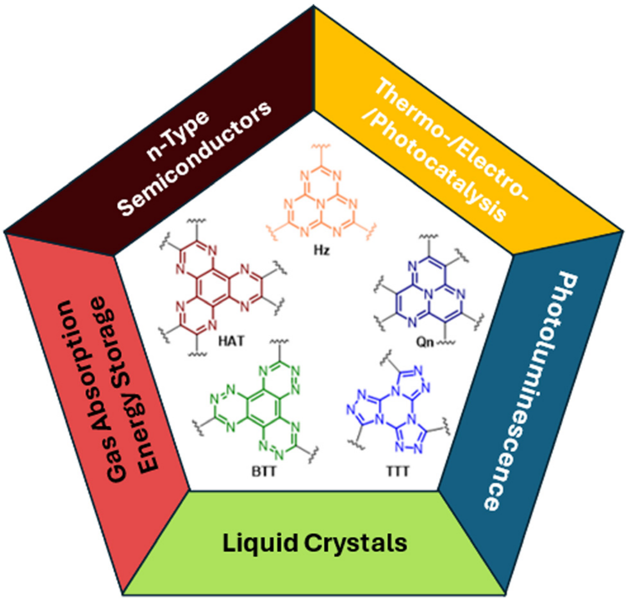

Fig. 1 Examples of π-extended fused aza-heterocycles and their main fields of applications.

In particular, among planar and rigid nitrogen-rich aromatic scaffolds, tris[1,2,4]triazolo[1,3,5]triazine (**TTT**) has recently emerged as a useful tecton for the preparation of liquid crystals and TADF (thermally activated delayed fluorescence) emitters. **TTT**, characterized by a central triazinic core with three annulated triazoles, with its nine sp^2 hybridized nitrogen atoms and C_3 symmetry, closely resembles cyclic triimidazole and therefore, in the present work, deserves closer inspection of the results so far obtained with its derivatives.

The first **TTT** described in the literature was pyroguanazole, synthesized in 1912 by thermal treatment of 3,5-diamino-1,2,4-triazole or guanazole.[39] However, since that early report, it remained mainly unexplored until 1961 when a seminal work by Huisgen and coworkers reported the synthesis of triphenyl-substituted **TTT** by reaction of cyanuric chloride with 1-phenyltetrazole.[40] This synthetic protocol was thoroughly explored later on, starting from the 2000s, when the ability of **TTTs** to self-assemble into columnar superstructures with mono-dimensional conducting properties was foreseen as a great opportunity to be exploited in molecular electronics and in the realization of discotic liquid crystals.[41–46] Interestingly, the strong coupling between lateral donor substituents and the central acceptor aromatic core together with the octupolar geometry endowed **TTTs** with linear and non-linear optical features (*i.e.* fluorescence and two-photon absorption).[47,48]

Open Access Article. Published on 20 January 2025. Downloaded on 1/21/2026 10:55:07 PM. This article is licensed under a Creative Commons Attribution-NonCommercial 3.0 Unported Licence.

Moreover, the thermal stability and highly ordered structures of discotic materials led to development of compounds characterized by high charge mobility together with light emission capability exploitable in electroluminescent devices.

Through appropriate functionalization of the central electron-acceptor core with donor groups (*e.g.*, phenoxazines, acridines, biacridines or carbazoles) the twisted D–A geometry of **TTTs** results in blue and green TADF emitters endowed, in some cases, with aggregation-induced enhanced emission (AIEE).[49–54] Furthermore, appropriately designed **TTT**-based dendrimers have been proposed as hot exciton materials to be used for the preparation of efficient and stable OLEDs.[55,56]

More recently, it has been found that the introduction of thiophene bridges in between bulky donor groups (di-3,6-*tert*-butyl-carbazole or 9,9-dimethyl-9,10-dihydroacridine) and the **TTT** acceptor core provides solutions with an impressive emissive behavior comprising delayed fluorescence (associated with triplet–triplet annihilation, TTA) and RTP. The latter has been justified by the positive effect of the bulky donor groups on inhibiting non-radiative decays from the triplet state, as confirmed by the similar lifetimes recorded in solution and in the solid state in the Zeonex matrix.[57]

Other interesting photoluminescence features have been observed for **TTTs** with a phenothiazine heterocycle as a donor functionality. Modulation of the donor strength and steric constraints through the incorporation of methyl groups at different positions of the emitter provided multifunctional materials exhibiting AIEE, dual-TADF, aggregation-induced delayed fluorescence (AIDF), and RTP characteristics. In addition, by appropriately choosing the polarity of the host matrix and by controlling the singlet–triplet energy gap, the possibility to switch between RTP and TADF processes has been demonstrated.[58]

3. The TT family

3.1 Synthetic procedures for TT and TTs

The first report on **TT** dates back to 1973 when the self-condensation at 373 K of 2-fluoro-imidazole into its cyclic trimer was reported.[29] Trimerization reactions were also successfully performed by using as starting materials 2-fluoro- and 2-chloro-imidazoles variously substituted in 4,5-positions or 1-iodo-2-X-4,5-dicyanoimidazoles (X = Cl, Br, I) (Scheme 1a and b).[59–62] In a similar way, thermolysis of 2-aryloxybenzimidazoles was reported for the preparation of tris(benzimidazo)-[1,2-*a*:1′,2′-*c*:1″,2″-*e*][1,3,5]triazine (**TT-Benzo**) (Scheme 1c).[63] An alternative and more effective synthetic route for the preparation on a multigram scale of **TT** and **TT-Benzo** was further proposed by exploiting solvent-free thermolysis of copper(II) imidazolates. In particular, treatment in vacuum of the blue polymorph of copper(II) diimidazolate $[Cu(C_3H_3N_2)_2]_n$ at temperatures above 513 K afforded **TT** together with, as the by-product in a 1 to 5 ratio, isomer **Iso-A** showing an imidazole ring with 1,5- instead of 1,2-annelation (see Scheme 1d).[30,64] Similarly, treatment at 513 K of bis-benzimidazolium hexachlorodicuprate(II) $(HBz)_2[Cu_2Cl_6]$ produced **TT-Benzo** in fairly good yields (see Scheme 1e).[65]

More recently, a multicomponent approach based on selective multiple Groebke–Blackburn–Bienaymé (GBB) reactions performed on the melamine substrate yielded novel hexasubstituted cyclic triimidazoles.[66,67] By appropriately choosing the isocyanide and aldehyde reactants, five different **TT**-based derivatives were easily isolated in fairly good yields (Scheme 1f). In the case of the halo-aryl substituted products, post-transformation into more complex tripodal scaffolds was further achieved by intramolecular Ullmann-type amination or multiple Suzuki–Miyaura cross-coupling reactions, the latter providing star-shaped compounds with nanometric dimensions.[66,67]

3.1.1 Haloderivatives. The introduction of one or multiple halogen atoms, X (X = Cl, Br, I), on the **TT** scaffold was investigated in order to address several issues including the preparation of derivatives suitable for further functionalization and the investigation of the effect of halogen atoms on **TT** photophysics (see later). It is, in fact, well known that phosphorescence may be positively affected by heavy halogen atoms due to strong SOC that facilitates singlet–triplet ISC. Chlorinated, brominated and iodinated triimidazole derivatives, hereinafter ***n*X** (*n* = 1, 2 and 3; X = Cl, Br and I) (see Scheme 2), were prepared by chlorination, bromination and iodination of **TT** under mild conditions by using *N*-chloro-, *N*-bromo- and *N*-iodo-succinimide (NXS), respectively, according to Scheme 2.[68–71]

Interestingly, the reactive positions in halogenation, as well as in all functionalization reactions of **TT** further described, are the chemically equivalent 3, 7 and 11 ones. Since halogenation through NXS is not specific and provides mixtures of products, a careful control of reaction conditions (NXS equivalents, solvent and addition of catalytic acid) and purification procedures were necessary to obtain **1-3X** in good yields.

1–3Cl were synthetized by mild chlorination of the **TT** scaffold with *N*-chlorosuccinimide (NCS).[68] Electrophilic chlorination is not a selective reaction and provides a mixture of mono-, di- and trisubstituted compounds in relative quantities related to the amount of NCS employed. To assess the best synthetic conditions, catalysts, solvents and NCS equivalents were screened. The isolation of **1–3Cl** in good yields (47%, 61% and 16%, respectively) was obtained by treating **TT** with NCS in acetonitrile or dioxane at room temperature with the addition of a protic acid such as trifluoroacetic or *p*-toluenesulfonic acid. The three compounds were isolated using chromatographic techniques and characterized by NMR and MS.

1–3Br were prepared by mild bromination using one, two or three equivalents of *N*-bromosuccinimide (NBS),

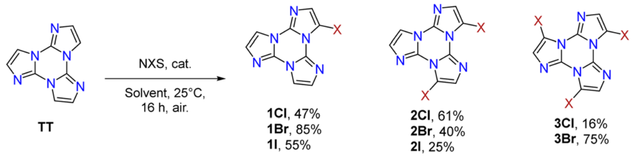

Scheme 2 Synthesis and chemical structures of **1–3X** (X = Cl, Br, I).

Open Access Article. Published on 20 January 2025. Downloaded on 1/21/2026 10:55:07 PM.
This article is licensed under a Creative Commons Attribution-NonCommercial 3.0 Unported Licence.

respectively.[69,70] The synthesis of **3Br** required an acetonitrile (ACN)/dichloromethane (DCM) mixture and the addition of trifluoroacetic acid as a catalyst. Products were purified by chromatography affording **1Br** and **3Br** in good yields (85 and 90%) while **2Br** was obtained in 40% yield together with **1Br** and **3Br** as by-products. NMR structural assignment of **1Br** and **2Br**, despite an extensive investigation comprising 1D (^{1}H and ^{13}C) and 2D (COSY, ^{1}H–^{13}C HSQC, ^{1}H–^{13}C HMBC, and ^{1}H–^{15}N-HMBC) experiments, was difficult due to the lack of crucial and diagnostic long-range correlations between quaternary carbon and proton signals. Implementation of the experimental results by DFT calculations highlighted $^{4}J_{H-C}$ correlations about twice the $^{3}J_{C-H}$ ones, allowing the proper chemical shift assignment for both compounds.[72]

Finally, mild electrophilic reaction of **TT** with *N*-iodosuccinimide (NIS) and catalytic amounts of trifluoroacetic acid in ACN provided **1I** and **2I**, both compounds being isolated and purified by chromatography and crystallization techniques.[71]

3.1.2 Overview of C–C and C–N bond formation. The isolation of **halo-TTs**, in particular the brominated ones, enabled the functionalization of the scaffold with different groups selected for their chemical, physical and photophysical properties. Pyrene and carbazole were chosen for their well-known chromophoric properties (*i.e.* a high quantum yield for the former and RTP features for the latter). The idea was to investigate the synergistic effect of **TT** and a photoluminescent moiety. Thiophene and pyridine were chosen for their versatile chemistry to get polymers for optoelectronic applications (the first) or ligands for metal complexation (the latter).

1–3Br were extensively used in Suzuki–Miyaura, Stille, Sonogashira and Ullmann cross-couplings mediated by Pd(0) or Cu(I) (see Scheme 3) with yields comparable to or slightly lower than those obtained from other brominated aryls (*e.g.* phenylbromide) using the same catalysts.[73–75] **1–3Br** react at high temperature, usually above 90 °C, otherwise leading to dehalogenation. The yields decrease, as expected, in polysubstitution reactions (values are in line with those reported for phenylbromide taken as a reference).[76,77]

Suzuki–Miyaura cross-coupling: **1–3Br** were reacted with commercially available boronic acids/esters such as pyrid-4-yl-,[78] pyren-1-yl-boronic acid[79,80] or 9*H*-carbazolyl-phenyl-,[81] 2-fluoropyrid-4-yl-,[82] 2,2′-bithiofen-5-yl-,[83] and 9-ethyl-9*H*-carbazole-3-boronic acid pinacol ester[84] in the presence of a Pd(0) precursor and a base, resulting in the isolation of different **TTs** (Scheme 4).

Stille cross-coupling reaction: in the same way, brominated **TTs** can react in Stille cross-coupling reaction. In this regard, **1–3Br** were reacted with pyrid-2-yl-,[78,85] thiophen-2-yl-,[83] and 4-hexylthiophen-2-yl[86] tributylstannyls in dry refluxing toluene for 16 h under an inert atmosphere (Scheme 5).

Ullmann-type cross-coupling reaction: moreover, **1Br** was reacted according to Ullmann-type cross-coupling reaction mediated by CuI with carbazole, affording **TT-(N)-Cz** in good yield (Scheme 6).[84]

Sonogashira cross-coupling reaction: halogenated **TTs** were also tested in Sonogashira type cross-coupling reactions. Recently, functionalization of **TT** with an ethynyl group was performed by following two different synthetic procedures using either **1Br** or **1I** as the starting material, both methods converging to **TT-CCH** (Scheme 7).[87]

Formylation reaction: formyl-**TTs** (**TT-(CHO)$_{1-3}$**) were prepared by direct formylation of the scaffold *via* a lithium salt intermediate followed by quenching with DMF.[78] The same synthetic route was exploited in the formylation of **TTPyr**,

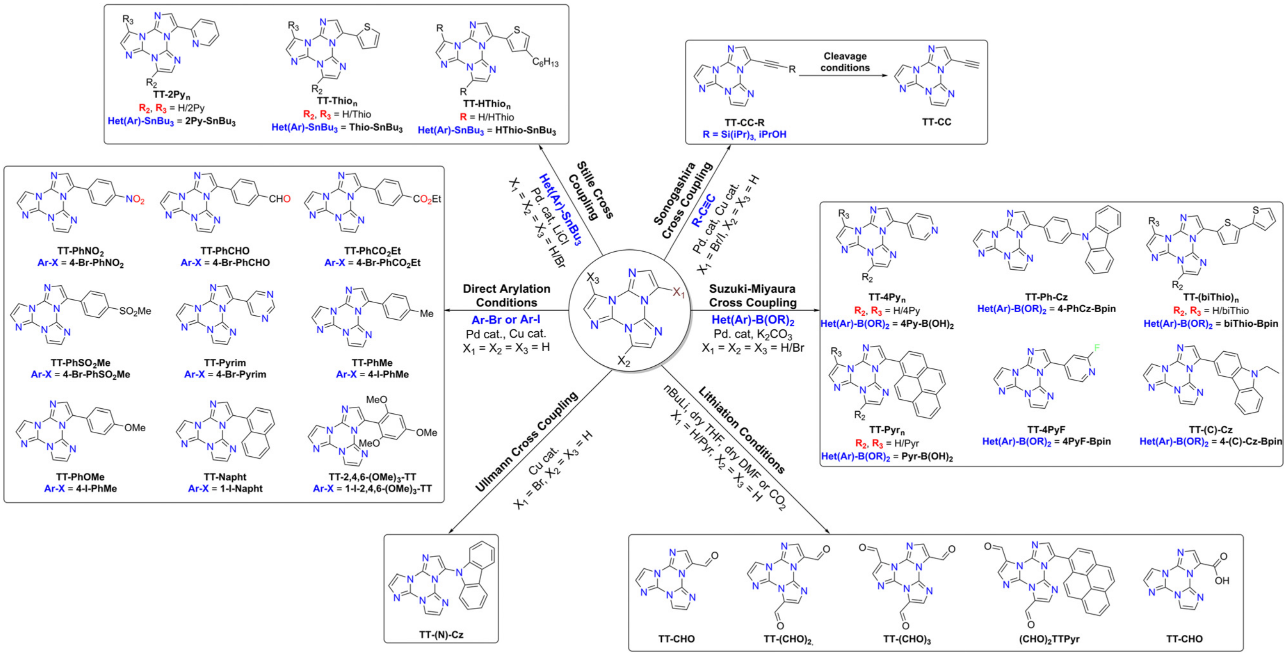

Scheme 3 Overview of C–C coupling products.

Open Access Article. Published on 20 January 2025. Downloaded on 1/21/2026 10:55:07 PM.
This article is licensed under a Creative Commons Attribution-NonCommercial 3.0 Unported Licence.

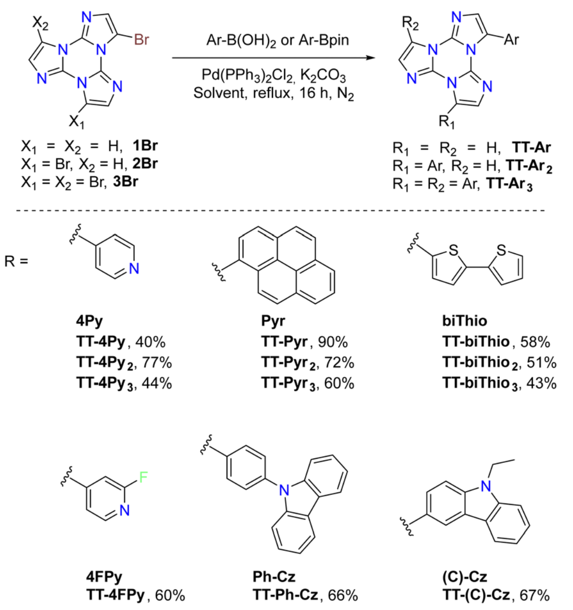

Scheme 4 Synthesis of **TT** derivatives by Suzuki–Miyaura cross-coupling.

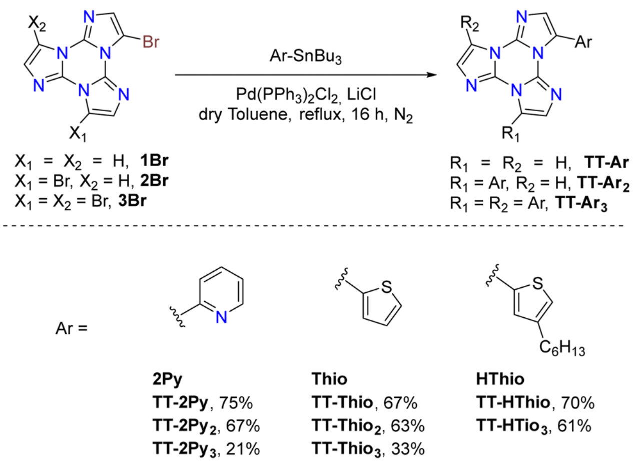

Scheme 5 Synthesis of **TT** derivatives by Stille cross-coupling.

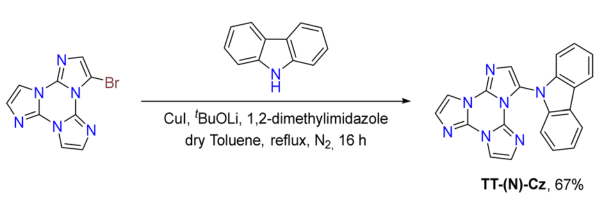

Scheme 6 Synthesis of **TT** derivatives by Ullmann-type cross-coupling.

resulting in the formation of the **$(CHO)_2$TT-Pyr** derivative, in which the two carbonyl groups are directly connected to the central triazinic core (Scheme 8).[88] Moreover, the **TT-COOH** ligand has been obtained through quenching of the lithium salt using CO_2.[89]

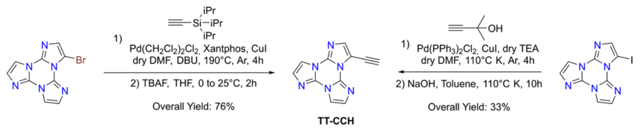

Scheme 7 Synthesis of **TT** derivatives by Sonogashira cross-coupling.

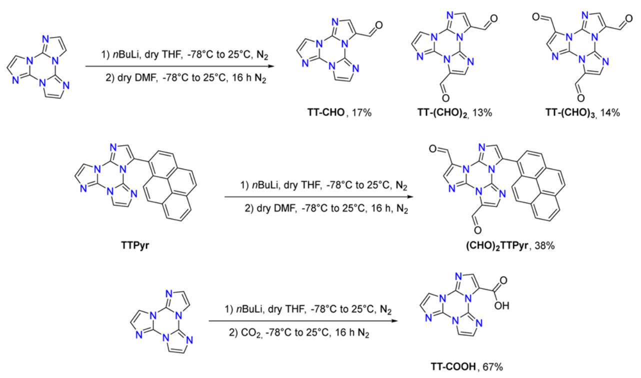

Scheme 8 Synthesis of **TT** derivatives by formylation.

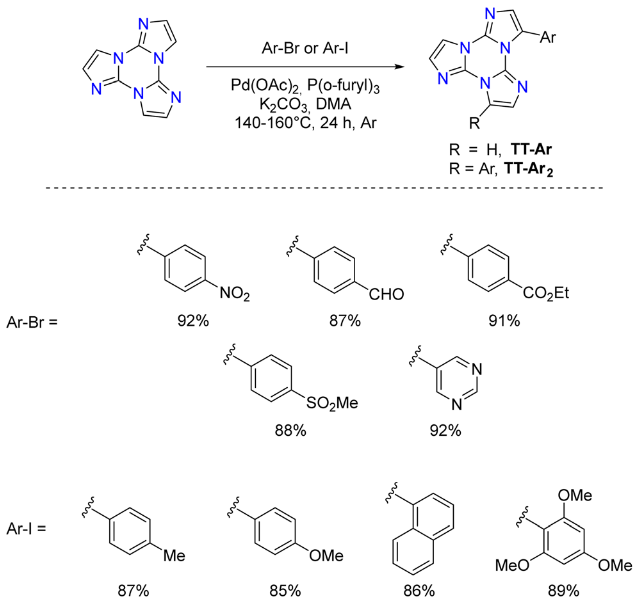

Scheme 9 Synthesis of **TT** derivatives by direct arylation.

Direct arylation: recently, a new synthetic approach based on direct and regioselective palladium-catalyzed C–H functionalization of the 3-position of the **TT** scaffold has been reported.[90] Optimization of the reaction conditions allowed achieving high conversion and selectivity with either electron-rich and electron-poor or sterically demanding (hetero)aryl halides (Scheme 9).

3.2 Electrochemical properties

In order to obtain a deeper insight into the structure/property relationship of **TTs** (Scheme 10), a systematic cyclic

Open Access Article. Published on 20 January 2025. Downloaded on 1/21/2026 10:55:07 PM. This article is licensed under a Creative Commons Attribution-NonCommercial 3.0 Unported Licence.

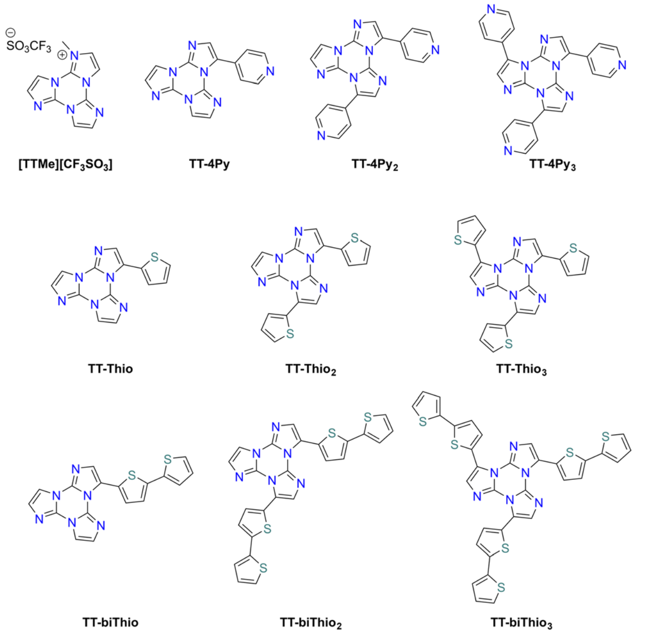

Scheme 10 Chemical structures of **[TTMe][CF$_3$SO$_3$]**, **TT-4Py$_{1-3}$**, **TT-Thio$_{1-3}$** and **TT-biThio$_{1-3}$**.

voltammetry investigation was performed.[83,91] **TT** is characterized by little electrochemical activity, with first oxidation and first reduction requiring extreme potentials, close to the DMF potential window limits, and with the three imidazole units behaving as three nearly independent redox sites. On the other hand, **Iso-A** is slightly more reactive, due to the electron-rich nature of the 1,5-annelated ring, which undergoes first oxidation at a milder potential, while reduction, centred on the remaining two almost equivalent 1,2-annelated moieties, is similar to that of **TT**. Methylation of one nitrogen atom of the imidazolic ring in **[TTMe][CF$_3$SO$_3$]** resulted in a significant positive shift of the first reduction potential, due to the electron poor nature of the alkylated N site. In **1–3Br**, the electrochemical cleavage of the C–X bond is only slightly influenced by the number of halogens. These findings further strengthened the hypothesis that each imidazole unit in the cyclic trimer acts as an almost independent redox site, with very poor heteroannular aromaticity.[91]

Comparison of the electrochemical activity of **TT** substituted with a pyridine moiety attached to the *ortho* (**TT-2Py**) or *para* (**TT-4Py**) position revealed that the effect of the linking position of the pyridyl group is more effective on the HOMO or oxidation process (mostly centred on **TT**) than the LUMO or reduction (mostly pyridine-centred). In the case of **TT-2Py**, a slight negative shift of the first oxidation potential was observed, probably due to a conjugation, rather than the inductive effect, between the **TT** core and the 2Py moiety.

On the other hand, a remarkable positive shift of both reduction and oxidation processes was observed for **TT-4Py**. As a result, both derivatives display a HOMO–LUMO gap dramatically decreased with respect to **TT**, although significantly smaller for **TT-2Py** than for **TT-4Py**. The introduction of multiple 4Py moieties in **TT-4Py$_2$** and **TT-4Py$_3$** favoured the reduction process, as pointed out by the less negative values with increasing number of pyridine substituents (**TT-4Py$_n$** −2.64/−2.60/−2.54 V for n = 1/2/3, respectively).

In the case of a more electron rich substituent, as the thiophene moiety in the **TT-Thio$_{1-3}$** series, the **TT** core is endowed with more favourable first oxidation and first reduction potentials and a narrower HOMO–LUMO gap. The derivatives are not only significantly electron richer than the pyridine-substituted ones, but display also a more effective conjugation efficiency, as confirmed by DFT calculations disclosing the significant involvement of the thiophene terminals in both HOMOs and LUMOs. However, no electrochemical coupling reactions have been observed for **TT-Thio$_{1-3}$**, probably due to the fact that the thiophene pendants are too small in comparison with the **TT** core.

In order to efficiently promote coupling and formation of an electroactive film on the electrode surface, the bithiophene **TT-biThio$_{1-3}$** series was investigated, revealing smaller energy gaps than their thiophene counterparts, with the HOMO and the LUMO mainly located on the bithiophene moiety. Electrodeposition experiments in monofunctionalized **TT-biThio** solutions, despite the formation of an electroactive product on the electrode surface, did not provide evidence of active film growth, probably due to the formation of a dimeric layer on the electrode surface. On the other hand, di- and trisubstituted monomers **TT-biThio$_{2-3}$** produced fast and regular growth of electroactive films on the electrode surface upon potential cycling around their first oxidation peak (Fig. 2). These promising results on the fast and reproducible oxidative electrodeposition of oligo/polymer films based on alternate **TT** and tetrathiophene units constitute an attractive springboard for the development of highly electroactive **TT**-based materials.[83]

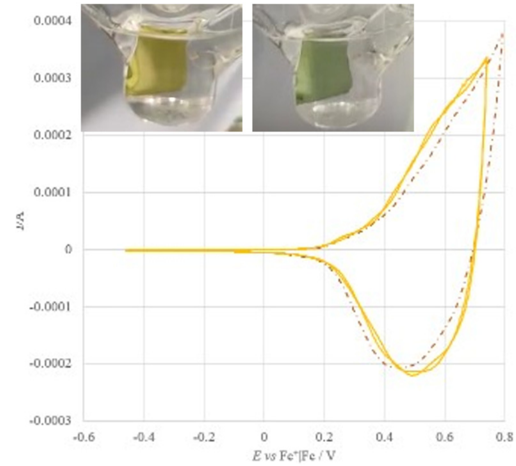

Fig. 2 First and fourth stability cycles in monomer-free solution and electrochromism of **[TT-biThio$_2$]$_n$** films electrochemically formed on the ITO electrode. Reproduced from ref. 83 under the terms of the Creative Commons CC BY license. Copyright 2023, Published by Elsevier Ltd.

Open Access Article. Published on 20 January 2025. Downloaded on 1/21/2026 10:55:07 PM.
This article is licensed under a Creative Commons Attribution-NonCommercial 3.0 Unported Licence.

3.3 Photophysical and structural properties

Single component materials characterized by rich emissive behaviour including synergic aggregation induced emissive (AIE) and room temperature long lived (room temperature phosphorescence, RTP) features are receiving growing attention from the scientific community due to the benefits they offer in different fields (*e.g.* bioimaging,[92–95] anti-counterfeiting,[96–100] and displays[101]). Long lived RTP can be achieved through organic compounds but phosphorescence is traditionally considered as the exclusive realm of heavy metal complexes. In fact, inter-system crossing (ISC) and, consequently, phosphorescence lifetime, depend on spin–orbit coupling (SOC), which is large in the presence of heavy atoms. However, through appropriate molecular design and supramolecular engineering, pure organic long-lived phosphors have become numerous and have been already tested for different applications.[102–104]

Many **TTs** revealed a rich photophysical behaviour comprising multiple fluorescence and phosphorescence of molecular and supramolecular origins, anti-Kasha emissions and excitation dependent photoluminescence (see the following). Multiple emissions derived from molecular electronic levels can originate from the anti-Kasha mechanism, that is, radiative deactivation from high energy S_n (or T_n) states, or from the presence of different conformers either in the ground or in the excited states. While anti-Kasha behaviour is frequently associated with a large S_1–S_2 energy gap and a high S_0–S_2 oscillator strength (*f*), it can also occur in systems having a smaller S_1–S_2 gap, but S_n–S_1 internal conversion (IC) prohibited on symmetry grounds.[105] Examples of both anti-Kasha mechanisms have been observed for **TTs** (see simplified mechanisms in Fig. 3).

The reported excitation dependent behavior of many **TTs** can be explained as the selective suppression of stronger signals (usually fast components at high energy) allowing the monitoring of the weaker ones (typically red shifted phosphorescence) by low energy excitation to singlets of aggregated species or of different conformers or, less frequently, by direct triplet population. Moreover, halogenated derivatives of **TT** represent remarkable examples of excitation dependent deactivation paths. These systems, in fact, display phosphorescence from T_1 only when excited at sufficiently high energy to populate an S_n from which ISC to T_n is favorable. Subsequent IC to T_1 results in the observed phosphorescence (see later).

3.3.1 The protoype: cyclic triimidazole. The **TT** prototype shows crystallization induced (CIE) and mechanochromic emissive behaviour, together with room temperature ultralong phosphorescence (RTUP) under ambient conditions.[106] More specifically, dilute DCM solutions of **TT** display at 298 K a very weak absorption at 285 nm, with a first sizable peak at about 220 nm, and a hardly discernible emission (at about 400 nm). Based on DFT/TDDFT calculations, the high (ideally C_{3h}) symmetry of the compound is responsible for 'silent' (*i.e.* characterized by oscillator strength, *f*, equal to zero) low-energy singlet states. The compound crystallizes in the $P\bar{1}$ space group with significant distortion from the expected C_{3h} symmetry, a result of the establishment of strong intermolecular π–π stacking interactions.[30] **TT** molecules, in fact, pack in an alternating AB face-to-face antiparallel fashion forming columnar aggregates where relatively electron-rich and electron-poor regions approach each other (Fig. 4). This structural pattern represents a distinctive feature of the **TT** scaffold being observed, with obvious variations in relative distances and orientations, in almost all **TTs**, as shown below.

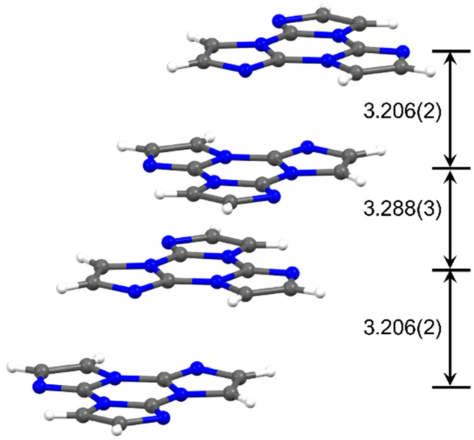

Fig. 4 Crystal packing of **TT** exhibiting AB stacking arrangement with distances between molecular planes given in Å.

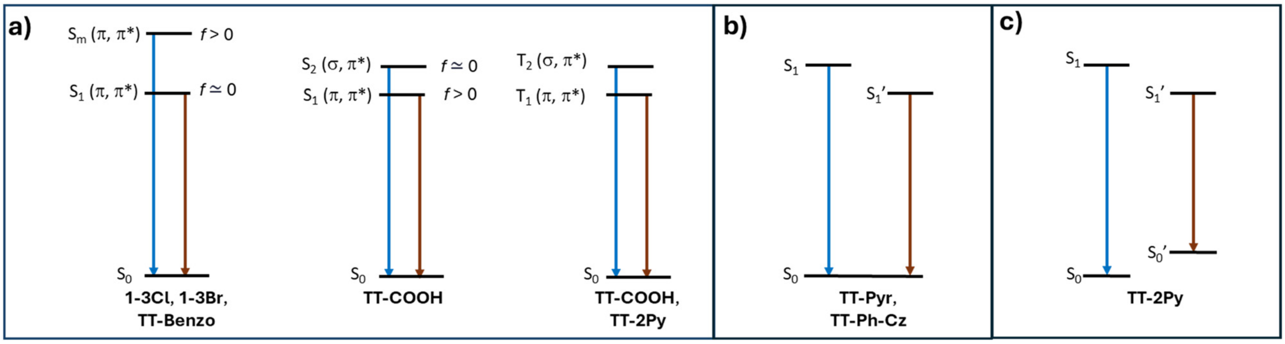

Fig. 3 Simplified energy level for organic **TTs** displaying anti-Kasha behavior (a) and multiple emissions from different excited (b) or ground (c) state conformers.

Open Access Article. Published on 20 January 2025. Downloaded on 1/21/2026 10:55:07 PM.
This article is licensed under a Creative Commons Attribution-NonCommercial 3.0 Unported Licence.

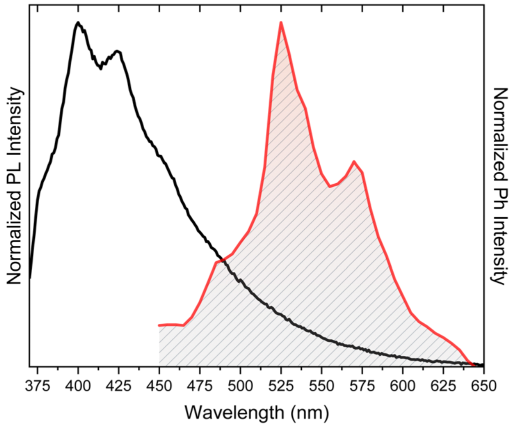

Fig. 5 Photoluminescence (PL, black line, λ_{exc} = 350 nm) and phosphorescence (red line, time delay 472 ms, λ_{exc} = 374 nm) of **TT** crystals at 298 K.

Crystals of **TT** display at 298 K an intense vibrationally resolved fluorescence at 400 and 424 nm with a RTUP (lifetime, τ, $\cong 1$ s) low energy tail (overall quantum yield, Φ, equal to 30%), which was well disclosed in the delayed spectrum where vibrationally resolved peaks at 525 and 570 nm become visible (Fig. 5). After grinding in a mortar, a loss of the vibronic components of both prompt and RTUP emissions was observed together with a quantum efficiency reduction from 30% to 22%.

Geometry optimizations based on either DFT calculations on dimeric and tetrameric aggregates[106] or hybrid QM/MM calculations[107] highlighted the role of π–π interactions in distorting **TT** from the C_{3h} symmetry, as experimentally observed. It was also evidenced[107] that low- and middle-frequency normal modes, that is, the triazine/imidazole twisting and stretching motions, respectively, are effective only for the isolated (*in vacuo* or DCM solution) molecule, while they are suppressed for a molecule restricted in a cluster. These restrictions result in a strong increase of the quantum yield and are therefore responsible for the observed AIE behaviour of **TT**. The phosphorescence efficiency in the solid state was explained by the strong decrease in the S_1–T_1 energy gap when going from the isolated molecule to aggregates[106,107] and by a remarkable intersystem crossing (k_{ISC}) and negligible reverse intersystem crossing (k_{rISC}) rates,[107] in agreement with the lack of delayed fluorescence.

The π–π interactions observed in many **TTs** are therefore expected to be relevant in affecting their photophysics. As a further proof, many of them, including **TT** itself, display mechanochromic features (see the following and Table 3).

These results, in agreement with previous reports on the active role played by H-aggregation in activating RTUP,[108,109] were further confirmed by investigation of the photophysics of **Iso-A**, the isomer of **TT** having one imidazole ring with 1,5- instead of 1,2-annelation. This compound, crystallizing in the $P2_1/c$ space group, is characterized by CIE behaviour, being slightly emissive in solution at 298 K (in DCM, Φ = 2.8%) but quite so in crystals due to a strong fluorescence at about 415 nm (Φ = 13%).[106] The absence of a long-lived component was confirmed also at 77 K. Its single crystal XRD analysis revealed aggregation of π–π stacked ribbons formed by dimeric units interconnected through cyclic C–H···N hydrogen bonds (HBs) and joined by co-crystallized water molecules. Weaker π–π interactions are suggested by the greater slippage of the parallel-packed columns and longer distance between centroids of the triazinic rings when compared to **TT**, in agreement with the lack of the ultralong emission component.

Owing to its inherent asymmetry associated with the presence of nitrogen atoms, **TT** is a prochiral molecule and its deposition on a surface generates two enantiomers.[110] The two are stabilized by π–metal interaction and their interconversion is not possible since it would require flipping the molecule out of plane by 180°. Along the surface plane, **TT** self-assembles through symmetric HB pairing of its left- (*S*) or right-turning (*R*) enantiomers, giving rise to spontaneously resolved two-dimensional hexameric networks consisting exclusively of *S*- (or *R*-) enantiomers (Fig. 6 top), as experimentally observed for **TT** deposited on a Ag(111) substrate.[110] The heterochiral assembly, though possible, was predicted by DFT calculations to be less stable than the homochiral one. STM images revealed

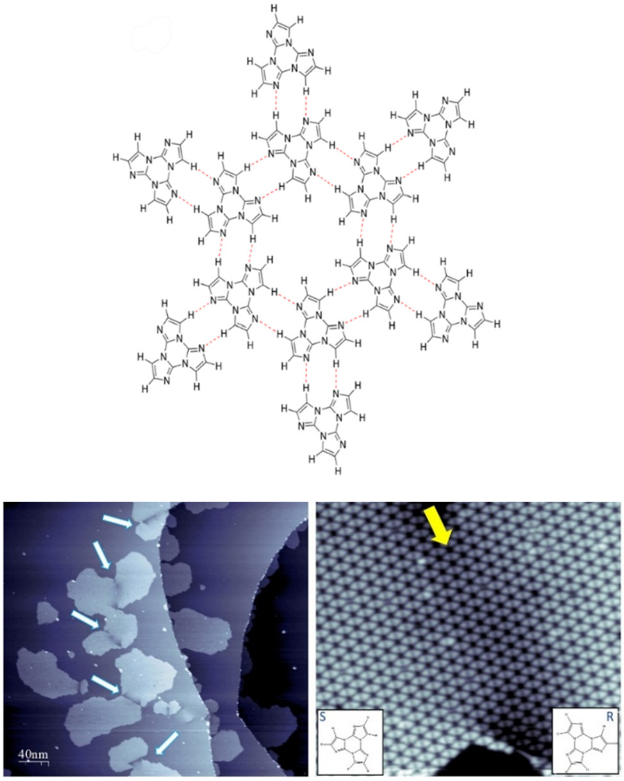

Fig. 6 Top: fragment of a model for the energetically most favorable homochiral 2D assembly of **TT** (the *S*-enantiomers are shown). Bottom: STM images of the nanoporous 2D networks formed by deposition of **TT** molecules on Ag(111) showing the kidney-shaped islands formed by **TT** (left, 400 × 400 nm, 1 V, 20 pA image) and one specific interface zone between two different domains of the hexagonal network (right, 40 × 40 nm, 1 V, 40 pA image). Adapted with permission from ref. 110 under the terms of the Creative Commons CC BY license. Copyright 2023, American Chemical Society.

Open Access Article. Published on 20 January 2025. Downloaded on 1/21/2026 10:55:07 PM. This article is licensed under a Creative Commons Attribution-NonCommercial 3.0 Unported Licence.

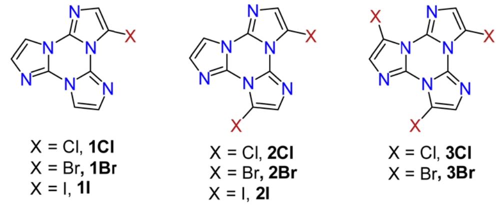

Scheme 11 Chemical structure of ***n*X**.

the presence of kidney-shaped enantiomeric islands, consisting of hexagonal porous networks of **TT** on the metal surface separated by a dark region, which was associated with a defective zone where *RR* islands 'capture' *S* enantiomers (and *vice versa*) during the deposition process (Fig. 6 bottom).

3.3.2 Halo-derivatives. The functionalization of **TT** with halogens (Scheme 11) greatly enriched the photophysical behaviour thanks to both molecular mechanisms and aggregation induced phenomena related to intermolecular interactions resulting in new emissive states.

In fact, **1–3X** display a quite complex, excitation dependent photoluminescence with emissions including dual fluorescence, molecular phosphorescence and supramolecular RTP and RTUP covering a wide portion of the visible region.[68–71]

3.3.2a Chlorine derivatives. Dilute DCM solutions of **1–3Cl** display at 298 K absorption bands at the wavelength below 300 nm and hardly discernible emissions ($\Phi < 1\%$) whose low quantum yield represented an impediment for the full interpretation of the molecular properties in solution.

1–3Cl crystallize in the $P\bar{1}$, $C2/c$ and $P2_1/c$ space groups, where molecules form hydrogen bonded corrugated layers, which stack in a slipped manner, evidencing the presence of π–π stacking interactions between **TT** units and, only for **3Cl**, very short ($r_{\mathrm{Cl}\cdots\mathrm{N}}$ = 3.014 and 3.151 Å) halogen bonds (XB) corresponding to 8.7 and 4.5% shortening with respect to the sum of the vdW (van der Waals) radii.

Crystals of **1–3Cl** are characterized by multiple, excitation dependent emissive features (Φ of about 24, 12 and 10% respectively) comprising dual fluorescence (a high energy component, HEF, in the 330–350 interval, and a low energy one, LEF, in the 350–400 nm portion of the spectrum) and triple phosphorescence (HEP 405–440 nm, MEP 480–550 nm and LEP 550–560 nm) with the lowest energy contribution (LEP) visible only at 77 K (see Fig. 7 and Table 3).

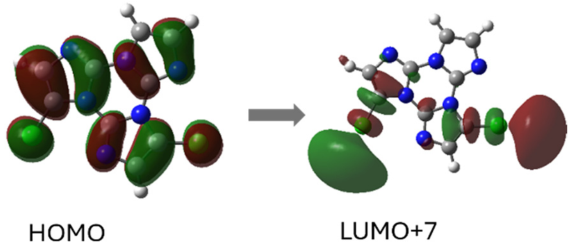

Fig. 8 Main molecular orbitals involved in the (π,σ*) T^{σ} state of **2Cl** (isosurface value: 0.02).

Through spectroscopic, structural and computational analyses, HEF, LEF, HEP and LEP were assigned to excited states of molecular origin while MEP was interpreted as derived from aggregated species. More specifically, HEF corresponds to radiative deactivation from a high energy singlet level (S_n) of (π,π*) character and large oscillator strength, while an S_1 state of (π,π*) character and much lower energy and oscillator strength is responsible for LEF. Altogether these features result in the observed anti-Kasha behaviour. Regarding the three phosphorescence types, HEP was correlated to T_1 of (π,π*) character, while LEP to high energy triplets of (π,σ*) character (T^{σ}, Fig. 8). Aggregation induced MEP, whose intensity increases by increasing the crystalline grade of the samples and the strength of π–π interactions in the crystal structure (intensity increasing in the order: **1Cl** < **3Cl** ≅ **2Cl**), was assigned to **TT** stacking interactions.

3.3.2b Bromine derivatives. Dilute DCM solutions of **1–3Br** display at 298 K a very sharp absorption band (at 230, 235 and 245 nm, respectively) with a low-energy tail in the 250–280 nm range. The emission spectra comprise a weak fluorescence (with maxima at 328, 380 and 370 nm, respectively), with Φ equal to 3% for **1Br** and almost vanishing for **2Br** and **3Br.** At 77 K, however, a very intense and broad phosphorescence in the

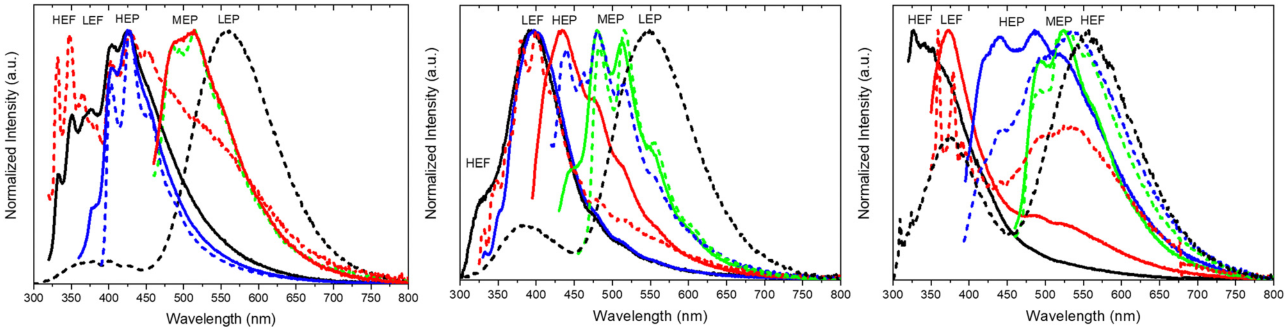

Fig. 7 Normalized PL emission spectra of **1–3Cl** crystals at 298 K (full lines) and 77 K (dashed lines). Left **1Cl**, 298 K: λ_{exc} = 300 nm (black), λ_{exc} = 340 nm (blue) and λ_{exc} = 440 nm (red). 77 K: λ_{exc} = 280 nm (black), λ_{exc} = 300 nm (red), λ_{exc} = 370 nm (blue) and λ_{exc} = 440 nm (green). Middle **2Cl**, 298 K: λ_{exc} = 280 nm (black), λ_{exc} = 308 nm (blue), λ_{exc} = 375 nm (red) and λ_{exc} = 413 nm (green). 77 K: λ_{exc} = 280 nm (black), λ_{exc} = 308 nm (red), λ_{exc} = 400 nm (blue) and λ_{exc} = 434 nm (green). Right **3Cl**, 298 K: λ_{exc} = 300 nm (black), λ_{exc} = 330 nm (red), λ_{exc} = 374 nm (blue) and λ_{exc} = 440 nm (green). 77 K: λ_{exc} = 280 nm (black), λ_{exc} = 330 nm (red), λ_{exc} = 373 nm (blue) and λ_{exc} = 440 nm (green).

Open Access Article. Published on 20 January 2025. Downloaded on 1/21/2026 10:55:07 PM.
This article is licensed under a Creative Commons Attribution-NonCommercial 3.0 Unported Licence.

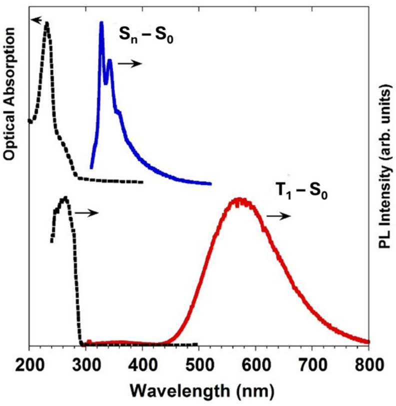

Fig. 9 **1Br** in DCM (10^{-4} M): top: absorption (black dotted line) and PL emission (λ_{exc} = 280 nm; blue solid line) at 298 K. Bottom: excitation profile (λ_{em} = 580 nm; black dotted line) and PL emission (λ_{exc} = 280 nm; red solid line) at 77 K. Adapted with permission from ref. 70. Copyright 2017, John Wiley and Sons.

570–590 nm range dominates the spectra by exciting below 280 nm (see Fig. 9 for **1Br**).

On the basis of DFT and TDDFT calculations, the RT emission was assigned, according to an anti-Kasha mechanism, to a high energy S_n state of (π,π*) character, while the phosphorescence observed at 77 K was explained by the presence of high energy ^{3}(σ,σ*) and, only for **3Br**, ^{3}(σ,π*) levels, which facilitate an efficient ISC (by both El Sayed and heavy atom effects) from the closest S'_n level, followed by IC to T_1. By exciting at longer wavelengths, in fact, the appropriate high energy S'_n level cannot be populated and only fluorescence from S_n was observed.

1–3Br crystallize in the $P2_1/c$, $P\bar{1}$ and $P2_1/c$ space groups respectively, forming π-stacked arrangements of dimeric (**3Br**) or columnar (**1Br** and **2Br**) **TT** units (see Fig. 10) with π–π stacking interactions' strength in the order **2Br** > **3Br** > **1Br**.

The structures of **2Br** and **3Br** highlight the presence of Br···Br XBs with formation of tetrameric Br_4 (**2Br**, see Fig. 10 centre) and trimeric Br_3 (**3Br**) units. The centrosymmetric Br_4 synthon (**2Br**) is characterized by high rigidity, as evidenced by both its approximate coplanarity and Br···Br distances 4 and 1% shorter than two times the bromine vdW radius. In the Br_3 unit (**3Br**), instead, only two molecules have close Br···Br contact (3% shortening), while the third one is rather far from the other two and significantly out from their ls (least squares) plane, indicating a less stable XB supramolecular aggregation.

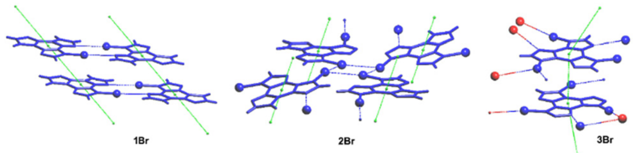

Fig. 10 Views of the π–π stacking in **1–3Br**; Br atoms are shown as spheres and XB interactions are highlighted by blue dashed lines. Red spheres in **3Br** refer to atoms belonging to different layers. Reproduced with permission from ref. 69. Copyright 2018, John Wiley and Sons.

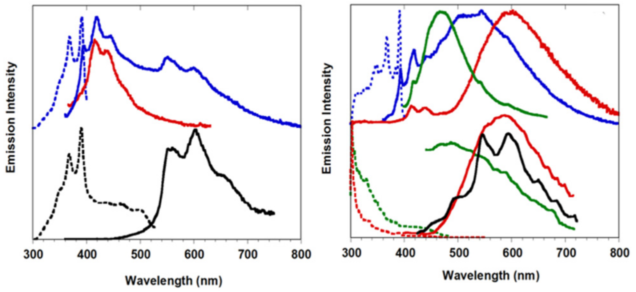

Fig. 11 Powders of **3Br** left: at 298 K. Top: Prompt emission (λ_{exc} = 280 nm, red solid line; λ_{exc} = 340 nm, blue solid line) and excitation profiles (λ_{em} = 420 nm, dashed blue line). Bottom: Delayed emission (λ_{exc} = 340 nm, 1 ms delay, window 50 ms; black solid line) and excitation profiles (λ_{em} = 550 nm, dotted black line). Right: at 77 K. Top: prompt emission (λ_{exc} = 280 nm, red solid line; λ_{exc} = 340 nm, blue solid line; λ_{exc} = 385 nm, green solid line) and excitation profiles (λ_{em} = 420 nm, dotted blue line). Bottom: delayed emission λ_{exc} = 360 nm, 100 μs delay, window 500 μs, red solid line; λ_{exc} = 385 nm, 100 μs delay, window 500 μs, green solid line; λ_{exc} = 385 nm, 5 ms delay, window 10 ms, black solid line) and excitation profiles (λ_{em} = 523 nm, dotted green line; λ_{em} = 600 nm, dotted red line). Adapted with permission from ref. 69. Copyright 2018, John Wiley and Sons.

Crystals of **1–3Br** display excitation dependent multicomponent spectra ($\Phi < 0.1$ for **1Br** and **3Br** and about 14% for **2Br**) including the S_n–S_0 emission, HEF, only observed in solution at RT, with maxima in the 330–440 nm interval. In addition, in **1Br** and **3Br**, the S_1–S_0 fluorescence LEF (with maxima in the 430–530 nm interval) is activated owing to distorting packing forces that reduce the symmetry of the molecular π-electron system (see Fig. 11 for **3Br**), resulting in dual fluorescence. The broad long-lived component detected at 470 nm for **2Br** at 298 K and at 490 nm for **3Br** at 77 K was ascribed to the extrinsic heavy atom effect caused by the bromine atom in the Br···Br XB motifs (the Br_4 cyclic units in **2Br** and the Br_3 cyclic units in **3Br**). The structured RTUP (at about 550–650 nm), observed in the emission spectra of powders of **2Br** and **3Br** (see Fig. 11 for **3Br**), was associated with the presence of stacking interactions among **TT** units. This RTUP cannot be totally excluded even for **1Br** since the crystallinity degree and the crystal size of the examined samples may play a role in the relative intensity of phosphorescence emissions. Finally, the three compounds display at 77 K and upon excitation at short wavelengths (280 nm) the strong phosphorescence (at 573, 558 and 590 nm for **1Br**, **2Br** and **3Br**, respectively) observed also in the frozen solutions and therefore assigned to molecular features.

3.3.2c **Iodine derivatives.**

DCM solutions of **1I** display an absorption band at about 240 nm with a tail in the 250–270 nm range and no emission at 298 K. At 77 K, a weak emission at about 420 nm, ascribed to deactivation from S_1, appears in the spectrum by exciting at low energy (λ_{exc} = 340 nm, see Fig. 12) while, at high energy excitation (below 300 nm), an intense, broad phosphorescence (630 nm) dominates the spectrum. Such molecular phosphorescence is largely red-shifted (by about 50 nm) and its lifetime is one order of magnitude shorter than those of **1–3Br** due to the enhanced heavy atom effect of

Open Access Article. Published on 20 January 2025. Downloaded on 1/21/2026 10:55:07 PM.
This article is licensed under a Creative Commons Attribution-NonCommercial 3.0 Unported Licence.

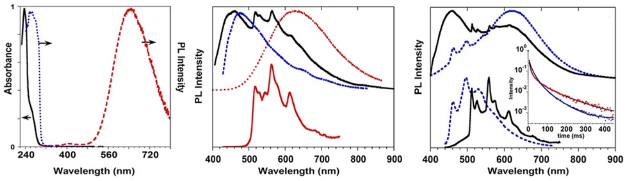

Fig. 12 Left: **1I** in DCM: absorption spectrum at 298 K (black solid); PL emission and excitation spectra at 77 K (λ_{exc} = 280 nm, red dashed; λ_{em} = 648 nm, blue dotted); centre: emission spectra of **1I** crystals at 298 K: top: PL at λ_{exc} = 300 nm (red dotted), λ_{exc} = 370 nm (black solid), λ_{exc} = 415 nm (blue dashed); bottom: phosphorescence spectrum (λ_{exc} = 370 nm, delay 50 ms, window 200 ms, red solid); right: emission spectra of **1I** crystals at 77 K. Top: PL at λ_{exc} = 320 nm (blue dotted), λ_{exc} = 370 nm (black solid); bottom: phosphorescence spectra at λ_{exc} = 320 nm (delay 10 ms, window 50 ms, blue dotted) and λ_{exc} = 370 nm (delay 50 ms, window 200 ms, black solid). Phosphorescence decays at λ_{em} = 460 nm (λ_{exc} = 320 nm, blue points) and λ_{em} = 558 nm (λ_{exc} = 370 nm, red points) with their three-exponential fits (black lines) are shown in the inset. Adapted with permission from ref. 71. Copyright 2019, John Wiley and Sons.

iodine with respect to bromine, which makes SOC even more efficient. Accordingly, the easier singlet-to-triplet and triplet-to-singlet ISCs explain, respectively, the lack of RT fluorescence and the faster phosphorescence of **1I**. Based on TDDFT calculations, the latter emission was explained, similarly to **1-3Br**, by the presence of a $^3(\pi,\sigma^*)$ state close to a high energy singlet state of $^1(\pi,\pi^*)$ character, allowing easy singlet-to-triplet ISC and then phosphorescence from a lower energy triplet state. The reduced heavy atom effect of chlorine in **1-3Cl** justifies the lack of such phosphorescence in their dilute solutions.

1I and **2I** crystallize in the $C2/c$ and $P\bar{1}$ space groups, respectively, where XB and π–π stacking interactions act in a cooperative way. In **1I**, non-equivalent I···N XB bonds ($r_{\text{I}\cdots\text{N}}$ = 2.878 and 3.020 Å, corresponding to 18 and 14% shortening with respect to the sum of the vdW radii) are established on both sides of the molecule, giving rise to helicoidal chains (see Fig. 13). Four halogen bonded chains are intervolved along the helix axis, so that the pitch of the helix, 16.388 Å long, comprises four molecules with the interplanar distance (3.309 Å) facilitating strong π–π interactions. The crystal structure of **2I** is isomorphous with that of **2Br**, where molecules form tetrameric I···I XB cyclic units, I_4, slightly more rigid than the Br_4 ones. The I···I distances, 3.717 and 3.780 Å, are in fact 6 and 5% shorter than two times the iodine vdW radius, to be compared with 4 and 1% shortening observed in the Br_4 unit.

Crystals of **1I** and **2I** show at room temperature quite similar excitation dependent emissive features (Φ < 0.1 and 7%, respectively). In particular, upon low energy excitation, **1I** and **2I** display a broad fluorescence (at 476 and 443 nm, respectively) (see Fig. 12 for **1I**) similar to that observed in solution at 77 K and analogously attributed to radiative deactivation from S_1. At higher excitation energy, RTUP becomes visible (at 517, 563, 612 nm and 625 nm, respectively). By exciting at very shorter wavelengths (<300 nm) the molecular phosphorescence (630 and 680 nm, respectively) present also in solution at 77 K is activated. Investigation of crystals of **1I** at 77 K (Fig. 12) revealed an additional phosphorescence contribution at 460, 495 and 530 nm. Even in this case, RTUP was assigned to π–π aggregates while the new 77 K phosphorescence of ms order observed at 460 nm, firstly ascribed to the presence of I···N XB, was, after investigation of **[MI(TT)]$_n$** coordination polymers (see later), interpreted as due to I···C intermolecular electronic coupling with partial orbital overlapping[111] between the heavy iodine atom and the **TT** unit. Finally, the molecular phosphorescence of **1I** and **2I**, visible also at 298 K, is much more intense than that observed at 77 K for ***n*Br**, in agreement with the presence of the heavier iodine atom on the molecule.

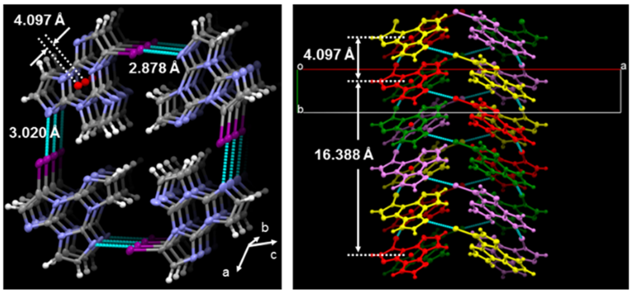

Fig. 13 Partial views along *b*- (left) and *c*-axes (right) of **1I** crystal structure showing columnar π–π stacks (centroids of the triazinic rings shown as red circles) interconnected through I···N XB (light blue dashed lines) to form intervolved quadruple helices along the *b*-axis. Reproduced with permission from ref. 71. Copyright 2019, John Wiley and Sons.

Comparison of the photophysical behaviour of halogenated compounds is reported in Fig. 14. The effect of the heavy halogen atoms can be accurately evaluated only through lifetimes of LEP, decreasing from **1Cl** to **1I**. In fact, LEP is associated with molecular electronic levels and it is observed for all **1X** under the same conditions (solid state, 77 K) allowing a reliable comparison.

To evaluate the extrinsic iodine heavy atom effect on the photoluminescence of **TT** isolated from the intrinsic one, a structural and spectroscopic investigation was performed on **TT·DITFB**, the 1 : 1 cocrystal self-assembled through I···N XB between **TT** and 1,4-diiodotetrafluorobenzene (see Fig. 15), **DITFB**.

Its crystal structure ($P2_1/n$ space group) consists of heteromeric zig-zag infinite 1D chains self-assembled through I···N XB, where **TT** acts as double XB acceptor and **DITFB** as a double XB donor (Fig. 15) with I···N distances, $r_{\text{I}\cdots\text{N}}$ = 3.031 and 3.006 Å, shorter by 14 and 15%, respectively, than the sum of vdW radii. Adjacent chains are connected through strong π–π stacking interactions among **TT** units.

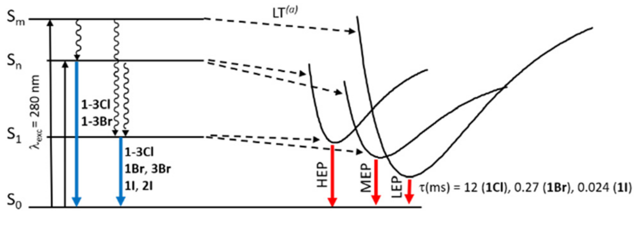

Fig. 14 Comparison through a simplified Jablonski diagram of solid **1–3X**. Lifetimes of LEP for **1X** are reported.[a] Even at RT for **1–2I**.

Open Access Article. Published on 20 January 2025. Downloaded on 1/21/2026 10:55:07 PM.
This article is licensed under a Creative Commons Attribution-NonCommercial 3.0 Unported Licence.

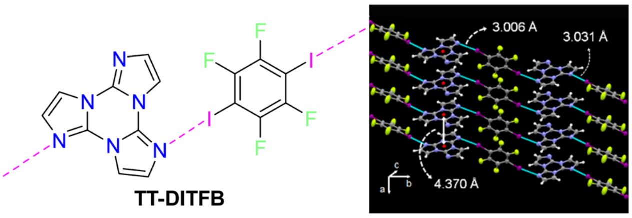

Fig. 15 Left: chemical structures of **TT·DITFB**. Right: partial view of its crystal structure showing columnar π–π stacks of **TT** (centroids of the triazinic rings shown as red circles) interconnected through I···N XB (light blue dashed lines) with **DITFB** to form infinite 1D zig-zag chains. Adapted with permission from ref. 71. Copyright 2019, John Wiley and Sons.

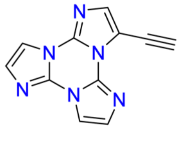

TT-CCH

Scheme 12 Chemical structure of **TT-CCH**.

Crystals of **TT·DITFB** show at 298 K (overall *Φ* equal to 5%) only broad fluorescence (at about 410 nm) and structured phosphorescence (at 496, 528 and 566 nm), while at 77 K broad, red phosphorescence (at 720 nm) dominates the spectrum comprising additional bands (Fig. 16). π–π stacking interactions among **TT** units were recognized as responsible for the structured phosphorescence, while the low energy contribution was associated through DFT/TDDFT calculations to the iodine extrinsic heavy atom effect, resulting in the presence of $^3(\sigma,\sigma^*)$ and $^3(\pi,\sigma^*)$ levels allowing SOC from close singlet states of different characters. This 'extrinsic-molecular phosphorescence', observed only at 77 K, is less efficient than the intrinsic one observed also at 298 K for **1I** and **2I**. Among the other bands observed at 77 K, additional phosphorescence was recognized through delayed spectra (at 463, 497, and 537 nm) and associated with the I···C intermolecular electronic coupling (T^I–S_0), similarly to what concluded for **1I**.

Based on these results, it was established that the molecular phosphorescence is better activated through an intrinsic heavy atom effect, being observed at 298 K only in **1I** and **2I**. Moreover, the I···C induced phosphorescence was confirmed as an extrinsic heavy atom effect, being observed in both **1I** and **TT·DITFB.**

On the whole, studies on **1-3X** revealed **1-3Cl** as the best performing among the full series, preserving the solid state multifaceted emissive behaviour but with enhanced AIE features (highest quantum yield) with respect to the bromine and iodine analogues. Moreover, the role of the extended network of intermolecular interactions in activating multiple radiative deactivation channels comprising fast and long-lived components was fully disclosed. In particular, strong π–π interactions dominating the crystal structures of all halo derivatives were deemed responsible for the RTUP, while extrinsic heavy atom effect was recognized as efficaceous in activating green phosphorescence only in the case of Br and I derivatives, owing to the low heavy-atom effect played by chlorine.

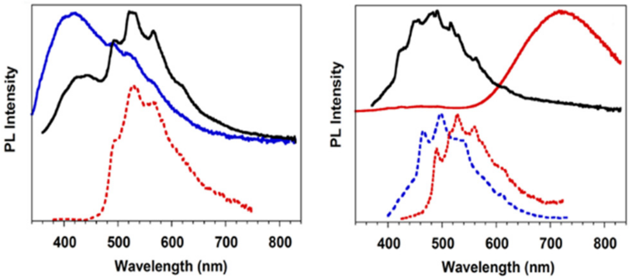

Fig. 16 Left: Emission spectra of **TT·DITFB** at 298 K: top: PL at λ_{exc} = 300 nm (blue) and λ_{exc} = 350 nm (black); bottom: phosphorescence (λ_{exc} = 350 nm, delay 0.5 ms, window 1 ms, red dashed); right: emission spectra of **TT·DITFB** crystals at 77 K: top: PL at λ_{exc} = 340 nm (black), λ_{exc} = 300 nm (red); bottom: phosphorescence at λ_{exc} = 320 nm (delay 10 ms, window 50 ms, blue dashed) and λ_{exc} = 370 nm (delay 10 ms, window 50 ms, red dotted). Adapted with permission from ref. 71. Copyright 2019, John Wiley and Sons.

3.3.3 TT-CCH. In DCM solutions, 3-ethynyltriimidazo[1,2-*a*:1′,2′-*c*:1″,2″-*e*][1,3,5]triazine, **TT-CCH** (Scheme 12), displays absorption at 240, 270 and 287 nm and a single, broad fluorescence at about 360 nm (Fig. 17) (*Φ* equal to 2%).[87]

For polymethylmethacrylate (PMMA)-blended films with low fluorophore loading (dye/matrix w/w% equal to 0.1) a single, unstructured fluorescence, HEF (at 330 nm), and a broad phosphorescence (at 442 nm), HEP, were observed at an appropriate excitation wavelength (Fig. 18). Blended films with higher loadings (w/w% equal to 5) display dual fluorescence (HEF at about 342 nm and LEF at about 383 nm) and dual phosphorescence (HEP at 442 nm and LEP at about 522 nm).

The compound crystallizes in the monoclinic $P2_1/c$ space group forming infinite ribbons with **TT-CCH** molecules connected through quite short CH···N HBs forming cyclic patterns ($r_{H\cdots N}$ = 2.33 and 2.48 Å, the former involving the acidic C(sp)–H bond). The ribbons are overlapped giving rise to columnar π–π aggregates.

Crystals of **TT-CCH** show excitation dependent behaviour (*Φ* = 16%) comprising dual fluorescence (HEF at 314, 326,

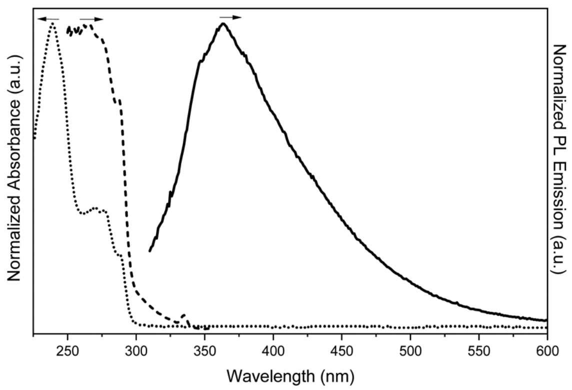

Fig. 17 Absorption (dotted line), excitation (dashed line, λ_{em}: 374 nm) and PL emission (continuous line, λ_{exc}: 290 nm) spectra of **TT-CCH** in DCM.

Open Access Article. Published on 20 January 2025. Downloaded on 1/21/2026 10:55:07 PM.
This article is licensed under a Creative Commons Attribution-NonCommercial 3.0 Unported Licence.

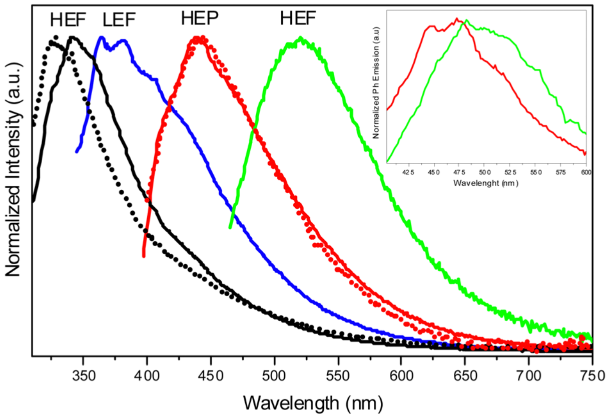

Fig. 18 PL emission spectra of **TT-CCH** in a PMMA matrix (0.1 w/w%, dotted line; 5 w/w%, full line) at 298 K. λ_{exc}: 290 nm (black lines), 330 nm (blue line), 380 nm (red lines) and 445 nm (green line). Inset: The delayed spectra are shown for the 5 w/w% concentration at short (40 μs delay, 200 μs window; red line) and long (4 ms delay, 20 ms window; green line) delay times.

338 nm and LEF at 354, 367, 377 nm) and dual phosphorescence (HEP at 434 nm and LEP at 538 nm). The relative intensity of the two fluorescent signals is temperature and grinding dependent, with LEF being attenuated through grinding and by increasing the temperature (Fig. 19). Of the four emissions, HEF and HEP were interpreted as molecular phenomena, while LEF and LEP as due to the supramolecular ones. In agreement with this hypothesis, in PMMA films, LEF and LEP appear only by increasing the dye-loading and HEF/LEF relative intensity shows mechanochromic dependence.

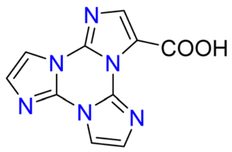

TT-COOH

Scheme 13 Chemical structure of **TT-COOH**.

The origin of LEF was clarified through DFT/TDDFT calculations on both the isolated molecule and different small aggregates, comprising CH$\cdots$N and/or π$\cdots$π stacked dimers and tetramers. The computed molecular S_1 level possessing (π,π*) character is localized on the $C\equiv C$ bond and the portion of the **TT** moiety directly bonded to it and lies very close to a triplet state from which HEP is originated. For the CH$\cdots$N aggregates, S_1 gradually red shifts and acquires an impressive increase of its oscillator strength, from 0.25 (monomer) to 0.74 (dimer) and then 1.64 (tetramer). For π–π stacked dimeric and tetrameric species a much lower increase in oscillator strength was computed, indicating that appearance of LEF is due to the strong HB characterizing the **TT-CCH** crystal structure and not to π–π stacking interactions, which are instead responsible for LEP as often observed among **TTs**.

3.3.4 TT-COOH.

Triimidazo[1,2-*a*:1′,2′-*c*:1″,2″-*e*][1,3,5]triazine-3-carboxylic acid, **TT-COOH** (Scheme 13), displays dual fluorescence (HEF at 327, 343 nm and LEF at 404 nm, overall Φ = 3.8%) in dilute DMSO solution.[89] The compound crystallizes in the centrosymmetric triclinic $P\bar{1}$ space group with the formation of intramolecular OH$\cdots$N hydrogen bonding and π–π stacking interactions involving the **TT** units. Crystals of **TT-COOH** display excitation dependent behaviour (Φ = 26%, Fig. 20) comprising dual fluorescence (HEF at about 342 nm and LEF at 386, 408 and 432 nm) and triple phosphorescence (HEP at 445 nm, MEP at 487 nm, LEP at 549, 590 and 642 nm).

Based on spectroscopic, structural and theoretical investigations, the emissions were recognized as molecular (HEF, LEF, HEP and MEP) or π–π aggregate (LEP) features (Fig. 20). The molecular contributions were associated with the presence of low energy excited states of (π,π*) and (σ,π*) symmetries, justifying separate deactivation radiative paths. Moreover, calculations on H-bonded dimers did not result in a remarkable increase of the S_1 oscillator strength as instead obtained for **TT-CCH**, as a consequence of the weaker interaction in **TT-COOH**. Therefore, the latter was classified as an anti-Kasha emitter differently from the former.

3.3.5 Functionalization with chromophoric groups.

Organic RTP emitters have recently proved to be attractive

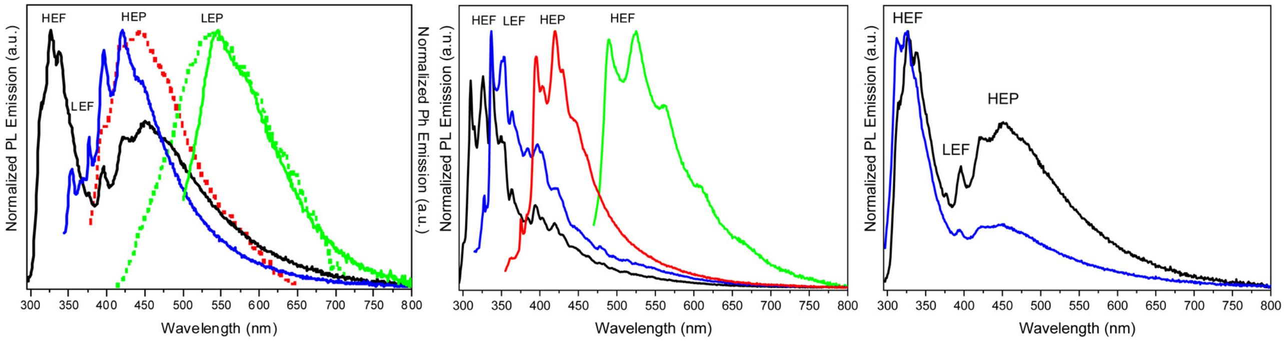

Fig. 19 Normalized PL emission spectra of **TT-CCH** crystals. Left at 298 K: Prompt (full line) and delayed (dashed line) spectra; $\lambda_{\text{exc.}}$: 275 nm (black); 330 nm (blue) and 486 nm (green); $\lambda_{\text{exc.}}$: 310 nm (dashed red, delay 15 μs, window 400 μs; dashed green, delay 1 ms, window 15 ms). Middle at 77 K: prompt spectra; $\lambda_{\text{exc.}}$: 275 nm (black); 300 nm (blue); $\lambda_{\text{exc.}}$: 340 nm (red); $\lambda_{\text{exc.}}$: 450 nm (green). Right at 298 K: before (black) and after (blue) manual grinding in a mortar; $\lambda_{\text{exc.}}$: 275 nm.

Open Access Article. Published on 20 January 2025. Downloaded on 1/21/2026 10:55:07 PM.
This article is licensed under a Creative Commons Attribution-NonCommercial 3.0 Unported Licence.

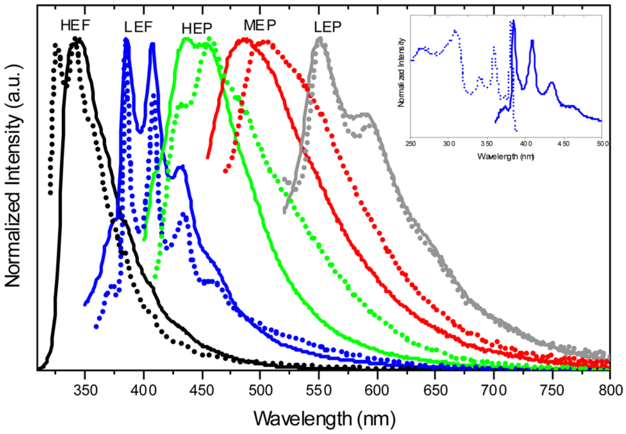

Fig. 20 Normalized PL emission spectra of **TT-COOH** crystals at RT (continuous lines) and 77 K (dotted lines). λ_{exc} = 300 nm (black); 340 nm (blue); 390 nm (green); 440 nm (red) and 500 nm (grey). Inset: Normalized emission (continuous, λ_{exc} = 340 nm) and excitation profiles (dotted, λ_{em} = 409 nm) at 77 K.

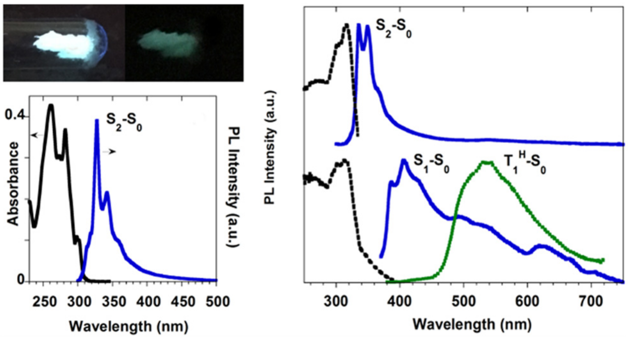

Fig. 21 (left) Top: powders of **TT-Benzo** at 77 K with UV irradiation on (left) and off (right). Bottom: DCM solutions at 298 K: absorption (black) and PL emission (blue, λ_{exc} = 260 nm). Right: Powders at 298 K: top: excitation (dashed black, λ_{exc} = 348 nm) and PL emission (blue, λ_{exc} = 260 nm). Bottom: excitation (dashed black, λ_{em} = 408 nm), PL emission (blue, λ_{exc} = 370 nm), and phosphorescence (green dotted, 10 ms delay, window 50 ms, λ_{exc} = 358 nm). Reproduced with permission from ref. 70. Copyright 2017, John Wiley and Sons.

luminescent materials for different applications, including, in particular, the field of biological sensing and imaging.[102–104] To be used in this area, however, RTP luminophores need to meet stringent requirements such as long wavelengths, bright RTP emission, suitable size and good water dispersibility. Organic substituents are expected to modify the emissive properties at both molecular and, through different packing modes, solid-state levels, though in a not completely predictable way. In order to extend the scope of the **TT** scaffold in view of possible biological applications, two main directions were envisaged. On one hand, the role of suitable chromophoric substituents (*e.g.* heteroaromatic substituents with red emission) in shifting the emission of **TT** towards the red while preserving the long lifetime of its triplet state was considered. On the other hand, the effect of extending the condensed polycyclic structure of **TT** on the photophysics of the organic emitter was examined, even though the latter aspect is still in its infancy and certainly deserves further investigation.

3.3.5a TT-Benzo. Benzo[4,5]imidazo[1,2-*a*]benzo[4,5]imidazo-[1,2-*c*]benzo[4,5]imidazo[1,2-*e*][1,3,5]triazine, hereafter **TT-Benzo** (Scheme 14), shows in trifluoroacetic acid (TFA) at 293 K an intense absorption band at 277 nm of (π,π*) character, which in DMSO is red-shifted to 285 nm with appearance of an additional band at 300 nm. A strong solvent effect was also observed for the (π,π*) emission at 380 nm in TFA, blue shifted and vibrationally resolved with maxima at 329 and 344 nm in DMSO[65] and 327, 341, 359 nm in DCM.[70]

TT-Benzo crystallizes in the $P\bar{1}$ space group[112] in an arrangement very similar to that of **TT** but with a higher intermolecular distance along its π–π columnar aggregates. At 298 K, microcrystalline powders of **TT-Benzo** show excitation dependent properties comprising both dual fluorescence (at 335, 350, 366 nm and 407 nm, the first being quite similar to the one observed in solution) and RTUP (at 530 nm); the latter is assignable to π–π stacking interactions (Fig. 21). The dual fluorescence was interpreted through DFT/TDDFT calculations, which revealed the presence of an S_0–S_1 transition of (π,π*) character and zero oscillator strength for symmetry reasons, and two almost degenerate transitions at slightly higher energy with large oscillator strength (S_0–S_2 and S_0–S_3). These electronic conditions are effective in producing anti-Kasha behaviour[105,113,114] and, on this basis, the high energy fluorescence observed in solution and in the solid state was associated with S_2–S_0 radiative deactivation. In the solid state, the S_0–S_1 transition acquires intensity due to the partial loss of molecular symmetry through intermolecular interactions, resulting in the S_1–S_0 fluorescence.

3.3.5b TT-pyrenes. Dilute DMSO solutions of **TTPyr$_{1-3}$** (Scheme 15) show two absorptions at 257, 268, and 279 nm and 332 and 347 nm of main pyrene character.[79,80] The strong red shift and broadening with respect to the parent compound were associated with the increased conformational freedom as

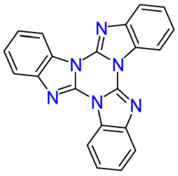

TT-Benzo

Scheme 14 Chemical structure of **TT-Benzo**.

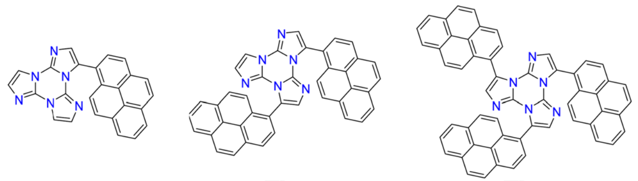

TTPyr
TTPyr$_2$
TTPyr$_3$

Scheme 15 Chemical structure of **TTPyr$_{1-3}$**.

Open Access Article. Published on 20 January 2025. Downloaded on 1/21/2026 10:55:07 PM. This article is licensed under a Creative Commons Attribution-NonCommercial 3.0 Unported Licence.

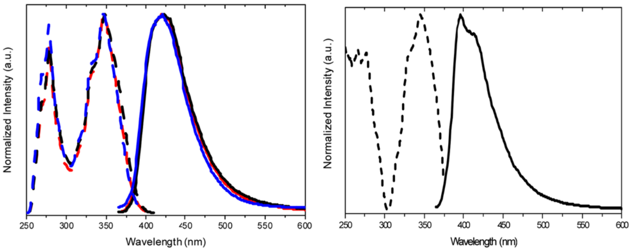

Fig. 22 Normalized PL emission (solid lines) and excitation (dashed lines) spectra at 298 K. Left: DMSO solutions of **TTPyr$_1$** (blue line), **TTPyr$_2$** (red) and **TTPyr$_3$** (black), λ_{exc} = 350 nm, λ_{em} = 420 nm. Right: **TTPyr$_1$** in PMMA (5% w/w), λ_{exc} = 345 nm; λ_{em} = 397 nm.

determined by DFT studies, resulting in an increased number of the involved excited states. An intense very broad single fluorescence emission (at about 420 nm) was observed for all of them (see Fig. 22) with impressively high quantum yield (92, 78 and 74% for **TTPyr$_1$**, **TTPyr$_2$** and **TTPyr$_3$**, respectively), when compared with pyrene itself (33.4%) under the same conditions, suggesting the positive role of the **TT** moiety in suppressing the ACQ (aggregation caused quenching) phenomenon affecting pyrene fluorescence.[115–117] Spin-coated blended films of **TTPyr$_1$** in PMMA (0.5 and 5 wt%) show an intense, vibronically resolved fluorescence at 396 nm (Φ about 75%), which is blue-shifted with respect to the one observed in DMSO solution. Based on DFT studies, two conformational minima, corresponding to different orientations of pyrene with respect to the **TT** moiety, were located on the S_0 potential energy surface (PES). These conformations were individuated in crystal structures of **TTPyr$_1$** (see below). In dilute solution, both conformations are populated owing to the flatness of the surface, resulting in a broad fluorescence emission, while in PMMA films the chromophore is frozen in the absolute minimum, and a narrower higher energy emission was observed.

Only for **TTPyr$_1$** single crystals suitable for XRD analysis were obtained by various methods. In particular, three crystalline forms, namely **TTPyr(RT)** ($P2_1/c$ space group, Fig. 23), **TTPyr(Et)** ($C2/c$ space group, Fig. 24) and **TTPyr(HT)** ($Pna2_1$ space group, Fig. 25), were isolated. The asymmetric unit of **TTPyr(Et)** contains one **TTPyr** and half ethanol molecule interacting *via* hydrogen bonds (Fig. 24).

In **TTPyr(RT)** and **TTPyr(Et)**, the **TT** unit of one molecule stacks in between two **Pyr** units of neighbouring molecules, forming infinite columns of π–π stacking fragments (Fig. 23 and 24). On the other hand, in **TTPyr(HT)** the molecules form columns where only the **TT** fragments are facing each other and the pyrene units of adjacent molecules protrude in opposite directions (Fig. 25).

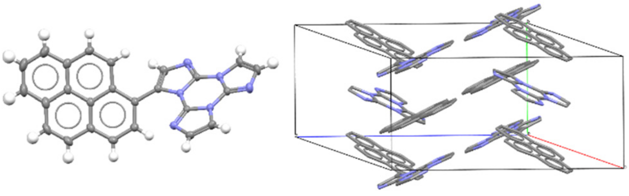

Fig. 23 X-Ray crystal structure of **TTPyr(RT)**. Left: View of a single **TTPyr** molecule (ellipsoid drawn at 30%); right: view of molecular packing (hydrogen atoms are omitted for clarity). Reproduced with permission from ref. 80. Copyright 2021, John Wiley and Sons.

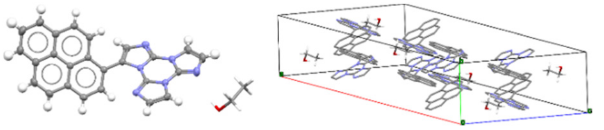

Fig. 24 X-Ray crystal structure of **TTPyr(Et)**. Left: View of a single **TTPyr** molecule interacting through hydrogen bonds with an ethanol molecule (ellipsoid drawn at 30%, only one model of disordered ethanol molecule is shown); right: view of the molecular packing (hydrogen atoms are omitted for clarity and only one model is shown for ethanol molecules). Reproduced with permission from ref. 80. Copyright 2021, John Wiley and Sons.

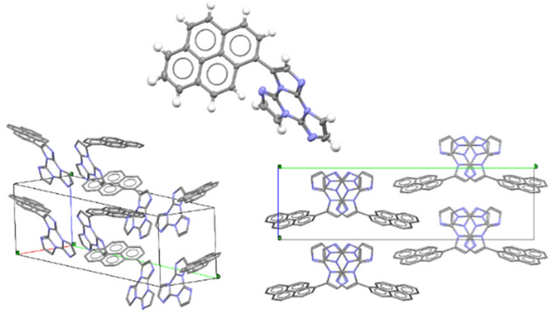

Fig. 25 X-Ray crystal structure of **TTPyr(HT)**. Top center: View of a single **TTPyr** molecule (ellipsoids are drawn at 30%); bottom: two views of the molecular packing (hydrogen atoms are omitted for clarity). Reproduced with permission from ref. 80. Copyright 2021, John Wiley and Sons.

Crystals of **TTPyr(RT)** and **TTPyr(Et)** display a similar excitation dependent photophysical behaviour (Φ about 40%), comprising one fluorescence band (at 490 and 493 nm, respectively) and one phosphorescence band (at 550 and 555 nm, respectively) (Fig. 26) with relative intensity varying with crystallinity of the examined sample.

In agreement with its different disposition of the chromophore inside the structure with respect to the other crystalline forms, **TTPyr(HT)** displays a macroscopically different photophysics with dual fluorescence (HEF and LEF at 420, 450 nm and 480 nm, respectively) and single phosphorescence (at 550 nm) with relative intensity depending on the excitation energy. For all phases, the phosphorescence feature was assigned to π–π (**TT-TT** or **TT-Pyr** interactions) aggregated species. For what concerns fluorescence, DFT/TDDFT calculations on dimeric prototypes of **TTPyr(RT)** evidenced a blocked conformation with reduced twisting with respect to the isolated molecule and therefore optimized lower energy S_1 minimum, resulting in the observed red shifted single fluorescence (monitored in solution). On the other hand, the **TTPyr(HT)** dimer, where the pyrene moiety is still free to get the two S_0 minima, produces dual fluorescence.

Relatively to **TTPyr$_2$** and **TTPyr$_3$**, showing in powder only one fluorescence band (at 490 and 476 nm, respectively) and one

Open Access Article. Published on 20 January 2025. Downloaded on 1/21/2026 10:55:07 PM.
This article is licensed under a Creative Commons Attribution-NonCommercial 3.0 Unported Licence.

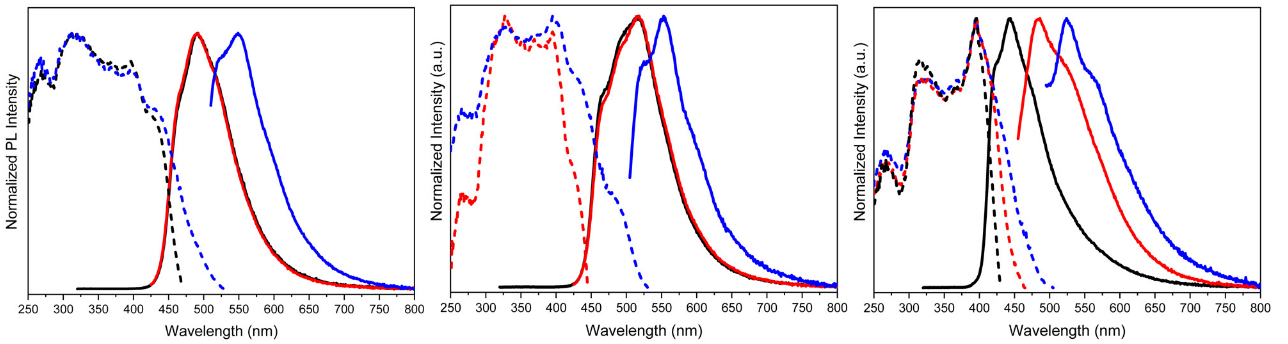

Fig. 26 Normalized PL emission (full line) and excitation (dashed line) spectra at RT. Left: **TTPyr(Et)** crystals. λ_{exc} = 300 nm (black line), λ_{exc} = 405 nm (red line), λ_{exc} = 495 nm (blue line); λ_{em} = 494 nm (black line); λ_{em} = 610 nm (blue line). Middle: **TTPyr(RT)** crystals. λ_{exc} = 300 nm (black line), λ_{exc} = 405 nm (red line), λ_{exc} = 490 nm (blue line); λ_{em} = 466 nm (red line), λ_{em} = 555 nm (blue line). Right: **TTPyr(HT)** crystals. λ_{exc} = 300 nm (black line), λ_{exc} = 440 nm (red line), λ_{exc} = 480 nm (blue line); λ_{em} = 445 nm (black line), λ_{em} = 483 nm (red line), λ_{em} = 524 nm (blue line).

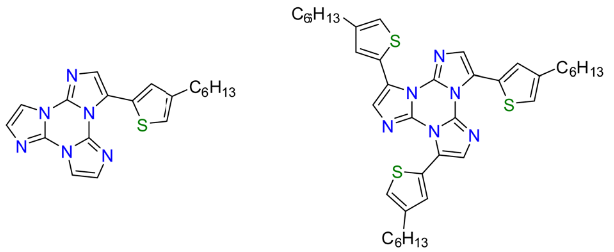

TT-HThio **TT-HThio$_3$**

Scheme 16 Chemical structures of **TT-HThio** and **TT-HThio$_3$**.

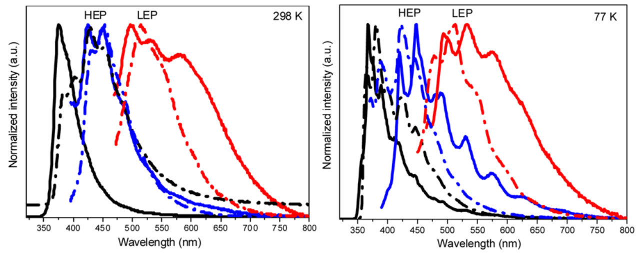

Fig. 27 Normalized PL emission of crystals of **TT-HThio**: (continuous lines) and of crystalline powders of **TT-(HThio)$_3$** (dashed dotted lines) spectra. Left 298 K at λ_{exc} = 300 nm (black), ≅380 nm (blue), 450 nm (red); right 77 K, emission at λ_{exc} = 300 nm (black), 360 nm (blue), ≅440 nm (red).

phosphorescence band (at 528 and 522 nm, respectively), the lack of structural details allowed drawing only qualitative conclusion. In particular, aggregated species were deemed responsible for the long-lived emission appearing at the same wavelength as that of **TTPyr** LEP.

3.3.5c TT-thiophenes. 3-(4-Hexylthiophen-2-yl)-triimidazo[1,2-*a*:1′,2′-*c*:1″,2″-*e*][1,3,5]triazine, **TT-HThio**, and 3,7,11-tri(4-hexylthiophen-2-yl)-triimidazo[1,2-*a*:1′,2′-*c*:1″,2″-*e*][1,3,5]triazine, **TT-(HThio)$_3$** (Scheme 16), display in DCM dilute solutions at 298 K, a single fluorescence band (at 370 and 380 nm, Φ equal to 11% and 5%, respectively).[86] At 77 K and in PMMA blended films (0.5 wt%, Φ equal to 15% and 17%, respectively) superimposable spectra were obtained (fluorescence at 365 and 370 nm, respectively) as expected for a molecular emission in rigidified media.

TT-HThio crystallizes in the $P\bar{1}$ space group with head-to-head π-stacked aggregates. No single crystals were obtained for **TT-(HThio)$_3$**.

Crystals of the former and powder of the latter display crystallization enhanced emission (CEE) through an excitation dependent behaviour comprising one fluorescence band (at 376 and 382 nm, and 400 nm, respectively) and two phosphorescence bands (HEP at 425 and 451 nm, and 428 and 453 nm, respectively; LEP at 497, 530, and 578 nm, and 514 and 550 nm, respectively) (overall Φ = 26% and 22%, respectively, Fig. 27). CEE behaviour was confirmed by a decrease in Φ (18%) through grinding crystals of **TT-HThio** in a mortar. From DFT/TDDFT and X-ray studies, HEP and LEP observed in both solid compounds were assigned to molecular and aggregated π–π (**TT-TT**) species.

3.3.5d TT-carbazoles. Carbazole, **Cz**, and its derivatives have been the subject of numerous investigations aimed at clarifying the mechanisms involved in their RTUP. It was reported that commercially available **Cz** is mixed with traces of its isomer (1*H*-benzo[*f*]indole), which is involved in the origination of the long lived emission.[118,119] This discovery has further pointed to the well-known issue of using highly purified uncontaminated samples when investigating the luminescence properties of materials but has also stimulated studies on new pure carbazole RTP derivatives.[120–122] With this in mind, we synthesized and deeply investigated three **TT-Cz** derivatives with the two units differently connected: specifically 3-(9*H*-carbazol-9-yl)triimidazo[1,2-*a*:1′,2′-*c*:1″,2″-*e*][1,3,5]triazine, **TT-(N)-Cz**, 3-(9-ethyl-9*H*-carbazol-3-yl)-triimidazo[1,2-*a*:1′,2′-*c*:1″,2″-*e*][1,3,5]triazine, **TT-(C)-Cz,** and 3-(4-(9*H*-carbazol-9-yl)phenyl)triimidazo[1,2-*a*:1′,2′-*c*:1″,2″-*e*][1,3,5]triazine, **TT-Ph-Cz** (Scheme 17).[81,84]

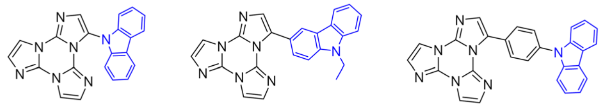

TT-(N)-CZ **TT-(C)-CZ** **TT-Ph-CZ**

Scheme 17 Chemical structures of **TT-(N)-Cz**, **TT-(C)-Cz** and **TT-Ph-Cz**.

Open Access Article. Published on 20 January 2025. Downloaded on 1/21/2026 10:55:07 PM.
This article is licensed under a Creative Commons Attribution-NonCommercial 3.0 Unported Licence.

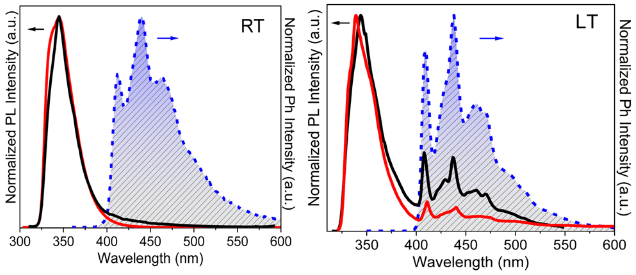

Fig. 28 **TT-(N)-Cz** normalized emission spectra (λ_{exc} = 300 nm). PL of DCM solutions (10^{-6} M, red) at 298 K (left) and 77 K (right) in air. PL of PMMA films (0.5 wt%) in vacuum (black) and delayed spectra (blue dashed; delay 200 μs, window 500 μs at 298 K (left); delay 5 ms, window 10 ms at 95 K (right).

*3.3.5d.1 **TT-(N)-Cz**.* In dilute DCM solution **TT-(N)-Cz** shows at room temperature two sets of absorption bands at 280 and 288 nm and 313 and 326 nm and a broad fluorescence band at 345 nm (Φ = 27%). At 77 K, a strong fluorescence band at 339 nm and a much weaker vibrationally resolved phosphorescence band at 411, 439, and 466 nm are observed. Blended PMMA films (**TT-(N)-Cz** 0.5 wt%, Fig. 28) display at RT in vacuum one fluorescence band at 345 nm (Φ = 28%) and one vibrationally resolved phosphorescence band (maxima at 412, 440 and 462 nm).

TT-(N)-Cz crystallizes in the monoclinic $P2_1/c$ (**TT-(N)-CzM**) and in the triclinic $P\bar{1}$ (**TT-(N)-CzT**) space groups. In both **TT-(N)-Cz** polymorphs, **TT** and **Cz** are almost orthogonal, with structures dominated by π–π stacking interactions between **TT** moieties (see Fig. 29).

Crystals of both polymorphs (Fig. 30) revealed quite similar excitation dependent emissive features (Φ = 13 and 16% for **TT-(N)-CzT** and **TT-(N)-CzM**, respectively) comprising HEF (349 and 357 nm for **TT-(N)-CzT** and **TT-(N)-CzM**, respectively), LEF (in the 380–402 nm interval), HEP (442, 464, and 437 nm, respectively) and LEP (509 and 517 nm, respectively).

The origin of this multicomponent emissive behaviour was disclosed through spectroscopic, structural and computational studies revealing the molecular or the aggregated nature of each contribution. LEF and LEP possess aggregated origin as proven by both their absence in diluted solutions and blended films and their quenching through crystal grinding. In addition, LEP appears in the same spectral region where RTP is observed for **TT** emitters having columnar or dimeric π–π aggregates. Based on theoretical studies, the LEF origin was as well attributed to strong π–π interactions involving the **TT** scaffold. In fact, TDDFT calculations performed on the molecule resulted, among the others, in an S_1 state of **Cz** character and an S_3 state of **TT** character, both having (π,π*) symmetry. For π–π dimeric prototypes a clear stabilization accompanied by a noteworthy increase in the oscillator strength was calculated only for S_3, which has been therefore identified as the lowest energy excited state in the crystal (S^H).

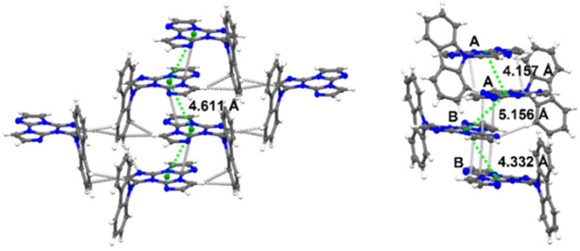

Fig. 29 Crystal packing of **TT-(N)-CzM** (left) and **TT-(N)-CzT** (right), showing the shorter distances between triazinic geometrical centroids (green spheres) and intermolecular contacts shorter than the sum of vdW radii (light grey dashed lines). Ellipsoids at 30% probability. Reproduced with permission from ref. 84. Copyright 2023, by Elsevier Ltd.

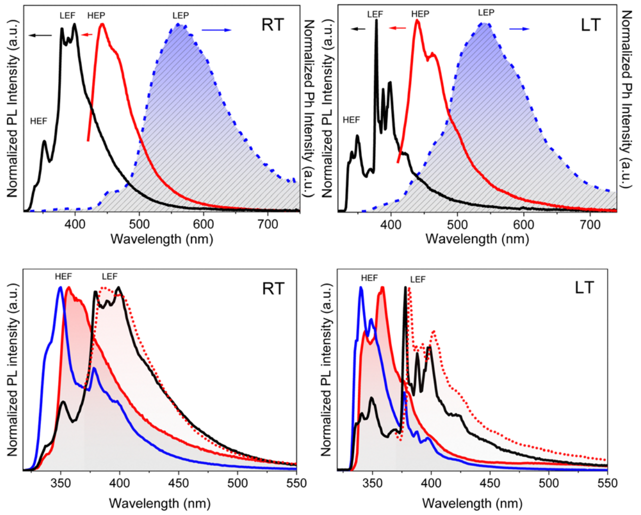

Fig. 30 Normalized emission at 298 K (left) and 77 K (right). Top: **TT-(N)-CzT** crystals: PL spectra (continuous lines): λ_{exc} = 300 nm (black) and λ_{exc} = 400 nm (red); delayed spectra (blue dashed): delay 1 ms, window 5 ms. Bottom: PL emission spectra of: **TT-(N)-CzM** crystals, λ_{exc} = 300 nm (red continuous); λ_{exc} = 355 nm (red dotted); **TT-(N)-CzT** crystals, λ_{exc} = 300 nm, before (black) and after (blue) grinding.

*3.3.5d.2 **TT-(C)-Cz**.* In dilute DCM solution, **TT-(C)-Cz** shows at RT two absorption bands at 239 and 290 nm with a tail at about 330 nm and a broad fluorescence at 380 nm (Φ = 20%). At 77 K, a broad long-lived component at about 500 nm (LEP) is clearly visible in the PL spectrum. PMMA films (**TT-(C)-Cz** 0.5 wt%, Fig. 31) in vacuum display one fluorescence band at 377 nm and two phosphorescence bands at about 417 nm (HEP) and 515 nm (LEP), which appear to be vibronically resolved at 90 K (at 412, 442, and 500 nm, respectively).

TT-(C)-Cz crystallizes in the $Pna2_1$ space group with two independent molecules in its a.u., *i.e.*, A and B, having the dihedral angle between **TT** and **Cz** units equal to 34.2° (A) and 37.8° (B), indicating partial conjugation. Moreover, differently from the **TT-(N)-Cz** polymorphs, in **TT-(C)-Cz** the π–π stacking interactions between **TT** units are replaced by analogous interactions between **TT** and **Cz**.

TT-(C)-Cz crystals (Φ = 28%, Fig. 32) display excitation dependent PL spectra comprising one fluorescence band at 402 nm with shoulder at 420 nm and one phosphorescence band at 460 nm with shoulder at 486 nm (HEP). Moreover, an

Open Access Article. Published on 20 January 2025. Downloaded on 1/21/2026 10:55:07 PM.
This article is licensed under a Creative Commons Attribution-NonCommercial 3.0 Unported Licence.

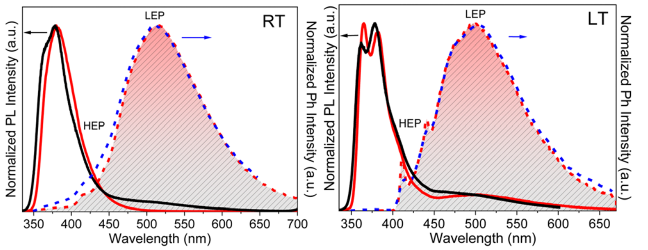

Fig. 31 **TT-(C)-Cz** normalized emission spectra (λ_{exc} = 300 nm). PL of DCM solutions (2×10^{-6} M, red continuous) at 298 K (left) and 77 K (right). PL of PMMA films (0.5 wt%, at 298 K, left, and 90 K, right) in vacuum (black) and delayed spectra (blue dashed, delay 0.2 ms, window 0.5 ms; red dashed, delay 50 ms, window 10 ms at 95 K.

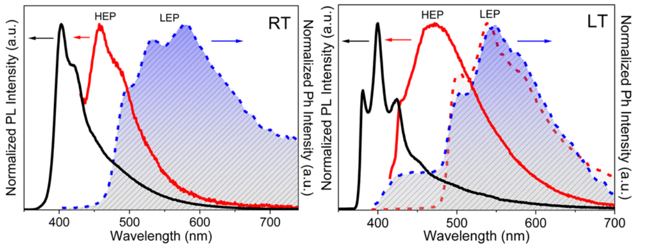

Fig. 32 Normalized emission spectra of **TT-(C)-Cz** crystals at 298 K (left) and 77 K (right). PL (continuous line) λ_{exc} = 300 nm (black) and λ_{exc} = 415 nm (red), delayed spectra (dashed line) λ_{exc} = 385 nm (298 K, delay 1 ms, window 5 ms; 90 K, blue: delay 0.5 ms, window 0.5 ms; red: delay 10 ms, window 20 ms).

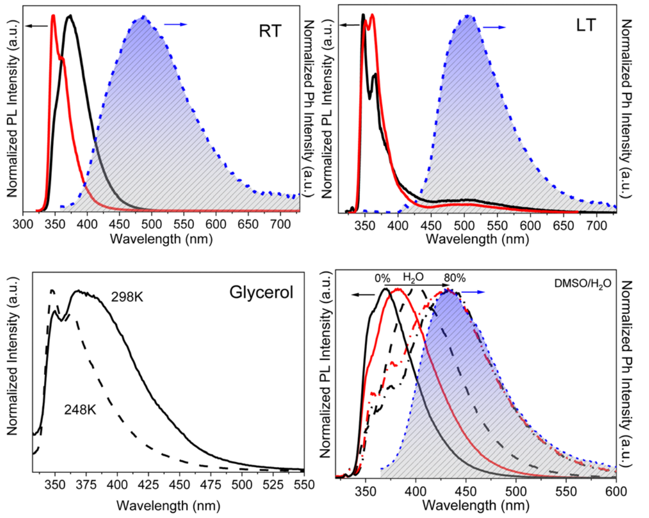

Fig. 33 **TT-Ph-Cz**. Normalized emission spectra (λ_{exc} = 300 nm). Top: PL in DCM (2×10^{-6} M, red lines) at 298 K (left) and 77 K (right) in air. PL of PMMA films (0.5 wt%, at 298 K, left, and 90 K, right) in vacuum (black) and delayed spectra (blue dashed, delay 0.2 ms, window 0.5 ms). Bottom: PL in glycerol (2×10^{-6} M, right) at 248 K (dashed line) and 298 K (continuous line). PL in DMSO (10^{-6} M) at 298 K (left) with increasing H_2O volume. 0% (black continuous), 20% (red continuous), 50% (black dashed), 70% (red dashed-dotted), 80% (black dashed-dotted). Delayed spectrum (blue dashed, delay 0.2 ms, window 0.5 ms) of the 80% water fraction solution.

additional phosphorescence band (LEP at 531 and 580 nm and at 500 and 540 nm at RT and 77 K, respectively) was disclosed in delayed spectra.

Supported by DFT/TDDFT calculations, fluorescence and HEP were associated with molecular excited states. They are red shifted with respect to the corresponding ones in **TT-(N)-Cz** owing to the reduced molecular twisting and the consequently increased electronic communication between **TT** and **Cz**. Again, LEP was attributed to a triplet of aggregated origin and its appearance in solutions or blended films was justified by the presence of aggregated forms even at very low concentrations. However, in the present case, less efficacious π–π stacking interactions between **TT** and **Cz** moieties result in RTP visible only in delayed experiments and in the absence of LEF.

3.3.5d.3 ***TT-Ph-Cz.*** The compound shows at 298 K in dilute DCM solutions four absorption maxima at 236, 293, 310 and 340 nm and a broad, structureless fluorescence band at 370 nm with a shoulder at 350 nm (Φ = 63%). At 77 K, a narrowing of the band (maximum at 353 nm) was observed together with the appearance of a broad phosphorescence band centered at 512 nm. The molecular or aggregate origin of the latter could not be established since, even in dilute solutions, the presence of small aggregates in frozen DCM is possible.[68,85] PMMA films (**TT-Ph-Cz** 0.5 wt%, Fig. 33) *in vacuo* display at 298 and 77 K a photophysical behaviour strongly resembling that of frozen solution. In particular, one narrow fluorescence band with vibronic replicas at 347 and 360 nm (Φ = 60.2%) and a broad phosphorescence band (490 or 508 nm, at 298 and 90 K, respectively) were observed. Speculating rigidification effects, spectra of dilute glycerol solution were collected. At 298 K, a broad band centered at 380 nm and a narrow peak at 350 nm were visible. Importantly, disappearance of the 380 nm component was observed by increasing the viscosity of the solution at low temperature. These results suggested dual emission from a Franck–Condon (FC) and a relaxed emitting state of molecular **TT-Ph-Cz,** as confirmed by theoretical calculations. Intriguingly, using solvent/non-solvent (DMSO/water equal to 20/80%) mixtures, RTP (430 nm) nanoaggregates were prepared.

TT-Ph-Cz crystallizes in three phases: **TT-Ph-CzM** (monoclinic $C2/c$ space group), **TT-Ph-CzT** (triclinic $P\bar{1}$) and **TT-Ph-CzO** (orthorhombic $Pbca$), all characterized by the same **TT-Cz** columnar aggregates. **TT-Ph-CzM** includes, in its a.u., one MeOH molecule, which is lost at 393 K, resulting in a single-crystal-to-single-crystal transition to **TT-Ph-CzT** and, at 443 K, to **TT-Ph-CzO** (Fig. 34). Transformation of **TT-Ph-CzM** into **TT-Ph-CzT** was found to be reversibly accomplished through grinding and MeOH exposure.

The interconversion among the three phases was followed through thermal analysis, photoluminescence investigations and XRPD measurements.

TT-Ph-CzM crystals display multiple emissions (Fig. 35) comprising at 298 K, HEF (375 and 408 nm), LEF overlapped with HEP (425 nm) and LEP (540 nm, overall Φ = 43%) and, at 77 K, only HEF (373 and 388 nm) and LEP (523 nm). The absence of LEF and HEP at 77 K was interpreted with two possible excited state conformations, with the relaxed one

Open Access Article. Published on 20 January 2025. Downloaded on 1/21/2026 10:55:07 PM.
This article is licensed under a Creative Commons Attribution-NonCommercial 3.0 Unported Licence.

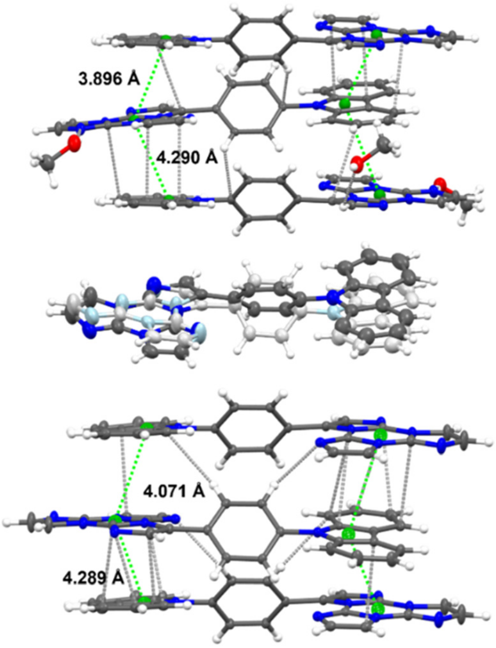

Fig. 34 Crystal structures of **TT-Ph-CzM** (top), **TT-Ph-CzT** (middle, showing the two disordered forms by different color gradation) and **TT-Ph-CzO** (bottom). In *a* and *c*, the shorter distances between triazinic and pyrrolic geometrical centroids (green spheres) and intermolecular contacts shorter than the sum of vdW radii (light grey dashed lines) are reported. Ellipsoids at 30% probability. Reproduced from ref. 81 under the terms of the Creative Commons CC BY license. Copyright 2023, John Wiley and Sons.

being not accessible at low temperature, in agreement with results obtained in solution. In addition, LEP was associated with π–π stacking interactions among TT and Cz units.

T-Ph-CzT and **TT-Ph-CzO** display, as well, multiple emissions but with reduced contribution from LEF/HEP at 298 K. This difference was related to the co-crystallized MeOH in **TT-Ph-CzM,** forming strong HBs with the **TT** unit. These, on one hand, provide conformational freedom to the **Ph-Cz** fragment resulting in LEF and, on the other hand, contribute to suppressing non-radiative deactivation channels highly competitive with HEP.

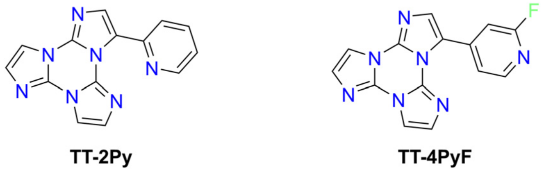

Scheme 18 Chemical structures of **TT-2Py and TT-4PyF** derivatives.

These studies revealed how synergistic and different combinations of **TT** and a chromophoric fragment (**Cz**) can result in quite different emissive behaviours due to both molecular reasons and aggregation modes. Crystals of **TT-(N)-Cz** (both polymorphs), **TT-(C)-Cz** and **TT-Ph-Cz,** with or without co-crystallized MeOH, display one LEP band associated with π–π stacking interactions involving only the **TT** unit or **TT** and **Cz** units. Moreover, **TT-(N)-Cz** and **TT-Ph-Cz** are characterized by HEF of molecular origin and LEF of different nature in the two compounds: in **TT-(N)-Cz** LEF derives from the **TT**-based π–π aggregated species, while in **TT-Ph-Cz** it is associated with conformational freedom resulting in rigidochromic and multi-stimuli responsive behaviour.

3.3.5e TT-pyridines. Among **TTs**, 3-(pyridin-2-yl)triimidazotriazine (**TT-2Py**), the pyridine derivative with the pyridinic nitrogen atom in the *ortho* position with respect to **TT** (Scheme 18) is characterized by multifaceted emissive properties particularly difficult to rationalize.[85] In fact, the partial rotational freedom of the pyridine ring is responsible for different metastable states, which result, in the crystalline phase, in the formation of three polymorphs and in excitation dependent emission comprising multiple fluorescence and RTP bands even in blended films. In particular, **TT-2Py** photoluminescence is characterized by two fluorescence components (HEF and LEF) and four phosphorescence components (HEP, MEP, two LEPs and DRP) related to the physical state of the sample.

In dilute DCM and ACN solutions at 298 K, **TT-2Py** displays absorption bands at about 235 and 290 nm and one emission

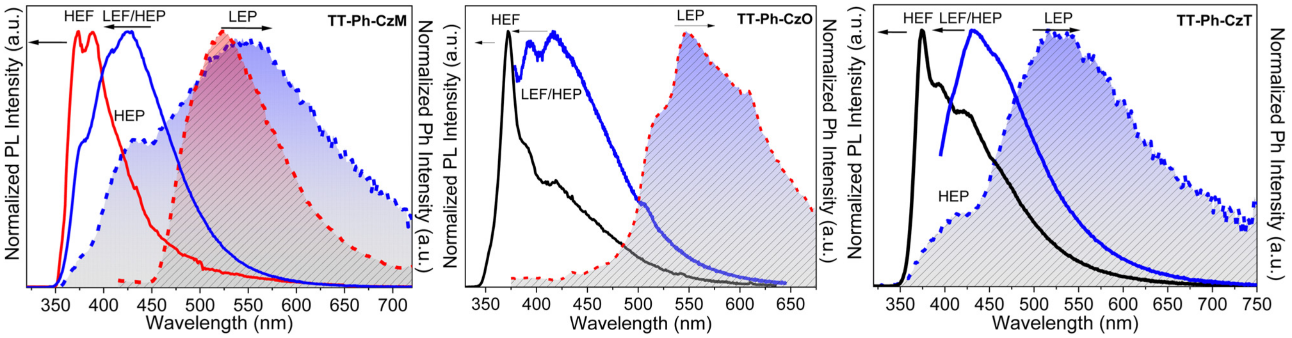

Fig. 35 Normalized PL (full lines) and delayed (dashed lines) spectra. Left: **TT-Ph-CzM** crystals (λ_{exc} = 300 nm) at 298 K (blue, blue dashed: delay 0.2 ms, window 0.5 ms) and 77 K (red, red dashed: delay 1 ms, window 5 ms). Middle: **TT-Ph-CzO** crystals at 298 K (black: λ_{exc} = 300 nm; blue: λ_{exc} = 370 nm; red: λ_{exc} = 360 nm, delay 1 ms, window 5 ms). Right: **TT-Ph-CzT** crystals at 298 K (black: λ_{exc} = 300 nm; blue full: λ_{exc} = 375 nm; blue dashed: λ_{exc} = 300 nm, delay 0.2 ms, window 0.5 ms.

Open Access Article. Published on 20 January 2025. Downloaded on 1/21/2026 10:55:07 PM.
This article is licensed under a Creative Commons Attribution-NonCommercial 3.0 Unported Licence.

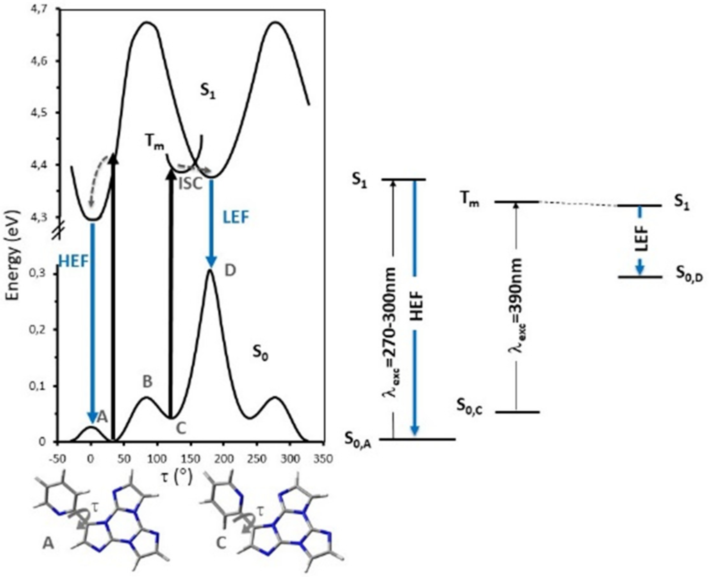

Fig. 36 Left: scans of the relaxed potential energy surfaces of S_1 and S_0 of **TT-2Py** along the N_{py}–C_{py}–C_{TT}–C_{TT} torsion angle, τ, at the (TD)-ωB97X/6-311++G(d,p) level of theory. T_m represents a generic triplet level, A and C denote minima on S_0 and B is the barrier between the two minima. Energies are relative to the S_0 state equilibrium geometry. Right: simplified Jablonski diagram of the fluorescence components of **TT-2Py**.

band at 350 nm ($\Phi \cong 17\%$). Detailed investigation of delayed spectra of deareated solutions and solvent–non-solvent mixtures indicated the presence of different long-lived emissions. In particular, HEP and MEP at 345 and 380–420 nm, respectively, and two LEPs in the 490–560 nm interval, were observed.

TT-2Py crystallizes as three different polymorphs (**A**, *Pbcn*; **H**, $P2_1/c$ and **X**, $P2_1/c$ space group) depending on the recrystallization solvent (CH_2Cl_2/CH_3OH, CH_3CN/H_2O or CH_3CN, respectively). All of them display, in their crystal structure, π–π stacking interactions among **TT** moieties, characterized by slightly different intermolecular distances and slippage features. The **TT** units are further anchored to each other by several short C–H···N HBs in the plane roughly perpendicular to the stacking axis. On the other hand, the pyridinic ring is involved only in weak interactions, resulting in slightly different tilting with respect to **TT** (41.47, 43.7 and 37.6/39.6° in **A**, **H**, and the two independent molecules of **X**, respectively).

According to an extensive spectroscopic, structural and theoretical investigation, LEP and DRP were attributed to dimeric or columnar π–π interactions among **TT** units, respectively. Noteworthily, while DRP was observed only for crystals of the polymorph with the strongest π–π interaction, the LEP components are present in all phases, including dilute solutions, where the presence of aggregated species cannot be totally excluded. The remaining emissions, namely HEF, HEP, MEP and LEF, were associated with molecular electronic states: HEF to S_1, HEP to a high energy T_n, MEP to T_1 and LEF to S_1 of a different conformer. In more detail, HEP anti-Kasha emission is due to the difficult IC from T_n to T_1 having different characters ((σ/π,π*) and (π,π*), respectively). LEF is associated with the presence, in the **TT-2Py** ground state (Fig. 36 left), of a local minimum (C) where the pyridinic N atom faces the **TT** unit rather than on the opposite side, as found in the minimum energy geometry (A). Although conformer C is not observed in any of the **TT-2Py** polymorphs, its minority presence cannot be excluded in any of the examined phases (solution, blended films and, as defects, in the crystal phase), with the two minima being separated by a low ($\cong 2$ kcal mol^{-1}) barrier (B). The two observed fluorescence components are therefore associated with radiative decay from S_1 of relaxed conformers A (HEF) and C (LEF), with the latter emission being detectable only by excluding the stronger HEF. The mechanism proposed to explain LEF, requiring population of a triplet T_m of low energy followed by ISC to S_1, has been supported by pump–probe experiments.

To deepen the comprehension of the mechanisms involved in **TT-2Py** photophysical behaviour, blended PMMA films were exposed to acidic vapors to give **TT-2PyH**$^+$, where a proton is added to the pyridinic nitrogen atom. According to DFT scan calculations, the conformation of the protonated species was predicted to be locked due to the formation of a strong $N–H^+\cdots N$ intramolecular hydrogen bond, accessible after rotation around the **TT**-pyridine bond by about 180° with respect to the neutral form. Such blocked structure predicted the suppression of LEF. Moreover, all computed transitions (both singlet and triplet states) were found to be red shifted with respect to the neutral form and to possess (π,π*) character, therefore excluding the possible presence of anti-Kasha HEP. In agreement with this finding, for **TT-2PyH**$^+$/PMMA blended films, only one fluorescent band (at 412 nm) was observed (Fig. 37), together with a weak phosphorescent band, both at lower energy with respect to the corresponding ones of **TT-2Py**.

3-(2-Fluoropyridin-4-yl)triimidazo[1,2-*a*:1′,2′-*c*:1″,2″-*e*][1,3,5]triazine, **TT-4PyF** (Scheme 18), displays in dilute ACN solution at 298 K two absorption maxima at 227 and 291 nm and an

Open Access Article. Published on 20 January 2025. Downloaded on 1/21/2026 10:55:07 PM.
This article is licensed under a Creative Commons Attribution-NonCommercial 3.0 Unported Licence.

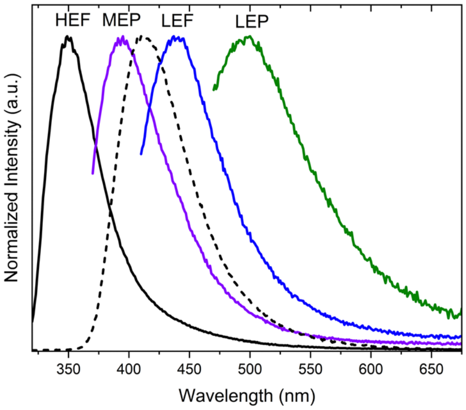

Fig. 37 Photophysical properties of **TT-2Py** in PMMA (**TT-2Py**/PMMA 10% wt) before (solid lines) and after (dashed line) HCl exposure. PL emission spectra λ_{exc} = 300 nm (black lines), λ_{exc} = 350 nm (violet), λ_{exc} = 390 nm (blue), and λ_{exc} = 450 nm (green).

intense fluorescence band at 358 nm (Φ = 50%).[82] At 77 K, an additional long-lived contribution is present at 454 nm. Similarly, fluorescence (at 348 nm) and green phosphorescence (at 415 and 436 nm) are observed at 298 K in PMMA blended films (w/w 6%).

The compound crystallizes in the $P\bar{1}$ space group with columnar π–π (**TT-TT**) aggregates. Crystals of **TT-4PyF** are characterized by fluorescence (at 373 nm) and dual phosphorescence (HEP at 403, 424 and 446 nm, and LEP at 547 nm, Fig. 38) with overall Φ = 25%. Based on structural and computational studies, HEP has been assigned to a molecular triplet while LEP has been ascribed to π–π aggregates. The presence of a single high energy fluorescence in **TT-4PyF** having only one conformer further supports the hypothesis of a different conformer at the origin of LEF in **TT-2Py**.

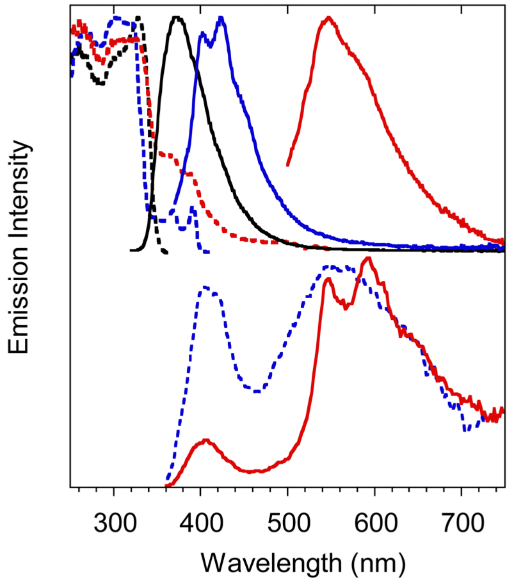

Fig. 38 Crystals of **TT-4PyF** at 298 K. Upper panel: normalized PL emission (λ_{exc} = 300 nm, black solid line; λ_{exc} = 360 nm, blue solid line; λ_{exc} = 480 nm, red solid line) and excitation (λ_{em} = 373 nm, black dashed line; λ_{em} = 425 nm, blue dashed line; λ_{em} = 570 nm, red dashed line) spectra. Bottom panel: Normalized phosphorescence spectra (λ_{exc} = 300 nm; delay 200 μs, window 1 ms, blue dashed line; delay 5 ms, window 20 ms, red solid line). Reproduced from ref. 82 under the terms of the Creative Commons CC BY license. Copyright 2019 by the authors. Licensee MDPI, Basel, Switzerland.

3.3.6 TTs as ligands in hybrid inorganic/organic derivatives. Metal containing compounds are usually characterized by short lifetimes of their triplet states due to the strong SOC associated with the presence of the heavy metal atom, which favors both ISC and radiative deactivation through otherwise spin-forbidden paths. This heavy-atom effect is larger when the metal orbitals are involved in the luminescence transition and this is the reason why solid-state afterglow emission is extremely rare in coordination compounds.

In this regard, an additional interesting feature of **TT** derivatives is the presence, at the vertexes of a regular triangle, of three nitrogen atoms potentially available for coordination, leading to various metal complexes and coordination polymers especially with filled-shell d^{10} systems, which lack low lying ligand-field excited states and offer an opportunity to observe other excited states.

3.3.6a TT as a ligand. By reacting **TT** with different metal salts, either **TT** coordination compounds or complexes where **TT** molecules are cocrystallized were obtained.

In particular, four coordination compounds, namely **$[Zn_3(CH_3COO)_6(H_2O)_2](TT)_2$**, **$[Cd(H_2O)_6](ClO_4)_2(TT)_2$**, **$[Cd(H_2O)_6](BF_4)_2(TT)_2$** and **$[Zn(H_2O)_6](BF_4)_2(TT)_2$**, accommodating **TT** as a guest in their crystal lattice, were isolated and investigated to clarify the extrinsic heavy metal effect on the chromophore's photophysics.

In crystals of **$[Zn_3(CH_3COO)_6(H_2O)_2](TT)_2$** the **TT** moieties are organized in π–π stacked columns similar to those found in **TT** itself (Fig. 39).[123]

In agreement with this finding, crystals of **$[Zn_3(CH_3COO)_6(H_2O)_2](TT)_2$** display at 298 K both fluorescence (at about 400 nm) and RTUP (at about 555 nm, Fig. 40); the latter is associated with the presence of the observed stacking interactions. By comparison between the metal complex and **TT**, the external heavy atom effect in the intensification of the RTUP emission was disclosed.

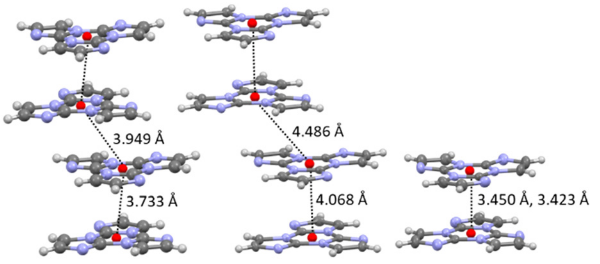

Fig. 39 Motifs of chromophore's aggregation in **TT** (left); **$[Zn_3(CH_3COO)_6(H_2O)_2](TT)_2$** (centre); **$[Cd(H_2O)_6](ClO_4)_2(TT)_2$**, **$[Cd(H_2O)_6](BF_4)_2(TT)_2$** and **$[Zn(H_2O)_6](BF_4)_2(TT)_2$** (right) with distances between centroids equal to 3.450 Å for the former and to 3.423 Å for the latter two. Reproduced with permission from ref. 123. Copyright 2019, John Wiley and Sons.

Open Access Article. Published on 20 January 2025. Downloaded on 1/21/2026 10:55:07 PM.
This article is licensed under a Creative Commons Attribution-NonCommercial 3.0 Unported Licence.

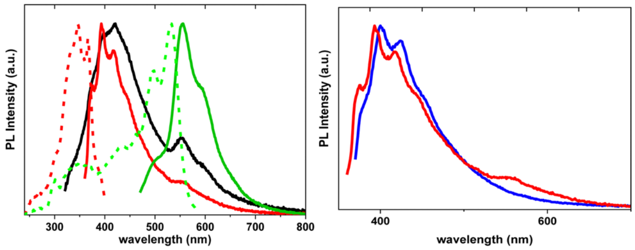

Fig. 40 Normalized PL spectra. Left: crystals of **$[Zn_3(CH_3COO)_6(H_2O)_2](TT)_2$**. Emission (full lines) at λ_{exc} = 300 nm (black), λ_{exc} = 340 nm (red), λ_{exc} = 450 nm (green), and excitation (dashed lines) at λ_{em} = 416 nm (red) and λ_{em} = 600 nm (green). Right: Emission spectra of **$[Zn_3(CH_3COO)_6(H_2O)_2](TT)_2$** ($\lambda_{exc}$ = 340 nm, red) and **TT** (λ_{exc} = 350 nm, blue).

In the three isostructural compounds, **$[Cd(H_2O)_6](ClO_4)_2(TT)_2$**, **$[Cd(H_2O)_6](BF_4)_2(TT)_2$** and **$[Zn(H_2O)_6](BF_4)_2(TT)_2$**, **TT** molecules form stacked dimers instead of columns.

Crystals of **$[Cd(H_2O)_6](ClO_4)_2(TT)_2$** display at 298 K a broad, featureless emission band comprising one fluorescence band (at 421 nm) and one RTUP band (at about 550 nm), which were associated with the π–π dimers. The fluorescence/RTUP intensity ratio is higher in **$[Cd(H_2O)_6](ClO_4)_2(TT)_2$** than **$[Zn_3(CH_3COO)_6(H_2O)_2](TT)_2$**, indicating that RTUP is more sensitive to the supramolecular organization of the chromophores themselves (columns *vs.* dimers) rather than to the extrinsic heavy atom effect.

The different heavy atom effect exerted by Cd *vs.* Zn was highlighted by comparing **$[Cd(H_2O)_6](BF_4)_2(TT)_2$** and **$[Zn(H_2O)_6](BF_4)_2(TT)_2$** both showing one fluorescence band (at 383 and 370 nm, respectively) and one RTUP band (at 441 and 469 nm and 394 and 422 nm, respectively). The latter possesses a shorter triplet lifetime in the cadmium complex compared to zinc (τ = 125 ms and 542 ms, respectively), indicating higher SOC in the former.

The observed emission red-shift of **$[Cd(H_2O)_6](ClO_4)_2(TT)_2$** with respect to the two other isostructural compounds was associated with the different counter ions through DFT and TDDFT calculations on **TT**·ClO_4^- and **TT**·BF_4^- interacting units. In fact, while HOMOs of **TT**·BF_4^- are essentially localized on **TT**, those of **TT**·ClO_4^- are delocalized on both interacting units, suggesting in the latter case charge transfer character for the S_0–S_1 transition. The CT character of emissive levels of **$[Cd(H_2O)_6](ClO_4)_2(TT)_2$** was therefore deemed responsible for the observed red shift of its emissions.

Zn(II) and Cd(II) coordination compounds with **TT** have also been obtained, in particular the cationic **$[Zn(TT)(NO_3)(H_2O)_3](NO_3)$** and the neutral **$[Cd(TT)_2(NO_3)_2(H_2O)_2]$** complexes where **TT** ligands form infinite stacking columns with **TT-TT** distances much shorter in the former (the distance between triazine geometric centroids equal to 3.85 Å *vs.* 4.88–4.94 Å).[124]

Crystals of the zinc complex display an intense fluorescence band (at 439 nm) with a long-lived tail (at about 550 nm) (overall Φ = 1%), which was assigned, due to crystallographic considerations, to π–π aggregates of the ligand. Comparison of the photophysical parameters (quantum yields and lifetimes) of **$[Zn(TT)(NO_3)(H_2O)_3](NO_3)$** with those of **TT** itself and the **$[Zn_3(CH_3COO)_6(H_2O)_2](TT)_2$** cocrystal, having a similar organization of **TT** inside the structure, allowed us to conclude that the presence of Zn(II) facilitates depopulation of S_1 through ISC to a triplet level with $k_r < k_{nr}$, with the intrinsic (coordination) effect being more pronounced than the extrinsic (cocrystal) one.

Crystals of **$[Cd(TT)_2(NO_3)_2(H_2O)_2]$** at 298 K show one fluorescence band (at 430 nm) and one phosphorescence band (at 505 nm), which, again based on crystallographic considerations, were identified as ligand-centered emissions.

The versatility of **TT** as a coordinating ligand is also manifested in the isolation of several Cu(I) and Ag(I) coordination polymers (CPs), ranging from 1D chains to 3D coordination networks, in which **TT** is either a monodentate or bi- and tridentate bridging ligand.[125,126] Among these, two Cu and three Ag CPs were obtained with the required high purity grade for reliable photophysical measurements. In particular, 1D double-stranded stair **$[MI(TT)]_n$** and 3D **$[MCl(TT)]_n$** (M = Cu, Ag) isostructural polymers and a 3D Ag(I) derivative, namely **$[Ag_3(TT)_4]_n(NO_3)_{3n}{\cdot}6nH_2O$**, were isolated and characterized. **$[MI(TT)]_n$** crystallized in the monoclinic $P2_1/c$ space group forming double-stranded stairs of $[MI]_n$ composition, decorated on both sides with monodentate **TT** ligands. The **TT** ligands on both sides of the chains are all parallel and superimposed allowing π–π stacking interactions.

Crystals of **$[MI(TT)]_n$** display an excitation dependent emissive behaviour. For crystals of **$[AgI(TT)]_n$** at 298 K one fluorescence band at 385 nm and three phosphorescence bands (HEP at 411 and 445 nm, MEP at 446, 476 and 509 nm, and LEP at 494, 530, 575, 620 and 680 nm) were visible (overall Φ equal to 19%). For **$[CuI(TT)]_n$** at an appropriate excitation wavelength three phosphorescence bands were observed (Φ = 18%). Two of them (MEP at 431, 460 and 487 nm and LEP at 536, 582 and 623 nm) fall in the same spectral range as that of **$[AgI(TT)]_n$**, while the third one (at 568 nm), activated only by exciting at high energy (λ_{exc} < 390 nm), is specific for **$[CuI(TT)]_n$** and assigned to a ^{3}XMLCT state. Based on structural considerations, LEP was associated with π–π stacking interactions between **TT** units and MEP was associated with I···C intermolecular electronic coupling, also in view of its similarity, in both position and shape, with that observed in **1I** and **TT·DITFB**.[71] The structures of these four compounds are in fact characterized by comparable I···C contacts between adjacent stairs (in **$[MI(TT)]_n$**), helices (in **1I**) and chains (in **TT·DITFB**). The similarity of LEP and MEP in the two isostructural **$[MI(TT)]_n$** polymers was a clear indication that the metal plays a secondary role in these emissions and can be therefore referred to as an "external" perturber. Ag(I) HEP was interpreted as due to deactivation of a ligand centered triplet state as supported by the energy spacing (about 1300–1550 cm^{-1}) of its vibrational components, which can be associated with a vibronic progression involving imidazole ring modes. The absence of fluorescence and HEP in **$[CuI(TT)]_n$** was justified, through theoretical studies, with the greater metal contribution to the intramolecular emissive behaviour of copper resulting in the

This journal is © The Royal Society of Chemistry 2025

Open Access Article. Published on 20 January 2025. Downloaded on 1/21/2026 10:55:07 PM.
This article is licensed under a Creative Commons Attribution-NonCommercial 3.0 Unported Licence.

suppression of fluorescence through easy ISC to close triplets and activation of the XMLCT phosphorescence.[127]

3D coordination polymers **[MCl(TT)]**$_n$ crystallize in the cubic space group $Pa\bar{3}$. Unlike **[MI(TT)]**$_n$ polymorphs, the **TT** ligand uses the nitrogen atoms of all of its three imidazole moieties to coordinate the metal atoms. Moreover, the ligands are also involved in π–π stacking interactions. At 298 K, crystals of **[AgCl(TT)]**$_n$ display an excitation-dependent emission spectrum comprising one fluorescence band (at 448 nm) and two superimposed phosphorescence bands (in the 530–615 nm range), one of molecular origin and the other assigned to **TT-TT** π–π dimers. For **[CuCl(TT)]**$_n$ only two long-lived emissions (at 515 and 560 nm) were observed, with the lowest energy one assigned as well to π–π dimers and the other to a molecular triplet. Again, the presence of fluorescence for the Ag(I) polymorph was interpreted as due to a reduced metal contribution of Ag(I) with respect to Cu(I) in the emitting states.[127]

The 3D coordination polymer **[Ag$_3$(TT)$_4$]**$_n$**(NO$_3$)**$_{3n}$**·6*n*H$_2$O** crystallizes in the cubic space group $I\bar{4}3d$ with each silver atom coordinated to four **TT** molecules in a distorted tetrahedral environment and no stacking interactions between **TT** molecules. Its crystals display at 298 K (Φ equal to 7.5%) excitation-dependent emissions comprising a broad fluorescence band (at 404 nm) and two phosphorescence bands (at 454 and 556 nm), which were related, according to DFT/TDDFT calculations, to triplet states of different nature indicating anti-Kasha behaviour.

3.3.6b TT-COOH as a ligand. Functionalization of **TT** with a carboxylic group provides additional sites for metal coordination. Therefore, **TT-COOH** was reacted with different metal salts resulting in isostructural complexes, namely **[M(TT-COO)$_2$(H$_2$O)$_2$]** (M = Mn(II), Co(II), Ni(II), Cu(II), Zn(II), Cd(II)).[89] They crystallize in the triclinic $P\bar{1}$ space group where the deprotonated **TT-COO**$^-$ residue coordinates in an *N*,*O*-bidentate chelate coordination mode forming a rare-met seven-membered metallochelate ring giving an extended H-bonded layer. Adjacent layers stack in a zip-like mode with partial overlap of coordinated luminophores.

Crystals of zinc and cadmium complexes, the only emissive in this series (Φ = 9 and 1.4%, respectively), display a photophysical behaviour quite similar to that of free **TT-COOH**. This suggests an external role of the metal (whose evidence is limited to a lower quantum yield in metal containing derivatives) as supported by DFT-TDDFT calculations. In fact, similarly to **TT-COOH**, two molecular fluorescence components (HEF at 338 and 352 nm for Zn and Cd, respectively; LEF at 382, 405 and 430 for both compounds) and phosphorescence components (HEP at 452 nm, MEP at 490 and 523 nm, respectively) with anti-Kasha behaviour were observed for the two complexes (Fig. 41). Moreover, an additional LEP (at 556 and 577 nm, respectively) of π–π stacked origin was present in the PL spectrum of the compounds.

3.3.6c TT-Py as a ligand. The coordination properties of **TT** can also be enhanced by insertion of pyridinic moieties (**TT-Pys**) through appropriate coupling reaction starting from ***n*Br**. This leads to the engineering of new extended hybrid supramolecular systems in which **TT-Py**s can act as mono-, bi- and tri-dentate ligands.

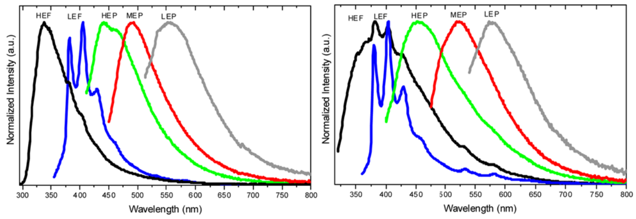

Fig. 41 Normalized PL emission spectra at RT. Left: crystals of **[Zn(TT-COO)$_2$(H$_2$O)$_2$]** λ_{exc} = 280 nm (black); 340 nm (blue); 390 nm (green); 435 nm (red) and 493 nm (grey). Right: crystals of **[Cd(TT-COO)$_2$(H$_2$O)$_2$]** λ_{exc} = 300 nm (black); 340 nm (blue); 390 nm (green); 454 nm (red) and 523 nm (grey).

A series of Cu(II) coordination compounds with pyridine-substituted derivatives, namely 3-(pyridin-2-yl)triimidazo[1,2-*a*:1′,2′-*c*:1″,2″-*e*][1,3,5]triazine (**TT-2Py**) and 3-(pyridin-4-yl)-triimidazo[1,2-*a*:1′,2′-*c*:1″,2″-*e*][1,3,5]triazine (**TT-4Py**), were reported.[128] In particular, a mononuclear complex **[Cu(NO$_3$)$_2$-(H$_2$O)$_2$(TT-4Py)$_2$]·2H$_2$O**, a binuclear one **[Cu$_2$(CH$_3$COO)$_4$(TT-2Py)$_2$]**, and a 1D coordination polymer **[Cu(NO$_3$)$_2$(TT-2Py)]**$_n$, where luminophores coordinate to the metal ion as either monodentate terminal ligands or bidentate-chelate ones, were obtained. In spite of the rich variety of structural patterns, accommodating both hydrogen bonds and π···π stacking interactions with different overlapping areas of the stacking ligands, the compounds are scarcely emissive in agreement with the paramagnetic character of the Cu(II) ion.

The ability of **TT-2Py** to act as a chelating ligand giving a seven-membered metallacycle through the nitrogen atom of the pyridinic ring and the other on the imidazolic unit, as observed in **[Cu(NO$_3$)$_2$(TT-2Py)]**$_n$, was exploited for the preparation of other coordination compounds. In particular, **TT-2Py** was reacted with Re(I) and Cu(I) further evidencing its versatility in adopting different coordination modes.

With Re(I), a mononuclear (**[ReCl(CO)$_3$(TT-2Py)]**) and a hexanuclear species (**[{Re(μ-Cl)(CO)$_3$(μ-TT-2Py)}{Re$_2$(μ-Cl)$_2$(CO)$_6$}]$_2$**) were isolated.[129] In the mononuclear complex the rhenium atom attains an octahedral geometry and bears three terminal carbonyl ligands in a facial arrangement, one terminal chloro ligand and two nitrogen atoms of the chelating **TT-2Py** ligand (Fig. 42), namely the nitrogen atom of the pyridyl substituent and the nitrogen atom of the triimidazotriazine moiety, similarly to what is observed in **[Cu(NO$_3$)$_2$(TT-2Py)]**$_n$. The hexanuclear species contains two **[ReCl(CO)$_3$(TT-2Py)]** moieties with geometry quite similar to the one of the mononuclear complexes, which bridge two additional [Re$_2$(μ-Cl)$_2$(CO)$_6$] fragments through the chloro ligand and a nitrogen atom of the triimidazotriazine moiety (Fig. 43).

The absorption and emission spectra of the two complexes were recorded in dilute DCM and toluene solutions, respectively. The mononuclear derivative shows two broad absorption bands at 247 and 301 nm both of which, based on DFT/TDDFT calculations, are assigned to MLCT + XLCT states. Moreover, for the lower energy transition, an additional ILCT contribution

Open Access Article. Published on 20 January 2025. Downloaded on 1/21/2026 10:55:07 PM.
This article is licensed under a Creative Commons Attribution-NonCommercial 3.0 Unported Licence.

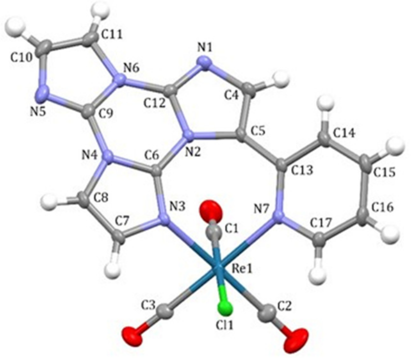

Fig. 42 View of the rhenium complex **[ReCl(CO)$_3$(TT-2Py)]** as found in its crystal structure, with a partial labelling scheme. Ellipsoids are drawn at the 50% probability level. Reproduced from ref. 129 under the terms of the Creative Commons license and with permission from the Royal Society of Chemistry. Copyright 2023.

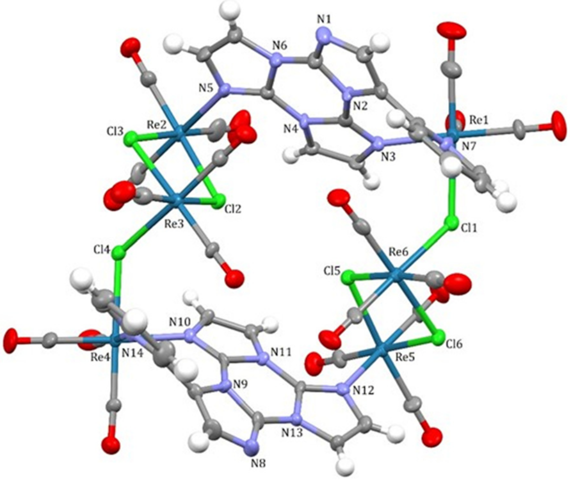

Fig. 43 View of the rhenium complex **[{Re(μ-Cl)(CO)$_3$(μ-TT-2Py)}{Re$_2$(μ-Cl)$_2$(CO)$_6$}]$_2$** as found in the crystal structure of its *n*-hexane solvate, with a partial labelling scheme. Ellipsoids are drawn at the 50% probability level. Reproduced from ref. 129 under the terms of the Creative Commons license and with permission from the Royal Society of Chemistry. Copyright 2023.

was predicted from calculations. The hexanuclear species displays absorption bands at 234, 264 and 320 nm, with a shoulder at 346 nm with not clearly established origin.

Upon excitation at 365 nm, the two compounds display a broad unstructured phosphorescence band (at 583 and 597 nm, Φ = 0.4 and 0.01%, for the mono- and the hexanuclear species, respectively). In the solid state, both derivatives maintain the structureless profile with a concomitant important hypsochromic shift of the phosphorescence maxima (532 and 563 nm, respectively) and increase in the photoluminescence quantum yield (12 and 2.5%, respectively). Such AIE features were attributed to restriction of the vibrational motions.

By mixing copper iodide with **TT-2Py** in ACN at 298 K in a 2 : 1 molar ratio, an orange emissive solid, namely **[Cu$_2$I$_2$(TT-2Py)]$_n$**, was obtained.[130] This Cu(I) CP, crystallizing in the $P2_1/n$ space group, is characterized by a quite rare crystal structural motif, comprising a double-stranded (CuI)$_2$ stair and a single CuI zig-zag chain (Fig. 44), which, among copper(I) halide based compounds, was reported in the literature only once previously (CSD Refcode GAJBEB[131]).

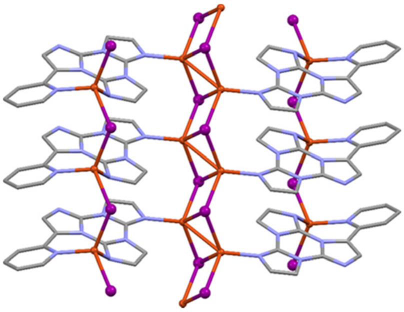

Fig. 44 View of a single monodimensional chain of **[Cu$_2$I$_2$(TT-2Py)]$_n$** showing the central double stranded stair and the two lateral single zig-zag structural motifs bridged by the ligand. Reproduced from ref. 130 under the terms of the Creative Commons CC BY license. Copyright 2023 by the authors. Licensee MDPI, Basel, Switzerland.

Powders of **[Cu$_2$I$_2$(TT-2Py)]$_n$** display at 298 K an orange broad excitation independent emission of XMLCT character centered at 588 nm (quantum yield, Φ, equal to 7%; τ = 1.33 μs) shifted to 580 nm (τ = 17.89 μs) at 77 K (Fig. 45). Based on the one order of magnitude increase of lifetime upon cooling (from 298 to 77 K) and on the presence of a triplet almost isoenergetic with S$_1$, a TADF mechanism at the origin of the single emission of **[Cu$_2$I$_2$(TT-2Py)]$_n$** was not fully excluded.

To further investigate the coordination ability of the **TT** ligands, the tri-pyridinic substituted derivative, namely 3,7,11-tri(pyridin-4-yl)triimidazo[1,2-*a*:1′,2′-*c*:1″,2″-*e*][1,3,5]triazine, hereafter **TT-4Py$_3$**, having three pyridyl groups with nitrogen atoms in the *para*-position with respect to **TT** and oriented with a trigonal symmetry, was synthesized and reacted with Ag(I), Cd(II) and Cu(I).[132] Three layered CPs, **[Ag{(TT-4Py$_3$}(SO$_3$CF$_3$)]$_n$·$\frac{1}{2}n$CH$_2$Cl$_2$**, **[Cd{TT-4Py$_3$}(NO$_3$)$_2$(EtOH)]$_n$** and **[(Cu$_2$I$_2$)$_3${TT-4Py$_3$}$_4$]$_n$·*xn*(H$_2$O,EtOH)** were obtained and characterized by SCXRD, XRPD, IR and photoluminescence spectroscopies and their emissive

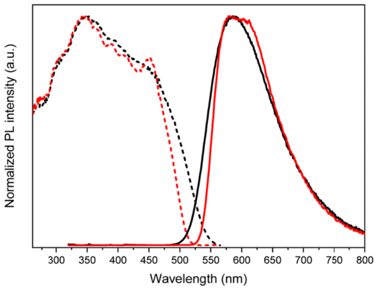

Fig. 45 Normalized excitation (dashed) and PL emission (continuous) spectra of crystalline powders of **[Cu$_2$I$_2$(TT-2Py)]$_n$** at 298 K (black, λ_{em} = 588 nm; λ_{exc} = 300 nm) and 77 K (red, λ_{em} = 580 nm; λ_{exc} = 300 nm). Reproduced from ref. 130 under the terms of the Creative Commons CC BY license. Copyright 2023 by the authors. Licensee MDPI, Basel, Switzerland.

Open Access Article. Published on 20 January 2025. Downloaded on 1/21/2026 10:55:07 PM.
This article is licensed under a Creative Commons Attribution-NonCommercial 3.0 Unported Licence.

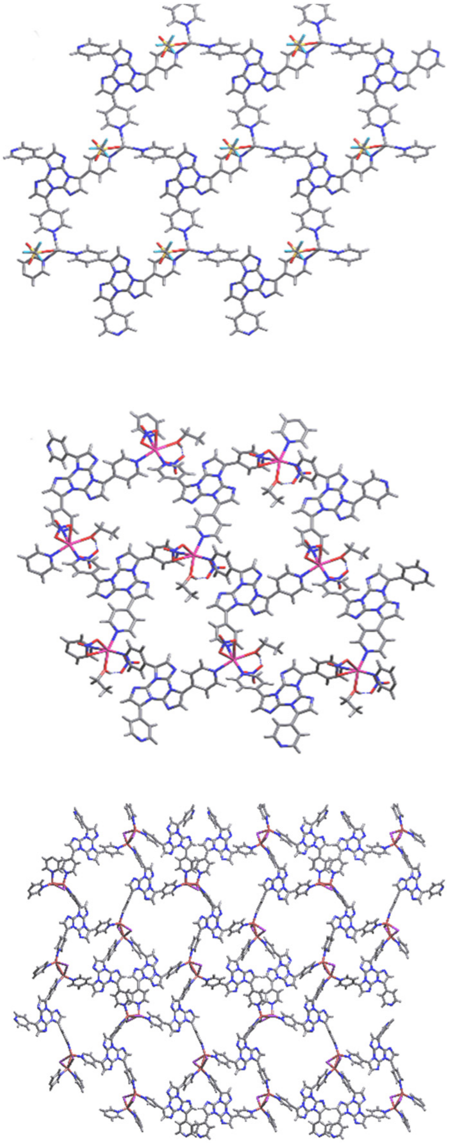

Fig. 46 Crystal structures of **[Ag{(TT-4Py$_3$}(SO$_3$CF$_3$)]$_n$·$\frac{1}{2}n$CH$_2$Cl$_2$**, **[Cd{TT-4Py$_3$}(NO$_3$)$_2$(EtOH)]$_n$** and **[(Cu$_2$I$_2$)$_3${TT-4Py$_3$}$_4$]$_n$·*xn*(H$_2$O,EtOH)**: views of a single molecular layer down the [1, 1, −1], [1, 0, −2] and [1, 0, 1] directions for **[Ag{(TT-4Py$_3$}(SO$_3$CF$_3$)]$_n$·$\frac{1}{2}n$CH$_2$Cl$_2$** (top), **[Cd{TT-4Py$_3$}(NO$_3$)$_2$(EtOH)]$_n$** (middle) and **[(Cu$_2$I$_2$)$_3${TT-4Py$_3$}$_4$]$_n$·*xn*(H$_2$O,EtOH)** (bottom). Adapted with permission from ref. 132. Copyright 2024, John Wiley and Sons.

properties were interpreted with the aid of DFT/TDDFT calculations.

[Ag{(TT-4Py$_3$}(SO$_3$CF$_3$)]$_n$·$\frac{1}{2}n$CH$_2$Cl$_2$ and **[Cd{TT-4Py$_3$}(NO$_3$)$_2$(EtOH)]$_n$** crystallize, respectively, in $P2_1/c$ and $P\bar{1}$ space groups to give very similar 2D coordination motifs, where the ligand acts as a trigonal donor through the pyridyl nitrogen atoms bridging three different metal ions, so that each metal is coordinated to three different ligands (Fig. 46). **[(Cu$_2$I$_2$)$_3${TT-4Py$_3$}$_4$]$_n$·*xn*(H$_2$O,EtOH)** crystallizes in the $P2_1/c$ space group without significant inter-layer interactions between aromatic fragments except for a short distance (3.735 Å) between the triazinic centroids of two **TT-4Py$_3$** ligands belonging to two parallel neighboring layers (Fig. 46), according to quite strong I···π halogen bonds.[133–138] Powders of **TT-4Py$_3$** and crystals of **[Ag{(TT-4Py$_3$}(SO$_3$CF$_3$)]$_n$·$\frac{1}{2}n$CH$_2$Cl$_2$** and **[Cd{TT-4Py$_3$}(NO$_3$)$_2$(EtOH)]$_n$** display excitation dependent emissive behaviour while those of **[(Cu$_2$I$_2$)$_3${TT-4Py$_3$}$_4$]$_n$·*xn*(H$_2$O,EtOH)** are characterized by a single, broad, excitation independent emission. In more detail, **TT-4Py$_3$** shows at 298 K and an appropriate excitation wavelength, one fluorescence band (at 365 nm) and two phosphorescence bands (at 458 and 549 nm). Similarly, crystals of **[Ag{(TT-4Py$_3$}(SO$_3$CF$_3$)]$_n$·$\frac{1}{2}n$CH$_2$Cl$_2$** show at 298 K one fluorescence band (at 390 nm) and two phosphorescence bands (at 460 and 530 nm) (overall $\Phi \cong 1\%$, Fig. 47). At 77 K the three emissions are still visible in slightly different positions (at 395 nm; 450 nm; 510, 548, 592 and 655 nm, respectively) but with different relative intensities with respect to that observed at room temperature suggesting different deactivation paths at the two temperatures.

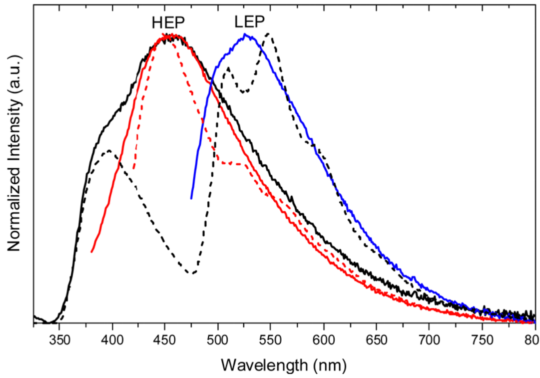

Fig. 47 Normalized PL emission spectra of **[Ag{(TT-4Py$_3$}(SO$_3$CF$_3$)]$_n$·$\frac{1}{2}n$CH$_2$Cl$_2$** crystals at 298 K (full lines) and 77 K (dashed lines); λ_{exc}: 300 nm (black lines); 358 nm (red full line); 400 nm (red dashed line) and 460 nm (blue line). Adapted with permission from ref. 132. Copyright 2024, John Wiley and Sons.

Crystals of **[Cd{TT-4Py$_3$}(NO$_3$)$_2$(EtOH)]$_n$** display at 298 K and an appropriate excitation wavelength (Fig. 48), one fluorescence band (at about 405 nm) and two phosphorescence bands (at about 455 and 550 nm, overall $\Phi \cong 15\%$), slightly shifted and better vibronically resolved at 77 K (at 346, 365, 381, 403 and 421 nm; 450 nm; 498 and 536 nm, respectively).

Interestingly, in both **[Ag{(TT-4Py$_3$}(SO$_3$CF$_3$)]$_n$·$\frac{1}{2}n$CH$_2$Cl$_2$** and **[Cd{TT-4Py$_3$}(NO$_3$)$_2$(EtOH)]$_n$**, the presence of the metal results in a red shift of the fluorescence with respect to that observed for the free ligand, while it does not affect the phosphorescence emission maxima. The latter were assigned to molecular (HEP) and supramolecular (LEP) contributions (π–π stacking arrangement of the ligands).

DFT/TDDFT calculations on both the isolated ligand and discrete models of the two compounds, comprising the metal ion and its full coordinating sphere, revealed that the set of singlet and triplet excited states display an alternation of pure (π,π*) and mixed (σ/π,π*) levels, with the σ contribution mainly located on the pyridine moieties. While for **TT-4Py$_3$** the lower energy singlet states have mixed $^1(\sigma/\pi,\pi^*)$ (S$_1$) or pure $^1(\sigma,\pi^*)$ character ($S_2 \div S_4$), and T$_1$ is a $^3(\pi,\pi^*)$ state, coordination to the

Open Access Article. Published on 20 January 2025. Downloaded on 1/21/2026 10:55:07 PM.
This article is licensed under a Creative Commons Attribution-NonCommercial 3.0 Unported Licence.

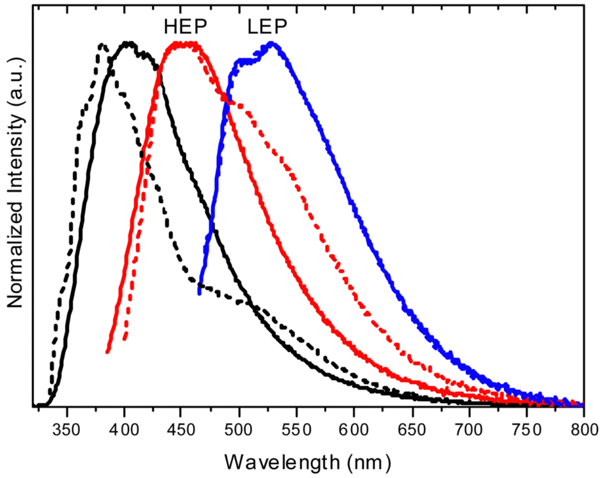

Fig. 48 Normalized PL emission spectra of **[Cd{TT-4Py$_3$}(NO$_3$)$_2$(EtOH)]$_n$** crystals at 298 K (full lines) and 77 K (dashed lines); λ_{exc}: 300 nm (black lines); 370 nm (red full line); 380 nm (red dashed line) and 450 nm (blue lines). Adapted with permission from ref. 132. Copyright 2024, John Wiley and Sons.

Ag(I) and Cd(II) ions results in stabilization of the (π,π*) singlets, which are located at lower energy with respect to the almost unvaried ^{1}(σ/π,π*) and ^{1}(σ,π*) ones. The low energy triplets, instead, remain almost unperturbed. This explains the observed red shift of the fluorescence emission, differently from HEP which remains energetically unaffected by complexation. Moreover, inspection of the orbitals mainly involved in the transitions revealed that in both compounds LUMOs and HOMOs are essentially ligand-centered. Only for **[Ag{(TT-4Py$_3$}(SO$_3$CF$_3$)]$_n$·$\frac{1}{2}$*n*CH$_2$Cl$_2$**, however, a partial, non-negligible delocalization on the metal was calculated, resulting in a modest MLCT contribution. The absence of a metal contribution in the transitions of **[Cd{TT-4Py$_3$}(NO$_3$)$_2$(EtOH)]$_n$** explained its much higher quantum yield compared to that of **[Ag{(TT-4Py$_3$}(SO$_3$CF$_3$)]$_n$·$\frac{1}{2}$*n*CH$_2$Cl$_2$**, due to the reduction, in the former, of the 'detrimental' (from this point of view) path towards the phosphorescence emission.

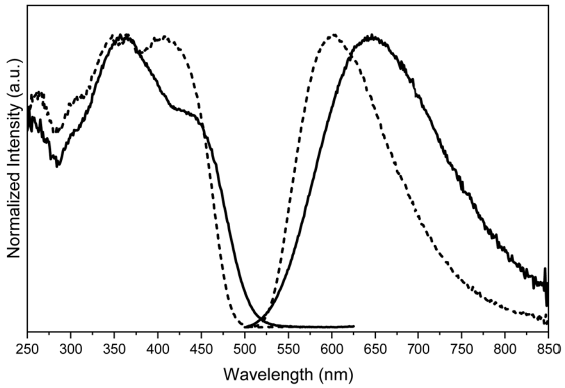

Fig. 49 Normalized PL emission (λ_{exc}: 360 nm) and excitation spectra of **[(Cu$_2$I$_2$)$_3${TT-4Py$_3$}$_4$]$_n$·*xn*(H$_2$O,EtOH)** crystals at 298 K (full line) and 77 K (dashed lines); (λ_{em}: 645 nm full line, 602 nm dashed line). Reproduced with permission from ref. 132. Copyright 2024, John Wiley and Sons.

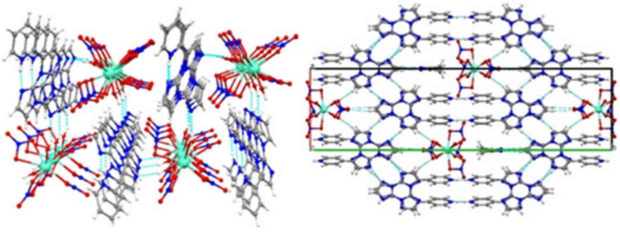

Fig. 50 Left: crystal structure of **(TT-2PyH)[Eu(NO$_3$)$_4$(H$_2$O)$_2$]**: fragment of the H-bonded layer. Right: crystal structure of **(TT-4PyHTT-4Py)$_2$[Eu(NO$_3$)$_5$(H$_2$O)]·(CH$_3$CN)$_2$**: fragment of crystal packing with indication of stabilising short contacts. Adapted with permission from ref. 139. Copyright 2024, American Chemical Society.

The single broad phosphorescence (at about 650 and 606 nm at RT and 77 K, respectively) observed for crystals of **[(Cu$_2$I$_2$)$_3${TT-4Py$_3$}$_4$]$_n$·*xn*(H$_2$O,EtOH)** was associated with multiple contributions mainly related to the ligand itself on the basis of its long lifetime (τ = 6.36 and 34.47 ms at 298 and 77 K, respectively, Fig. 49) and DFT/TDDFT calculations, providing low energy triplet states with prevalent ILCT character.

Reaction of **TT-2Py**, **TT-4Py** and **TT-4Py$_3$** with europium nitrate afforded two salts, namely **(TT-2PyH)[Eu(NO$_3$)$_4$(H$_2$O)$_2$]** and **(TT-4PyHTT-4Py)$_2$[Eu(NO$_3$)$_5$(H$_2$O)]·(CH$_3$CN)$_2$**, where the protonated ligands are accommodated as guests in the crystal lattices, and a neutral complex, **[Eu(NO$_3$)$_3$(H$_2$O)$_2$(TT-4Py$_3$)]**.[139]

(TT-2PyH)[Eu(NO$_3$)$_4$(H$_2$O)$_2$] shows a significant planarization of the **(TT-2PyH)$^+$** cation provided by intramolecular NH···N HBs resulting in supramolecular chains with an alternation of organic and inorganic motifs within the HB layers (Fig. 50 left). The twisted protonated **TT-4Py** ligands in **(TT-4PyHTT-4Py)$_2$[Eu(NO$_3$)$_5$(H$_2$O)]·(CH$_3$CN)$_2$** form packed HB layers with channels accommodating the bulky inorganic anions (Fig. 50 right).

Differently, in **[Eu(NO$_3$)$_3$(H$_2$O)$_2$(TT-4Py$_3$)]**, a direct coordination between one of the *N*-pyridine binding sites of **TT-4Py$_3$** and the Eu(III) metal centre is present (Fig. 51).

Photoluminescence investigation of **(TT-4PyHTT-4Py)$_2$[Eu(NO$_3$)$_5$(H$_2$O)]·(CH$_3$CN)$_2$** and **[Eu(NO$_3$)$_3$(H$_2$O)$_2$(TT-4Py$_3$)]** revealed a broad unstructured triazinic ligand-based emission with very small Eu(III) contribution for the former and an efficient ligand–metal energy transfer for the latter, as manifested by its bright red emission comprising only the characteristic emissive features of Eu(III).

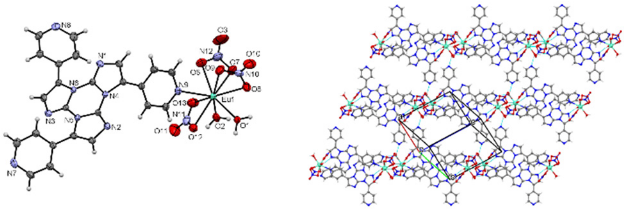

Fig. 51 Crystal structure of **[Eu(NO$_3$)$_3$(H$_2$O)$_2$(TT-4Py$_3$)]**. Left: The molecule of **[Eu(NO$_3$)$_3$(H$_2$O)$_2$(TT-4Py$_3$)]** with the partial numbering scheme. The thermal ellipsoids are shown at the 50% probability level. Right: fragment of the H-bonded layer. Reprinted with permission from ref. 139. Copyright 2024, American Chemical Society.

Open Access Article. Published on 20 January 2025. Downloaded on 1/21/2026 10:55:07 PM.
This article is licensed under a Creative Commons Attribution-NonCommercial 3.0 Unported Licence.

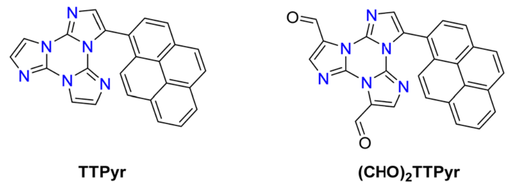

Scheme 19 Chemical structures of **TTPyr** and **(CHO)$_2$TTPyr**.

3.4 Applications of TTs

3.4.1 TTs as sensors for explosive detection. The detection of explosives is one of the major concerns in global security and, in the past few decades, great efforts have been devoted to developing fluorescent sensors for rapid and reliable detection of low amounts of energetic hazardous chemicals and their precursors. Fluorescence-based methods have been extensively studied due to their promising advantages such as high sensitivity, selectivity and low costs; moreover, they are user-friendly and can be easily incorporated into handheld devices.[140,141]

In this scenario, two emissive pyrene derivatives of **TT**, namely **TTPyr** and **(CHO)$_2$TTPyr** (Scheme 19), were proposed as single-molecule fluorescent probes for the detection of various nitroaromatic energetic hazardous materials.[88] The two sensors were investigated by means of fluorescence-quenching titrations in solution through the incremental addition of analytes, comprising a large number of highly energetic molecules and explosives (Scheme 20). A strong attenuation of the emission intensity was observed for both compounds in the presence of nitroaromatics (phenols and toluenes) while negligible effects were recorded with aliphatic or inorganic energetic materials.

Fluorescence quenching titrations were analysed through the Stern–Volmer (SV) equation: $I_0/I = 1 + K_{SV}[Q]$, where I_0 and I are the emission intensities before and after addition of the quencher, respectively, $[Q]$ is the quencher concentration and K_{SV} is the SV constant. For those analytes absorbing in the blue region (*e.g.* nitrophenols) and thus overlapping and affecting the 420 nm **TTPyr** emission according to the secondary inner filter effect, the red-shifted fluorescence of **(CHO)$_2$TTPyr** at 565 nm represented a valid alternative. Evaluation of the interaction strength between probes and analytes, by means of K_{SV} and limit of detection (LOD) calculations, provided values that are quite comparable for both **TT** probes (Table 1), according to the following order: aliphatic and inorganic explosives < nitrotoluenes < nitrophenols, with the strongest response in the case of picric acid (PA).

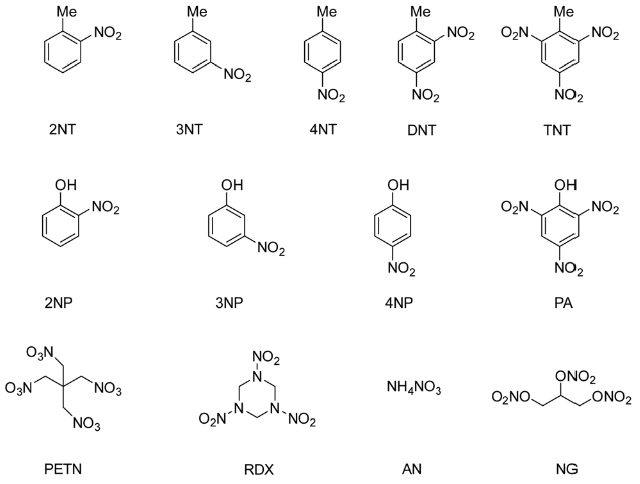

Scheme 20 List of explosives tested with **TTPyr** and **(CHO)$_2$TTPyr** probes.

Table 1 List of the Stern–Volmer constants and LODs obtained from intensity data at 420 nm for **TTPyr** and at 565 nm for **(CHO)$_2$TTPyr**, (λ_{exc} = 350 nm). For the data set of **TTPyr** with PA, 3NP and 2NP data are calculated on the emission intensity at 490 nm while for 4NP at 500 nm in order to minimize the secondary inner filter effect

	TTPyr		**(CHO)$_2$TTPyr**	
Explosive	K_{SV} (M^{-1})	LOD (μM)	K_{SV} (M^{-1})	LOD (μM)
RDX	$2.30 \times 10^{+2}$	113	$1.66 \times 10^{+2}$	164
PETN	$1.74 \times 10^{+2}$	114	$-1.15 \times 10^{+1}$	—
NG (dynamite)	$2.00 \times 10^{+2}$	126	$2.17 \times 10^{+1}$	880
AN	$1.89 \times 10^{+2}$	120	$1.54 \times 10^{+2}$	146
2NT	$1.71 \times 10^{+3}$	18.15	$4.70 \times 10^{+2}$	41.62
3NT	$2.57 \times 10^{+3}$	17	$5.34 \times 10^{+2}$	30.5
4NT	$9.75 \times 10^{+2}$	28.41	$5.79 \times 10^{+2}$	29.57
DNT	$1.31 \times 10^{+3}$	18.46	$1.06 \times 10^{+3}$	31.76
TNT	$2.17 \times 10^{+3}$	8.2	$1.45 \times 10^{+3}$	10.27
2NP	$3.48 \times 10^{+3}$	12.56	$4.86 \times 10^{+3}$	3.66
3NP	$1.81 \times 10^{+3}$	24.13	$4.90 \times 10^{+3}$	7.58
4NP	$8.99 \times 10^{+3}$	4.87	$1.12 \times 10^{+4}$	2.53
PA	$1.46 \times 10^{+4}$	2.85	$1.25 \times 10^{+4}$	2.76

Moreover, time-resolved measurements in the absence and in the presence of increasing concentration of PA or TNT were performed on **TTPyr** with the aim to discriminate between static or dynamic quenching. The results showed constant excited state lifetimes even at very high quencher concentration, suggesting a static quenching with formation of a non-emissive dark-complex between the probe and the analyte in the ground state. Such evidence was further supported by the isolation and characterization by SCXRD of a **TTPyr**/PA adduct with 2 : 1 stoichiometry.

In the panorama of highly energetic molecules, **TT** was used as a stabilizer of all-carbon-nitrated azoles, usually suffering from drawbacks such as poor thermal stability, frictional and impact sensitivities, deliquescence and hydrolysis.[142,143] By exploiting the donor properties of the electron-rich **TT** scaffold, three cocrystals with electron-poor acceptors, namely 5-nitrotetrazole (HNT), 3,5-dinitro-1,2,4 triazole (HDNT) and 3,4,5-trinitropyrazole (TNP), were prepared (Fig. 52).[144] All

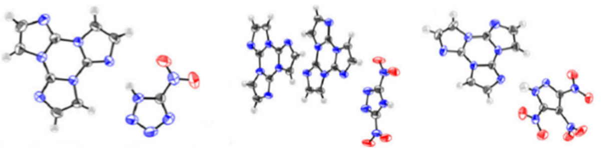

Fig. 52 Crystal structures of: (left) 1 : 1 **TT**/HNT cocrystals, (middle) 2 : 1 **TT**/HDNT cocrystals and (right) 1 : 1 **TT**/TNP cocrystals. Displacement ellipsoids are shown at the 50% probability level. Adapted with permission from ref. 144. Copyright 2022, American Chemical Society.

Open Access Article. Published on 20 January 2025. Downloaded on 1/21/2026 10:55:07 PM. This article is licensed under a Creative Commons Attribution-NonCommercial 3.0 Unported Licence.

cocrystals exhibited better performances, in terms of thermal stability and mechanical sensitivity, with respect to the pure azole components. By means of SCXRD and theoretical calculations it was suggested that the combination of strong hydrogen bonds (N–H···N, C–H···N, and C–H···O) and weak $NO_2\cdots\pi$ and π-stacking interactions encountered in the highly energetic adducts could be responsible for their significantly improved performances.

3.4.2 TTs as ligands for bioimaging. The AIE and RTP features displayed by several **TTs** represent an intriguing starting point for the development of organic luminescent materials for screening, diagnosis and treatment in biomedical applications. In fact, AIE allows exploiting a wide range of molecules, including polyaromatic hydrocarbons, usually showing great photoemissive properties but low solubility in biological media.[145,146] RTP, owing to its unique long-lived signals, is particularly suitable for advanced bioimaging since it allows minimizing or even fully removing the background interference due to autofluorescence from endogenous fluorophores in biological tissues. Moreover, due to triplet exciton population, RTP probes can play an active role in phototheranostics thanks to singlet oxygen and ROS generation.[95,147]

To this scope, **TTPyr** was selected as the test compound due to its luminescence properties such as long-lived emission, tunable emission range and high quantum yields both in solution and as a solid phase.[80] Evaluation of **TTPyr** emissive behaviour in DMSO by adding increasing amounts of a non-solvent (water) showed a gradual increase and a concomitant blue shift of the emission from 420 to 400 nm by increasing the water content up to 70% in volume (Fig. 53 left). Further water addition resulted in an attenuation of this emission with appearance of an additional low energy fluorescence component (associated with aggregated species) at 480 nm, the wavelength suitable for bacteria and cell imaging studies. Staining experiments with eukaryotic (HeLa and HLF) and prokaryotic (*S. aureus* and *E. coli*) cells revealed, through confocal laser scanning microscopy, that **TTPyr** can enter both type of cells at low concentration in an appropriate time window, locating at cytoplasm level (Fig. 53 right). In addition, MTT assays pointed out the good biocompatibility properties of **TTPyr**, characterized by distinct cytotoxicity towards cancer cells rather than normal cells. These findings provide useful insights and indications to further expand the **TT** family aiming at the development of probes for the intracellular environment sensing to be potentially applied as luminescent drugs for anticancer and phototheranostic studies.

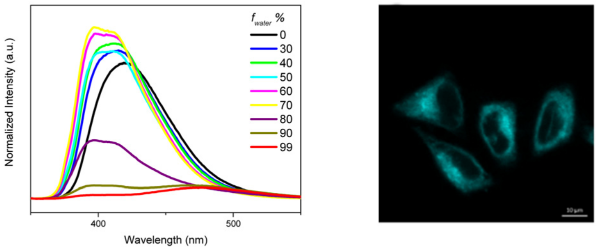

Fig. 53 Left: PL emission spectra of **TTPyr** (10^{-5} M) in DMSO/H_2O mixtures with different water fractions (f_{water}) at RT (λ_{exc}= 340 nm). Right: HeLa cell co-staining experiment (**TTPyr** 10 μM). Adapted with permission from ref. 80. Copyright 2021, John Wiley and Sons.

3.4.3 TTs as ligands for G-quadruplex structures. There is an extensive and ongoing research on the development of 1,3,5-triazine derivatives for their biological activity in different fields spanning from anticancer, antimalarial, antibacterial, antifungal to antiviral applications.[16,148] In this regard, **TT** derivatives represent promising candidates to be investigated as DNA stabilizing agents, since they share certain structural features with known G-quadruplex binding ligands.

G-Quadruplexes (G4) are non-canonical secondary structures of DNA or RNA nucleic acids that self-folds in regions rich in guanine bases organized in planar layers of four guanines (G-quartets), which are repeated inside the biopolymer sequence.[149,150] Intriguingly, it has been reported that putative G4-forming sequences are present in genomic regions and they are involved in several pathologies, such as cancer or viral infections, where they can promote or rule the genetic information transfer. Additionally, they are found to have a role in DNA repair and maintenance,[151,152] and hence there is interest in targeting G4s as an appealing and novel promising antitumor strategy.[150,153,154] There is rich literature on G4 ligands, which are characterized by some common structural features such as the presence of large planar aromatic systems, able to stack with the planar G-quartets, and the presence of polar or positively charged tails, which interact with the negatively

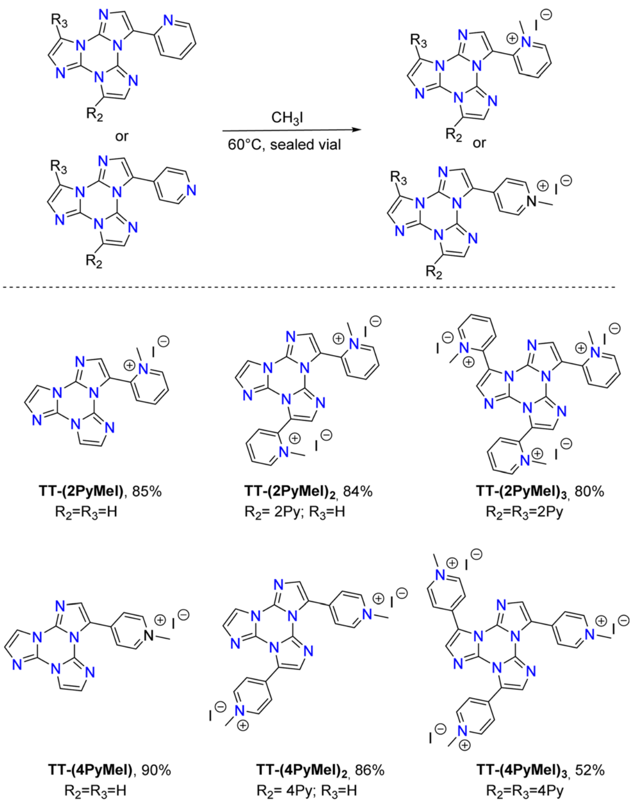

Scheme 21 Preparation of **TT-(2PyMeI)$_n$** and **TT-(4PyMeI)$_n$**.

Open Access Article. Published on 20 January 2025. Downloaded on 1/21/2026 10:55:07 PM.
This article is licensed under a Creative Commons Attribution-NonCommercial 3.0 Unported Licence.

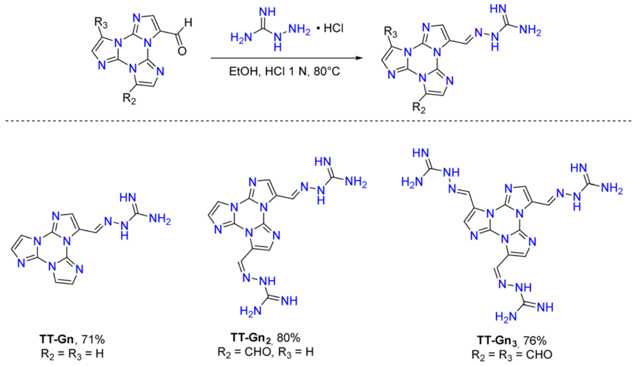

Scheme 22 Preparation of **TT-Gn$_x$** (x = 1–3).

charged phosphate DNA backbone and the grooves and loops of G4s.[155–157] Based on these observations, the flat aromatic **TT** was appropriately functionalized by the introduction of polar and hydrophilic groups. In particular, **TT-2Py$_n$** and **TT-4Py$_n$** series were methylated on the pyridinic nitrogen, resulting in water soluble salts with the positive charge at different distances from the central core (Scheme 21).[78]

In parallel, a family of polar guanyl hydrazones **TT-Gn$_x$** (x = 1–3) were synthesized through imination of the corresponding formyl-**TT-(CHO)$_x$** with aminoguanidine hydrochloride (Scheme 22).[158,159]

The methyl pyridinium and guanyl hydrazone **TTs** were tested as G4 stabilizers by using sequences from the oncogene promoter regions of BCL-2, c-KIT, c-MYC (BCL2 G4, c-KIT2 G4 and c-MYC G4, respectively) and a 26-mer truncation of the human telomeric DNA sequence (Tel26 G4). A biophysical *in vitro* screening of the ligands was carried out by circular dichroism (CD) analysis and CD-melting experiments, to evaluate the ability of the synthesized compounds to interact and stabilize the G4 targets. The results revealed a noteworthy G4-stabilizing effect for most of the tested compounds even at low concentrations, with stabilization increasing with the number of substituents on the **TT** core (Table 2). Moreover, a comparison of ligand-G4s affinity for the **TT-(2PyMeI)$_n$** and **TT-(4PyMeI)$_n$** series revealed better interaction for the *para*-substituted one, highlighting the importance of the positive charge distance from the central scaffold.

Förster resonance energy transfer (FRET) melting assays on the three best performing ligands, namely **TT(4PyMeI)$_3$**, **TT-Gn$_2$** and **TT-Gn$_3$**, supported the remarkable stabilizing ability of the three candidates and provided evidence for better performances of guanyl hydrazone derivatives (rather than the pyridinium ones) probably due to higher flexibility of the peripheral fragments allowing more effective interactions with the grooves/loops of G4s. On the other hand, in order to estimate the ligands' selectivity for G4 over duplex DNA, FRET melting and microscale thermophoresis (MST) experiments were carried out,[160,161] overall suggesting the need for improving their selectivity toward G4 structures by an appropriate molecular design.

Table 2 Compound-induced thermal stabilization of the investigated G4s measured by CD melting experiments. ΔT_m is the difference between the T_m of DNA in the presence (2 molar equiv.) and absence of compounds. T_m values in the absence of compounds are: Tel26 = 44.6 (± 0.1) °C; BCL2 = 61.7 (± 0.1) °C; c-KIT2 = 59.0 (± 0.1) °C and c-MYC = 67.9 (± 0.1) °C. All experiments were performed in duplicate, and the reported values are the average of two measurements

	ΔT_m (°C)			
Compounds	BCL2	c-KIT2	c-MYC	Tel26
TT-(2PyMeI)	−1.6	1.9	0.8	0.9
TT-(2PyMeI)$_2$	0.2	1.0	4.7	2.1
TT-(2PyMeI)$_3$	6.4	4.3	8.1	5.0
TT-(4PyMeI)	3.2	7.0	2.1	6.6
TT-(4PyMeI)$_2$	13.7	15.3	3.8	16.6
TT-(4PyMeI)$_3$	>30	22.0	2.1	22.0
TT-Gn	7.2	11.0	6.2	2.3
TT-Gn$_2$	>30	27.8	10.8	8.4
TT-Gn$_3$	>30	27.7	16.9	11.7

4. Conclusions

The present perspective comprehensively gathers studies on a promising family based on the cyclic triimidazole scaffold, a small, rigid, planar, N-rich system with excellent π–π stacking ability and with moderate electron withdrawing character. Fascinating observations have already been made by inspection of multiemissive properties and coordination potentialities of different members of the family, including the **TT** prototype, and the results are here analytically reported according to different classes.

Excitation dependent short and long-lived photoluminescence of molecular and supramolecular origin resulting in AIE features has been frequently disclosed. **TT**'s multifaceted emissive behaviour, including dual fluorescence and phosphorescence, RTP from aqueous aggregates, mechanochromism and vapochromism, confirms **TT** as a powerful building block for designing high-performance single-component luminescent materials.

Intriguingly, some compounds possess anti-Kasha fluorescence (namely **1-3X** (X = Cl, Br) and **TT-Benzo**) or phosphorescence (**TT-2Py** and **[Ag$_3$(TT)$_4$]$_n$(NO$_3$)$_{3n}$·6nH$_2$O**) or both (**TT-COOH**, **[Zn(TT-COO)$_2$(H$_2$O)$_2$]** and **[Cd(TT-COO)$_2$(H$_2$O)$_2$]**). Some others possess dual fluorescence due to emission from different conformers (**TT-2Py**, **TTPyr** and **TT-Ph-Cz**). Finally, all compounds, except **Iso-A**, display π–π stacking induced phosphorescence. Interpretation of the mechanisms involved in the photophysical behaviour has been achieved through experimental, structural and computational studies. Discrimination between molecular and supramolecular features has been provided by the comparison of photoluminescence in solution and low loaded blended film with respect to crystalline phases. Further proof has been given by mechanochromism associated with supramolecular components and, when possible, comparison among polymorphs.

Preliminary applications of **TTs** in sensing and bio-medicine open avenues for further studies in these fields and exciting results in a plethora of applications are expected by using **TT** as a building block for molecular, macromolecular and supramolecular systems.

Open Access Article. Published on 20 January 2025. Downloaded on 1/21/2026 10:55:07 PM.
This article is licensed under a Creative Commons Attribution-NonCommercial 3.0 Unported Licence.

Table 3 Photophysical properties of **TTs**

Compound		298 K				77 K			Ref.
		Φ (%)	Origin	λ_{em} (nm)	τ_{av}	Origin	λ_{em} (nm)	τ_{av}	
 **TT**	DCM	2	S_1–S_0	400	7.09 ns	S_1–S_0	435	14.31 ns	106
						T^H–S_0	500	0.927 s	
	pwd	18	S_1–S_0	425	9.89 ns	S_1–S_0	430	12.32 ns	
			T^H–S_0	520	0.555 s	T^H–S_0	520	0.963 s	
	cryst	30	S_1–S_0	400	7.67 ns	S_1–S_0	403	8.96 ns	
			T^H–S_0	525	0.970 s	T^H–S_0	510	1.075 s	
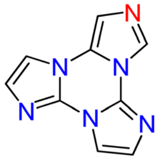 **Iso-A**	cryst	13	S_1–S_0	415	2.98 ns	S_1–S_0	420	14.41 ns	106
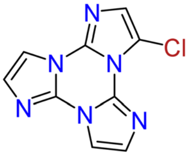 **1Cl**	cryst	24	S_n–S_0	333, 348	0.77 ns	S_n–S_0	333, 349	1.22 ns	68
			S_1–S_0	350	1.02 ns	S_1–S_0	367, 378, 383	4.76 ns	
			T_1–S_0	405, 428	269.74 μs	T_1–S_0	406, 429, 450	1.66 ms	
			T^H–S_0	510	25.99 ms	T^H–S_0	487, 515	778.44 ms	
						T^σ–S_0	558	11.92 ms	
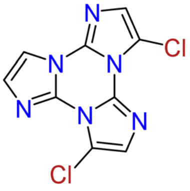 **2Cl**	cryst	12	S_n–S_0	329	n.d.	S_n–S_0	329, 339, 348	n.d.	68
			S_1–S_0	397	1.41 ns	S_1–S_0	362, 380, 401	1.48 ns	
			T_1–S_0	434	1.33 ms	T_1–S_0	436	4.38 ms	
			T^H–S_0	481, 512, 552	49.13 ms	T^H–S_0	483, 515, 554	530.56 ms	
						T^σ–S_0	549	12.68 ms	
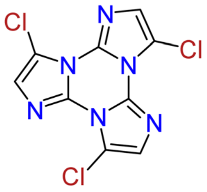 **3Cl**	cryst	9	S_n–S_0	327, 341, 349	n.d.	S_n–S_0	318, 332	n.d.	68
			S_1–S_0	373	0.65 ns	S_1–S_0	358, 380	0.96 ns	
			T_1–S_0	416, 438	13.66 ms	T_1–S_0	416, 439	516.60 ms	
			T^H–S_0	492, 523	142.45 ms	T^H–S_0	490, 521	700.58 ms	
						T^σ–S_0	550	11.22 ms	
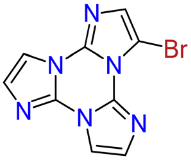 **1Br**	DCM	3	S_n–S_0	328, 342, 358	0.68 ns	T_1–S_0	580	0.276 ms	69,70
	pwd	<0.1	S_n–S_0	326, 345, 365, 382	0.89 ns	S_n–S_0	344, 365, 378	0.86 ns	
			S_1–S_0	426, 530	5.52 ns	S_1–S_0	457, 492, 530	2.54 ns	
						T_1–S_0	573	0.274 ms	
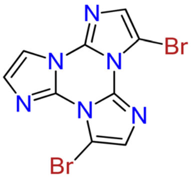 **2Br**	DCM	<0.1	S_n–S_0	380	5.22 ns	T_1–S_0	575	0.288 ms	69,70
	pwd	14	S_n–S_0	395, 419, 443	0.91 ns	S_n–S_0	409, 434, 462	1.96 ns	
			T^{Br}–S_0	470	1.07 ms	T^{Br}–S_0	433, 461, 484	4.05 ms	
			T^H–S_0	553, 600, 646	28.85 ms	T_1–S_0	558	0.302 ms	

View Article Online

Open Access Article. Published on 20 January 2025. Downloaded on 1/21/2026 10:55:07 PM.
This article is licensed under a Creative Commons Attribution-NonCommercial 3.0 Unported Licence.

Table 3 (*continued*)

Compound		298 K				77 K			Ref.
		Φ (%)	Origin	λ_{em} (nm)	τ_{av}	Origin	λ_{em} (nm)	τ_{av}	
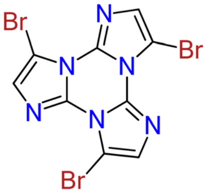 **3Br**	DCM	< 0.1	S_n–S_0	370	10.91 ns	T_1–S_0	585	0.263 ms	69
	pwd	< 0.1	S_n–S_0	394, 418, 444	1.02 ns	S_n–S_0	392, 417, 440	1.51 ns	
			S_1–S_0	415, 437	n.d.	S_1–S_0	414, 440	n.d.	
			T^H–S_0	555, 605, 656	18.42 ms	T^H–S_0	545, 596, 650	n.d.	
						T^{Br}–S_0	490	18.11 ms	
						T_1–S_0	590	0.200 ms	
 **1I**	DCM					T_1–S_0	630	27.27 μs	71
	cryst	< 0.1	S_1–S_0	476	1.37 ns	S_1–S_0	458	2.77 ns	
						T^I–S_0	460, 495, 530	34.85 ms	
			T^H–S_0	517, 563, 612	63.69 ms	T^H–S_0	511, 526, 558, 573, 610	66.47 ms	
			T_1–S_0	630	0.53 μs	T_1–S_0	640	23.66 μs	
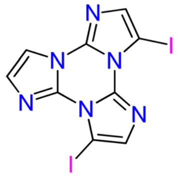 **2I**	cryst	7	S_1–S_0	443	1.23 ns				71
			T^H–S_0	625	9.47 ms				
			T_1–S_0	680	3.47 ms				
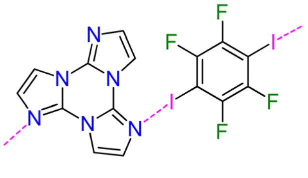 **TT·DITFB**	cryst	5	S_1–S_0	410	2.56 ns	S_1–S_0	440	3.41 ns	71
						T^I–S_0	463, 497, 537	14.65 ms	
			T^H–S_0	496, 528, 566	21.48 ms	T^H–S_0	490, 527, 560	20.01 ms	
						T_1–S_0	720	6.83 μs	
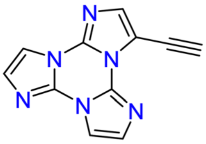 **TT-CCH**	DCM	2	S_1–S_0	363	n.d.				87
	PMMA	3	S_1–S_0	342	0.99 ns				
			S^H–S_0	383	1.46 ns				
			T_1–S_0	439	0.16 ms				
			T^H–S_0	522	6.9 ms				
	cryst	16	S_1–S_0	314, 326, 338	n.d.	S_1–S_0	310, 327, 337	n.d.	
			S^H–S_0	354, 367, 377	1.05 ns	S^H–S_0	354, 364, 383	1.47 ns	
			T_1–S_0	396, 420	0.25 ms	T_1–S_0	395, 419	6.39 ms	
			T^H–S_0	545	4.66 ms	T^H–S_0	489, 523	44.84 ms	
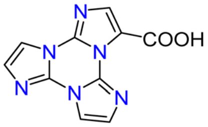 **TT-COOH**	DMSO	3.8	S_2–S_0	327, 343	n.d.				89
			S_1–S_0	404	3.55 ns				
	cryst	26	S_2–S_0	342	2.32 ns	S_2–S_0	326, 341	2,51	
			S_1–S_0	386, 408, 432	2.75 ns	S_1–S_0	385, 408, 435	5,51	
			T_2–S_0	445	3.64 ms	T_2–S_0	457	117 ms	
			T_1–S_0	487	5.58 ms	T_1–S_0	505	526 ms	
			T^H–S_0	549, 590, 642	117 ms	T^H–S_0	549, 590, 642	1.1 s	
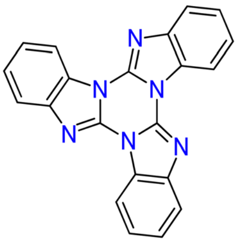 **TT-Benzo**	DCM	17	S_2–S_0	327, 341, 359	3.24 ns	S_2–S_0	338, 352, 373	5.06 ns	70
	pwd	18	S_2–S_0	335, 350, 366	2.61 ns	S_2–S_0	339, 352, 370	1.93 ns	
			S_1–S_0	387, 407, 429	n.d.	S_1–S_0	394, 413, 437	n.d.	
			T^H–S_0	497, 536, 623	0.339 s	T^H–S_0	504, 537, 621	0.573 s	

Open Access Article. Published on 20 January 2025. Downloaded on 1/21/2026 10:55:07 PM.
This article is licensed under a Creative Commons Attribution-NonCommercial 3.0 Unported Licence.

Table 3 (*continued*)

Compound		298 K				77 K			
		Φ (%)	Origin	λ_{em} (nm)	τ_{av}	Origin	λ_{em} (nm)	τ_{av}	Ref.
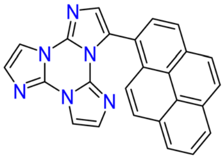 **TT-Pyr**	DMSO	92	S_1–S_0	420	2.76 ns				79,80
	cryst **TT-Pyr(Et)**	53	S_1–S_0	493	2.97 ns	S_1–S_0	463, 493, 520	4.17 ns	
			T^H–S_0	555	4.95 ms	T^H–S_0	553, 596	5.37 ms	
	TT-Pyr(RT)	20	S_1–S_0	490	1.85 ns	S_1–S_0	463, 492, 520	2.66 ns	
			T^H–S_0	550	4.62 ms	T^H–S_0	556, 599	5.61 ms	
	TT-Pyr(HT)	21	S'_1	422, 443	0.62 ns	S'_1	413, 450	1.56 ns	
			S_1–S_0	483	1.99 ns	S_1–S_0	478	2.91 ns	
			T^H–S_0	524, 563	23.4 ms	T^H–S_0	553, 590	26.2 ms	
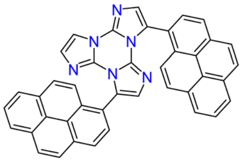 **TT-Pyr$_2$**	DMSO	78	S_1–S_0	419	9.22 ns				79
	pwd	40.2	S_1–S_0	490	4.64 ns				
			T^H–S_0	528	20.54 ms				
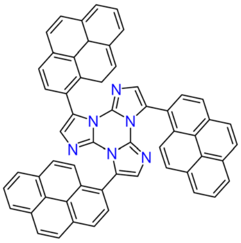 **TT-Pyr$_3$**	DMSO	74.4	S_1–S_0	422	11.16 ns				79
	pwd	36.9	S_1–S_0	476	5.12 ns				
			T^H–S_0	522	40.62 ms				
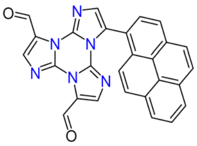 **(CHO)$_2$-TTPyr**	DMSO	3	S_1–S_0	565	2.76 ns				88
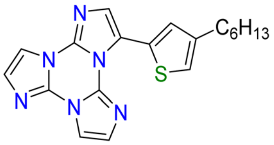 **TT-HThio**	DCM	11	S_1–S_0	370	0.81 ns	S_1–S_0	365	1.71 ns	86
	PMMA	15	S_1–S_0	365	0.72 ns				
	cryst	26	S_1–S_0	376	1.15 ns	S_1–S_0	368	1.48 ns	
			T_1–S_0	425, 451	5.91 ms	T_1–S_0	420, 448	10.61 ms	
			T^H–S_0	497, 530, 578	50.22 ms	T^H–S_0	494, 553, 577	132.01 ms	
	Ground cryst	18	S_1–S_0	376	1.11 ns	S_1–S_0	375	1.91 ns	
			T_1–S_0	428, 441	5.20 ms	T_1–S_0	423, 443	9.56 ms	
			T^H–S_0	500	29.81 ms	T^H–S_0	492, 513	60.84 ms	
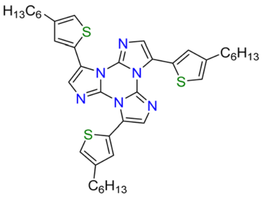 **TT-HThio$_3$**	DCM	5	S_1–S_0	380	1.17 ns	S_1–S_0	370	1.42 ns	86
	PMMA	17	S_1–S_0	372	0.90 ns	S_1–S_0			
	pwd	22	S_1–S_0	382, 400	0.42 ns	S_1–S_0	364, 381	1.23 ns	
			T_1–S_0	428, 453	15.10 ms	T_1–S_0	423, 447	153.42 ms	
			T^H–S_0	514, 550	41.51 ms	T^H–S_0	478, 512, 544	327.16 ms	
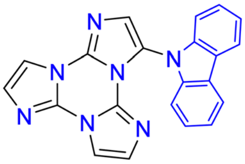 **TT-(N)-Cz**	DCM	27	S_1–S_0	337, 345	3.47 ns	S_1–S_0	339	5.69 ns	84
						T_1–S_0	411, 439, 466	2.75 s	
	PMMA	28	S_1–S_0	333, 345	9.58 ns	S_1–S_0	345	10.25 ns	
			T_1–S_0	412, 440, 462	319.3 ms	T_1–S_0	411, 439, 466[b]	82.87 ms	
	cryst **TT-(N)-CzT**	13	S_1–S_0	350	2.37 ns	S_1–S_0	329, 343, 352	4.30 ns	
			S^H–S_0	379, 390, 398	28.02 ns	S^H–S_0	377, 385, 394	52.13 ns	
			T_1–S_0	442, 464	23.36 ms	T_1–S_0	440, 465	82.87 ms	
			T^H–S_0	509	247.78 ms	T^H–S_0	495, 516	1.14 s	
	TT-(N)-CzM	16	S_1–S_0	357, 367	3.66 ns	S_1–S_0	344, 358	6.34 ns	

Open Access Article. Published on 20 January 2025. Downloaded on 1/21/2026 10:55:07 PM. This article is licensed under a Creative Commons Attribution-NonCommercial 3.0 Unported Licence.

Table 3 (*continued*)

				298 K			77 K			
Compound			Φ (%)	Origin	λ_{em} (nm)	τ_{av}	Origin	λ_{em} (nm)	τ_{av}	Ref.
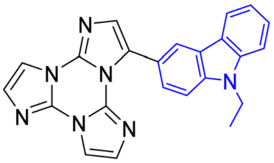 **TT-(C)-Cz**				S^{H}–S_0	386, 391, 402	15.39 ns	S^{H}–S_0	381, 394, 402	27.31 ns	84
				T_1–S_0	437	20.04 ms	T_1–S_0	436	71.35 ms	
				T^{H}–S_0	517	0.17 s	T^{H}–S_0	519	0.13 s	
	DCM		20	S_1–S_0	380	5.55 ns	S_1–S_0	365, 381	5.80 ns	
							T^{H}–S_0	500	0.88 s	
	PMMA		33	S_1–S_0	377	9.98 ns	S_1–S_0	361, 379	10.49 ns	
				T_1–S_0	417	46.51 ms	T_1–S_0	412, 442	1.65 s	
				T^{H}–S_0	515	134.6 ms	T^{H}–S_0	500	0.24 s	
	cryst		28	S_1–S_0	402, 420	6.74 ns	S_1–S_0	380, 400, 422	8.45 ns	
				T_1–S_0	460, 486	57.80 ms	T_1–S_0	471	0.12 s	
				T^{H}–S_0	531, 580	0.12 s	T^{H}–S_0	500, 540	1.17 s	
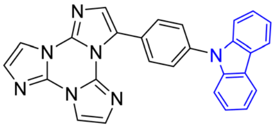 **TT-Ph-Cz**	DCM		63	S_1–S_0	350, 370	2.86 ns	S_1–S_0	353	5.60 ns	81
							T^{H}–S_0	512	935 ms	
	PMMA		60	S_1–S_0	347, 360	7.70 ns	S_1–S_0	350 (90 K)	8.79 ns[b]	
				T^{H}–S_0	490	246.8 ms	T^{H}–S_0	508	601.0 ms	
	cryst	**TT-Ph-CzM**	43	S_1–S_0	375, 408	2.16 ns	S_1–S_0	373, 388	3.45 ns	
				T_1–S_0	425	20.72 ms				
				T^{H}–S_0	540	60.94 ms	T^{H}–S_0	523	684.47 ms	
		TT-Ph-CzT	22	S_1–S_0	374, 394	3.41 ns				
				T_1–S_0	432	3.03 ms				
				T^{H}–S_0	510	10.61 ms				
		TT-Ph-CzO	23	S_1–S_0	373	3.49 ns				
				T_1–S_0	416	15.04 ms				
				T^{H}–S_0	550	62.16 ms				
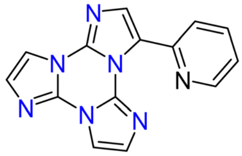 **TT-2Py**	DCM		17	S_1–S_0	351	0.62 ns	S_1–S_0	325, 345	2.32 ns	85
				T_n–S_0		10.2 ms	T_n–S_0	375	13.16 ms	
				T_1–S_0	408	11.01 ms	T_1–S_0	393	—	
	PMMA			S_1–S_0	350	1.18 ns				
				T_1–S_0	394	13.73 ms				
				S'_1–S'_0	440	3.47 ns				
				$T^{H\prime}$–S_0	530	15.70 ms				
	cryst	**TT-2Py-A**	52	T_n–S_0	370	698 ms				
				T_1–S_0	418	0.29 ms				
				S'_1–S'_0	450	—				
				$T^{H\prime}$–S_0	510, 570, 608	2.09 ms				
		TT-2Py-H		T_n–S_0	374	20.38 ms				
				T_1–S_0	408	0.47 ms				
				S'_1–S'_0	450	1.91 ns				
				$T^{H\prime}$–S_0	500	18.25 ms				
					528, 562, 610	5.98 ms				
		TT-2Py-X		T_n–S_0	362	91.83 ms				
				T_1–S_0	402	1.31 ms				
				S'_1–S'_0	466	4.13 ns				
				$T^{H\prime}$–S_0	524	9.38 ms				
				T^{H}–S_0	636, 695, 767	111.1 ms				
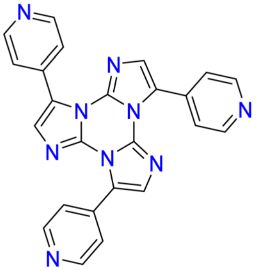 **TT-4py$_3$**	pwd		—	S_1–S_0	365	1.25 ns				132
				T_1–S_0	458	6.31 ms				
				T^{H}–S_0	549	66.41 ms				
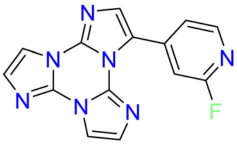 **TT-4PyF**	ACN		50	S_1–S_0	358	4.26 ns	S_1–S_0	344	4.04 ns	82
							T_1–S_0	454	1.63 s	
	PMMA			S_1–S_0	348	1.89 ns				
				T_1–S_0	415, 436	3.09 ms				
	cryst		25	S_1–S_0	373	4.77 ns	S_1–S_0	385	16.42 ns	
				T_1–S_0	403, 424, 446	11.64 ms	T_1–S_0	401, 425, 457	12.95 ms	
				T^{H}–S_0	546, 592	419.08 ms	T^{H}–S_0	549	1.93 s	

Open Access Article. Published on 20 January 2025. Downloaded on 1/21/2026 10:55:07 PM.
This article is licensed under a Creative Commons Attribution-NonCommercial 3.0 Unported Licence.

Table 3 (*continued*)

		298 K				77 K			
Compound		Φ (%)	Origin	λ_{em} (nm)	τ_{av}	Origin	λ_{em} (nm)	τ_{av}	Ref.
Hybrid inorganic/organic derivatives									
[Zn$_3$(CH$_3$COO)$_6$(H$_2$O)$_2$](TT)$_2$	cryst	7	S_1–S_0	375, 395, 418	6.75 ns	S_1–S_0	416	8.45 ns	123
			T^H–S_0	555	0.650 s	T^H–S_0	554	1.303 s	
[Cd(H$_2$O)$_6$](ClO$_4$)$_2$(TT)$_2$	cryst	10	S_1–S_0	421	5.17 ns	S_1–S_0	440	5.50 ns	123
			T^H–S_0	549	0.110 s	T^H–S_0	550	0.585 s	
[Cd(H$_2$O)$_6$](BF$_4$)$_2$(TT)$_2$	cryst	16	S_1–S_0	383	17.16 ns	S_1–S_0	390	18.63 ns	123
			T^H–S_0	441, 469	0.293 s	T^H–S_0	441, 471	0.753 ms	
[Zn(H$_2$O)$_6$](BF$_4$)$_2$(TT)$_2$	cryst	9	S_1–S_0	370	3.52 ns	S_1–S_0	371	5.66 ns	123
			T^H–S_0	394, 422	0.542 s	T^H–S_0	397, 422	1.29 s	
[Zn(TT)(NO$_3$)(H$_2$O)$_3$](NO$_3$)	cryst	1	S_1–S_0	439	4.36 ns	S_1–S_0	430	5.93 ns	124
			T^H–S_0	550	67.70 ms	T^H–S_0	498	534.63 ms	
[Cd(TT)$_2$(NO$_3$)$_2$(H$_2$O)$_2$]	cryst		S_1–S_0	430	0.61 ns	S_1–S_0	430	2.15 ns	124
			T^H–S_0	505	32.69 ms	T^H–S_0	500	240.96 ms	
[Ag(TT)I]$_n$	cryst	19	S_1–S_0	385, 400	2.15 ns	S_1–S_0	386, 395	2.31 ns	126
			T_1–S_0	411, 445	$<$50 µs	T_1–S_0	425, 446	421.03 µs	
			T^I–S_0	446, 476, 509	2.84 ms	T^I–S_0	440, 470, 506, 541	5.67 ms	
			T_H–S_0	494, 530, 575, 620, 680	39.76 ms	T_H–S_0	490, 528, 576, 631, 701	44.51 ms	
[Cu(TT)I]*n*	cryst	18	T_1–S_0	568	32 µs	T_1–S_0	568	47.14 µs	125, 126
			T^I–S_0	431, 460, 487	—	T^I–S_0	430, 460, 494, 538	41.85 µs	
			T_H–S_0	536, 582, 623	302.12 µs	T_H–S_0	529, 580, 627	1.03 s	
[Ag(TT)Cl]$_n$	cryst		S_1–S_0	448	4.45 ns				126
			T_1–S_0	520	—				
			T_H–S_0	526, 565, 615	47.7 ms				
[Cu(TT)Cl]$_n$	cryst	4	T_1–S_0	515	6.24 µs				125, 126
			T_H–S_0	560	3.56 ms				
[Ag$_3$(TT)$_4$]$_n$(NO$_3$)$_{3n}$·6*n*H$_2$O	cryst	7.5	S_1–S_0	404	1.49 ns	S_1–S_0	391	1.76 ns	126
			T_n–S_0	454	3.41 ms	T_n–S_0	471	32.69 ms	
			T_1–S_0	556	1.04 ms	T_1–S_0	565	33.36 ms	
[Zn(TT-COO)$_2$(H$_2$O)$_2$]	cryst	9	S_2–S_0	338	0.88 ns				89
			S_1–S_0	382, 405, 430	1.94 ns				
			T_2–S_0	452	1.42 ms				
			T_1–S_0	490	4.3 ms				
			T^H–S_0	566	478 ms				
[Cd(TT-COO)$_2$(H$_2$O)$_2$]	cryst	1.4	S_2–S_0	352	0.77 ns				89
			S_1–S_0	382, 405, 430	1.59 ns				
			T_2–S_0	452	2.04 ms				
			T_1–S_0	523	10.4 ms				
			T^H–S_0	577	116 ms				
[ReCl(CO)$_3$(TT-2Py)]	Tol	0.4	T_1–S_0	583	483 ns				129
	pwd	12	T_1–S_0	532	100 ms				
[Re$_3$Cl$_3$(CO)$_9$(TT-2Py)]$_2$	Tol	0.01	T_1–S_0	597	500 ns				129
	pwd	2.5	T_1–S_0	563	40 ms				
[Cu$_2$I$_2$(TT-2Py)]$_n$	cryst	7.3	T_1–S_0	588	1.33 ms	T_1–S_0	580	17.89 ms	130
[Cu$_2$I$_2$(TT-2Py)]$_2$	cryst	44	T^I–S_0	515	9.35 µs	T^I–S_0	513	27.93 µs	
			T^H–S_0	598	19.07 µs	T^H–S_0	596, 645	1.73 ms	
[Ag{(TT-4Py$_3$}(SO$_3$CF$_3$)]$_n$·$\frac{1}{2}$nCH$_2$Cl$_2$	cryst	1	S_1–S_0	390	1.66 ns	S_1–S_0	395	1.96 ns	132
			T_1–S_0	460	0.836 ms	T_1–S_0	450	1.35 ms	
			T^H–S_0	530	4.912 ms	T^H–S_0	510, 548, 592, 655	262 ms	
[Cd{TT-4Py$_3$}(NO$_3$)$_2$(EtOH)]$_n$	cryst	15	S_1–S_0	405	2.54 ns	S_1–S_0	346, 365, 381, 403, 421	2.69 ns	132
			T_1–S_0	455	12.62 ms	T_1–S_0	450	73.88 ms	
			T^H–S_0	550	74.63 ms	T^H–S_0	498, 536	1.86 s	
[(Cu$_2$I$_2$)$_3${TT-4Py$_3$}$_4$]$_n$·*xn*(H$_2$O,EtOH)	cryst	≈1	T^H–S_0	650	6.36 ms	T^H–S_0	606	34.47 ms	132
(TT-4PyHTT-4Py)$_2$[Eu(NO$_3$)$_5$(H$_2$O)]·(CH$_3$CN)$_2$	cryst		S_1–S_0	450					139
			$^5D_0$–$^7F_2$	618					
[Eu(NO$_3$)$_3$(H$_2$O)$_2$(TT-4Py$_3$)]	cryst		$^5D_0$–$^7F_2$	618	283 µs				139

T^{σ}: triplet of (π,σ^*) symmetry, T^{Br}: triplet located on the Br halogen bond; T_n: high energy triplet; S_n: high energy singlet; T^I: triplet associated with the extrinsic I effect, S'_0,S'_1: S_0, S_1 from a second conformer; S^H: singlet from π–π aggregates; T^H: triplet from π–π aggregates; $T^{H'}$: triplet from a π–π dimer.

Open Access Article. Published on 20 January 2025. Downloaded on 1/21/2026 10:55:07 PM.
This article is licensed under a Creative Commons Attribution-NonCommercial 3.0 Unported Licence.

A close control of the excited-state energy, which is essential for the development of triplet exciton-harvesting organic emitters, such as those with TADF and RTP, is far from being reached and needs further investigations through appropriate functionalization of the **TT** core with donor groups.[57,58] When compared with other fused nitrogen-rich heterocycles, **TT** enables the preparation of asymmetric scaffolds: brominated derivatives have been revealed as convenient starting materials in C–C and C–N cross-coupling reactions, and therefore, donor–acceptor groups can be introduced on the core by properly reacting **1–2Br**.

The presence of three exo-oriented nitrogen atoms on the **TT** scaffold, its relatively simple functionalization with coordinating groups and the possibility to prepare mono-, di- and tri-substituted systems make **TTs** particularly attracting in view of their further exploitation in coordination chemistry and isolation of porous metal–organic frameworks (MOF). In addition, tri-substituted **TTs** with C_3 symmetry represent appealing building blocks for the production of covalent organic frameworks (COF), as reported for other π-extended conjugated multiazine or H-bonded organic frameworks (HOF), by fine tuning pendant groups around the central core. Moreover, because of their octupolar character, appropriately functionalized tri-substituted **TTs** represent suitable candidates for NLO applications and as chromophores for multiphoton absorption.

Due to their planar and prochiral nature, **TTs** can be exploited for the development of self-organized homochiral two-dimensional nanostructures on different surfaces to be used, for example, in the preparation of graphene-like structures.

A further challenge regarding this family is the application of **iso-A**, the **TT** isomer, in the preparation and characterization of molecular and supramolecular materials analogous to those of **TT**. Moreover, **iso-A** utilization in the preparation of carbene compounds (through salification of the asymmetric nitrogen and subsequent reaction with metals) as preliminarily reported in the literature[64] deserves further investigation.

Data availability

No primary research results, software or code have been included and no new data were generated or analysed as part of this perspective.

Conflicts of interest

There are no conflicts to declare.

Acknowledgements

The authors are grateful to Chiara Botta, Lucia Carlucci, Clelia Giannini and Daniele Marinotto for their contribution to most of the work cited in this perspective.

References

1 A. A. Bekhit and A. M. Baraka, *Eur. J. Med. Chem.*, 2005, **40**, 1405–1413.
2 M. A. Gouda, M. A. Berghot, G. E. Abd El-Ghani and A. E.-G. M. Khalil, *J. Heterocycl. Chem.*, 2016, **53**, 1241–1250.
3 E. M. Morsy, E. R. Kotb, H. A. Soliman, H. H. Sayyed and N. A. Abdelwahed, *Acta Pol. Pharm.*, 2015, **72**, 465–474.
4 A. Kumar, S. Rana, G. Sharma, P. Dhiman, M. I. Shekh and F. J. Stadler, *J. Environ. Chem. Eng.*, 2023, **11**, 110770.
5 X. Wei, N. Li, Y. Wang, Z. Xie, H. Huang, G. Yang, T. Li, X. Qin, S. Li, H. Yang, J. Zhu, F. You, C. Wu and Y. Liu, *Appl. Mater. Today*, 2021, **23**, 100995.
6 Q. Zhang, J. Zhou, H. Zhang, C. Qi, Q. Zhou, R. Guo, H. Yang, T. Xing, M. Wang, M. Wu and W. Wu, *Adv. Funct. Mater.*, 2024, **34**, 2401579.
7 Z. An, C. Zheng, Y. Tao, R. Chen, H. Shi, T. Chen, Z. Wang, H. Li, R. Deng, X. Liu and W. Huang, *Nat. Mater.*, 2015, **14**, 685–690.
8 S. Cai, H. Shi, J. Li, L. Gu, Y. Ni, Z. Cheng, S. Wang, W.-W. Xiong, L. Li, Z. An and W. Huang, *Adv. Mater.*, 2017, **29**, 1701244.
9 L. Gu, H. Shi, C. Miao, Q. Wu, Z. Cheng, S. Cai, M. Gu, C. Ma, W. Yao, Y. Gao, Z. An and W. Huang, *J. Mater. Chem. C*, 2018, **6**, 226–233.
10 Y. Liu, G. Zhan, P. Fang, Z. Liu, Z. Bian and C. Huang, *J. Mater. Chem. C*, 2017, **5**, 12547–12552.
11 G.-P. Yong, Y.-M. Zhang, W.-L. She and Y.-Z. Li, *J. Mater. Chem.*, 2011, **21**, 18520.
12 W. Akbar, S. Ehsan, S. A. Siddique, M. Sarfraz, F. Shaheen, A. Shafqat, Shahnaz, M. B. A. Siddique, A. Saeed, R. Al-Salahi and Y. El Bakri, *ACS Omega*, 2024, **9**, 34428–34444.
13 S. H. Lee, S. Kim, M. H. Yun, Y. S. Lee, S. N. Cho, T. Oh and P. Kim, *Bioorg. Med. Chem. Lett.*, 2011, **21**, 1515–1518.
14 X. Lu, X. Liu, B. Wan, S. G. Franzblau, L. Chen, C. Zhou and Q. You, *Eur. J. Med. Chem.*, 2012, **49**, 164–171.
15 Y. Ozkay, I. Isikdag, Z. Incesu and G. Akalin, *Eur. J. Med. Chem.*, 2010, **45**, 3320–3328.
16 B. Rathod, S. Pawar, S. Puri, A. Diwan and K. Kumar, *ChemistrySelect*, 2024, **9**, e202303655.
17 M. Tapera, E. Doğan, K. Şahin, G. A. Gözkamane, H. Kekeçmuhammed, S. Sandal, A. C. Gurkan, R. E. Bora, A. Anber, S. Durdagi, Y. Zorlu and E. Sarıpınar, *J. Mol. Struct.*, 2024, 1318.
18 Y. A. Belousov, A. A. Drozdov, I. V. Taydakov, F. Marchetti, R. Pettinari and C. Pettinari, *Coord. Chem. Rev.*, 2021, **445**, 214084.
19 X.-Q. Liang, H.-P. Xiao, B.-L. Liu, Y.-Z. Li, J.-L. Zuo and X.-Z. You, *Polyhedron*, 2008, **27**, 2494–2500.
20 X.-Q. Liang, X.-H. Zhou, C. Chen, H.-P. Xiao, Y.-Z. Li, J.-L. Zuo and X.-Z. You, *Cryst. Growth Des.*, 2009, **9**, 1041–1053.
21 G. Yuan, Z. Chao, D.-J. Xu, K.-Z. Shao, X.-M. Li, X.-R. Hao and Z.-M. Su, *Polyhedron*, 2020, **180**, 114430.
22 A. Barakat, A. El-Faham, M. Haukka, A. M. Al-Majid and S. M. Soliman, *Appl. Organomet. Chem.*, 2021, **35**, e6317.

Open Access Article. Published on 20 January 2025. Downloaded on 1/21/2026 10:55:07 PM. This article is licensed under a Creative Commons Attribution-NonCommercial 3.0 Unported Licence.

23 K. Biradha and M. Fujita, *Angew. Chem., Int. Ed.*, 2002, **41**, 3392–3395.

24 B. Therrien, *J. Organomet. Chem.*, 2011, **696**, 637–651.

25 M.-H. Yu, X.-T. Liu, B. Space, Z. Chang and X.-H. Bu, *Coord. Chem. Rev.*, 2021, **427**, 213518.

26 C. Krishnaraj, H. S. Jena, K. Leus and P. Van Der Voort, *Green Chem.*, 2020, **22**, 1038–1071.

27 P. Puthiaraj, Y.-R. Lee, S. Zhang and W.-S. Ahn, *J. Mater. Chem. A*, 2016, **4**, 16288–16311.

28 P. Xiong, S. Zhang, R. Wang, L. Zhang, Q. Ma, X. Ren, Y. Gao, Z. Wang, Z. Guo and C. Zhang, *Energy Environ. Sci.*, 2023, **16**, 3181–3213.

29 K. L. Kirk, W. Nagai and L. A. Cohen, *J. Am. Chem. Soc.*, 1973, **95**, 8389–8392.

30 D. M. Schubert, D. T. Natan, D. C. Wilson and K. I. Hardcastle, *Cryst. Growth Des.*, 2011, **11**, 843–850.

31 J. L. Segura, R. Juárez, M. Ramos and C. Seoane, *Chem. Soc. Rev.*, 2015, **44**, 6850–6885.

32 K. Bergmann and Z. M. Hudson, *Faraday Discuss.*, 2024, **250**, 181–191.

33 O. Buyukcakir, R. Yuksel, Y. Jiang, S. H. Lee, W. K. Seong, X. Chen and R. S. Ruoff, *Angew. Chem., Int. Ed.*, 2019, **58**, 872–876.

34 H. Chen, X. Suo, Z. Yang and S. Dai, *Adv. Mater.*, 2022, **34**, 2107947.

35 J. Li, L. Tao, Y. Wang, Y. Yao and Q. Guo, *Front. Chem.*, 2021, **9**, 717569.

36 J. Liu, D. Yang, Y. Zhou, G. Zhang, G. Xing, Y. Liu, Y. Ma, O. Terasaki, S. Yang and L. Chen, *Angew. Chem., Int. Ed.*, 2021, **60**, 14473–14479.

37 S. Vijayakumar, A. P. Mohanachandran, R. B. Rakhi, S. Shankar, R. S. Pillai and A. Ajayaghosh, *Small*, 2024, **20**, 2405701.

38 X.-Y. Yan, M.-D. Lin, S.-T. Zheng, T.-G. Zhan, X. Zhang, K.-D. Zhang and X. Zhao, *Tetrahedron Lett.*, 2018, **59**, 592–604.

39 K. A. Hofmann and O. Ehrhart, *Chem. Ber.*, 1912, **45**, 2731–2740.

40 R. Huisgen, H. J. Sturm and M. Seidel, *Chem. Ber.*, 1961, **94**, 1555–1562.

41 R. Cristiano, J. Eccher, I. H. Bechtold, C. N. Tironi, A. A. Vieira, F. Molin and H. Gallardo, *Langmuir*, 2012, **28**, 11590–11598.

42 R. Cristiano, H. Gallardo, A. J. Bortoluzzi, I. H. Bechtold, C. E. M. Campos and R. L. Longo, *Chem. Commun.*, 2008, 5134–5136, DOI: **10.1039/B810680K**.

43 A. G. Dal-Bó, G. G. L. Cisneros, R. Cercena, J. Mendes, L. M. da Silveira, E. Zapp, K. G. Domiciano, R. da Costa Duarte, F. S. Rodembusch and T. E. A. Frizon, *Dyes Pigm.*, 2016, **135**, 49–56.

44 M. D. S. Kutz, L. A. Suassuna e Bega, C. Francener, G. Farias, F. A. de Campos, H. Bock, I. H. Bechtold, F. Molin and E. Westphal, *J. Mol. Struct.*, 2025, **1321**, 139996.

45 M. Sperner, N. Tober and H. Detert, *Eur. J. Org. Chem.*, 2019, 4688–4693.

46 V. A. Tartakovsky, A. E. Frumkin, A. M. Churakov and Y. A. Strelenko, *Russ. Chem. Bull.*, 2005, **54**, 719–725.

47 S. Glang, T. Rieth, D. Borchmann, I. Fortunati, R. Signorini and H. Detert, *Eur. J. Org. Chem.*, 2014, 3116–3126.

48 H. Zhao, Y. Wang, Z. Liu and B. Dai, *RSC Adv.*, 2014, **4**, 13161–13166.

49 X. Chen, S. Wang, H. L. Lee, J. Y. Lee, X. Liao, L. Li, W. Zhu and Y. Wang, *Adv. Opt. Mater.*, 2021, **9**, 2101518.

50 Z. Fang, S. Wang, J. Liao, X. Chen, Y. Zhu, W. Zhu and Y. Wang, *J. Mater. Chem. C*, 2022, **10**, 4837–4844.

51 R. Hojo, D. M. Mayder and Z. M. Hudson, *J. Mater. Chem. C*, 2021, **9**, 14342–14350.

52 F. Hundemer, E. Crovini, Y. Wada, H. Kaji, S. Bräse and E. Zysman-Colman, *Mater. Adv.*, 2020, **1**, 2862–2871.

53 S. K. Pathak, Y. Xiang, M. Huang, T. Huang, X. Cao, H. Liu, G. Xie and C. Yang, *RSC Adv.*, 2020, **10**, 15523–15529.

54 S. Wang, X. Wang, K. H. Lee, S. Liu, J. Y. Lee, W. Zhu and Y. Wang, *Dyes Pigm.*, 2020, **182**, 108589.

55 Y. Yin, S. Zeng, C. Xiao, P. Fan, D. J. Shin, K. J. Kim, H. Nam, Q. Ma, H. Ma, W. Zhu, T. Kim, J. Y. Lee and Y. Wang, *Mater. Horiz.*, 2024, **11**, 1741–1751.

56 S. Zeng, C. Xiao, J. Zhou, Q. Dong, Q. Li, J. Lim, H. Ma, J. Y. Lee, W. Zhu and Y. Wang, *Adv. Funct. Mater.*, 2022, **32**, 2113183.

57 H. Marchi Luciano, G. Farias, C. M. Salla, L. G. Franca, S. Kuila, A. P. Monkman, F. Durola, I. H. Bechtold, H. Bock and H. Gallardo, *Chem. – Eur. J.*, 2023, **29**, e202203800.

58 M. Ferreira, N. O. Decarli, A. Nyga, K. Erfurt, J. Lingagouder, L. E. de Sousa, L. de Thieulloy, P. de Silva and P. Data, *J. Mater. Chem. C*, 2024, **12**, 13651–13664.

59 E. C. Coad, P. G. Apen and P. G. Rasmussen, *J. Am. Chem. Soc.*, 1994, **116**, 391–392.

60 E. C. Coad, J. Kampf and P. G. Rasmussen, *J. Org. Chem.*, 1996, **61**, 6666–6672.

61 J. Heredia-Moya and K. L. Kirk, *J. Fluorine Chem.*, 2007, **128**, 674–678.

62 Y. Takeuchi, K. L. Kirk and L. A. Cohen, *J. Org. Chem.*, 1979, **44**, 4243–4246.

63 I. Sadahiro, F. Yoshiaki, S. Shizen and M. Kohji, *Bull. Chem. Soc. Jpn.*, 1975, **48**, 956–959.

64 D. M. Buck and D. Kunz, *Organometallics*, 2015, **34**, 5335–5340.

65 R. Bhattacharya, S. Ray, J. Ray and A. Ghosh, *Cent. Eur. J. Chem.*, 2003, **1**, 427.

66 O. Ghashghaei, S. Caputo, M. Sintes, M. Revés, N. Kielland, C. Estarellas, F. J. Luque, A. Aviñó, R. Eritja, A. Serna-Gallego, J. A. Marrugal-Lorenzo, J. Pachón, J. Sánchez-Céspedes, R. Treadwell, F. de Moliner, M. Vendrell and R. Lavilla, *Chem. – Eur. J.*, 2018, **24**, 14513–14521.

67 O. Ghashghaei, P. N. Rodríguez and R. Lavilla, *Synlett*, 2022, 822–835.

68 C. Giannini, A. Forni, D. Malpicci, E. Lucenti, D. Marinotto, A. Previtali, L. Carlucci and E. Cariati, *Eur. J. Org. Chem.*, 2021, 2041–2049.

69 E. Lucenti, A. Forni, C. Botta, L. Carlucci, A. Colombo, C. Giannini, D. Marinotto, A. Previtali, S. Righetto and E. Cariati, *ChemPhotoChem*, 2018, **2**, 801–805.

70 E. Lucenti, A. Forni, C. Botta, L. Carlucci, C. Giannini, D. Marinotto, A. Pavanello, A. Previtali, S. Righetto and E. Cariati, *Angew. Chem., Int. Ed.*, 2017, **56**, 16302–16307.

Open Access Article. Published on 20 January 2025. Downloaded on 1/21/2026 10:55:07 PM.
This article is licensed under a Creative Commons Attribution-NonCommercial 3.0 Unported Licence.

71 E. Lucenti, A. Forni, C. Botta, C. Giannini, D. Malpicci, D. Marinotto, A. Previtali, S. Righetto and E. Cariati, *Chem. – Eur. J.*, 2019, **25**, 2452–2456.

72 S. Di Micco, C. Giannini, A. Previtali, E. Lucenti and G. Bifulco, *Magn. Reson. Chem.*, 2019, **57**, 82–92.

73 M. Beinhoff, W. Weigel, M. Jurczok, W. Rettig, C. Modrakowski, I. Brüdgam, H. Hartl and A. D. Schlüter, *Eur. J. Org. Chem.*, 2001, 3819–3829.

74 A. Pal, R. Ghosh, N. N. Adarsh and A. Sarkar, *Tetrahedron*, 2010, **66**, 5451–5458.

75 M. Mao, M.-G. Ren and Q.-H. Song, *Chem. – Eur. J.*, 2012, **18**, 15512–15522.

76 S. Telitel, F. Dumur, T. Faury, B. Graff, M.-A. Tehfe, D. Gigmes, J.-P. Fouassier and J. Lalevée, *Beilstein J. Org. Chem.*, 2013, **9**, 877–890.

77 M. Drev, U. Grošelj, B. Ledinek, F. Perdih, J. Svete, B. Štefane and F. Požgan, *Org. Lett.*, 2018, **20**, 5268–5273.

78 D. Malpicci, S. Andolina, S. Di Ciolo, E. Lucenti, E. Cariati, S. Marzano, B. Pagano, J. Amato, A. Randazzo and C. Giannini, *Eur. J. Org. Chem.*, 2022, e202200718.

79 D. Malpicci, C. Giannini, E. Lucenti, A. Forni, D. Marinotto and E. Cariati, *Photochem*, 2021, **1**, 477–487.

80 A. Previtali, W. He, A. Forni, D. Malpicci, E. Lucenti, D. Marinotto, L. Carlucci, P. Mercandelli, M. A. Ortenzi, G. Terraneo, C. Botta, R. T. K. Kwok, J. W. Y. Lam, B. Z. Tang and E. Cariati, *Chem. – Eur. J.*, 2021, **27**, 16690–16700.

81 D. Malpicci, A. Forni, C. Botta, C. Giannini, E. Lucenti, D. Marinotto, D. Maver, L. Carlucci and E. Cariati, *Chem. – Eur. J.*, 2023, **29**, e202300930.

82 A. Previtali, E. Lucenti, A. Forni, L. Mauri, C. Botta, C. Giannini, D. Malpicci, D. Marinotto, S. Righetto and E. Cariati, *Molecules*, 2019, **24**, 2552.

83 D. Malpicci, S. R. Araneo, S. Arnaboldi, E. Cariati, A. Forni, S. Grecchi, E. Lucenti, D. Marinotto, D. Maver and P. R. Mussini, *Electrochim. Acta*, 2023, **469**, 143117.

84 D. Malpicci, A. Forni, C. Botta, C. Giannini, E. Lucenti, D. Marinotto, D. Maver, L. Carlucci and E. Cariati, *Dyes Pigm.*, 2023, **215**, 111274.

85 E. Lucenti, A. Forni, A. Previtali, D. Marinotto, D. Malpicci, S. Righetto, C. Giannini, T. Virgili, P. Kabacinski, L. Ganzer, U. Giovanella, C. Botta and E. Cariati, *Chem. Sci.*, 2020, **11**, 7599–7608.

86 D. Malpicci, A. Forni, E. Cariati, R. Inoguchi, D. Marinotto, D. Maver, F. Turco and E. Lucenti, *Molecules*, 2023, **28**, 140.

87 D. Malpicci, D. Maver, E. Rosadoni, A. Colombo, E. Lucenti, D. Marinotto, C. Botta, F. Bellina, E. Cariati and A. Forni, *Molecules*, 2024, **29**, 1967.

88 M. Formenti, D. Blasi, E. Cariati, L. Carlucci, A. Forni, C. Giannini, M. Guidotti, S. Econdi, D. Malpicci, D. Marinotto and E. Lucenti, *Dyes Pigm.*, 2022, **206**, 110637.

89 D. Malpicci, A. Forni, E. Lucenti, D. Marinotto, D. Maver, V. Lozovan, V. C. Kravtsov, A. Siminel, M. S. Fonari and E. Cariati, *Eur. J. Inorg. Chem.*, 2024, e202400338.

90 E. Rosadoni, L. Ballerini, A. Del Vecchio and F. Bellina, *Asian J. Org. Chem.*, 2024, **13**, e202400082.

91 M. Magni, E. Lucenti, A. Previtali, P. R. Mussini and E. Cariati, *Electrochim. Acta*, 2019, **317**, 272–280.

92 Q. Dang, Y. Jiang, J. Wang, J. Wang, Q. Zhang, M. Zhang, S. Luo, Y. Xie, K. Pu, Q. Li and Z. Li, *Adv. Mater.*, 2020, **32**, 2006752.

93 W. Qin, P. Zhang, H. Li, J. W. Y. Lam, Y. Cai, R. T. K. Kwok, J. Qian, W. Zheng and B. Z. Tang, *Chem. Sci.*, 2018, **9**, 2705–2710.

94 Y. Wang, H. Gao, J. Yang, M. Fang, D. Ding, B. Z. Tang and Z. Li, *Adv. Mater.*, 2021, **33**, 2007811.

95 J. Zhi, Q. Zhou, H. Shi, Z. An and W. Huang, *Chem. – Asian J.*, 2020, **15**, 947–957.

96 L. Gu, H. Wu, H. Ma, W. Ye, W. Jia, H. Wang, H. Chen, N. Zhang, D. Wang, C. Qian, Z. An, W. Huang and Y. Zhao, *Nat. Commun.*, 2020, **11**, 944.

97 Y. Lei, W. Dai, J. Guan, S. Guo, F. Ren, Y. Zhou, J. Shi, B. Tong, Z. Cai, J. Zheng and Y. Dong, *Angew. Chem., Int. Ed.*, 2020, **59**, 16054–16060.

98 Y. Li and P. Gao, *Chemosensors*, 2023, **11**, 489.

99 B. Sk and S. Hirata, *Adv. Sci.*, 2024, **11**, 2308897.

100 J. Tan, Q. Li, S. Meng, Y. Li, J. Yang, Y. Ye, Z. Tang, S. Qu and X. Ren, *Adv. Mater.*, 2021, **33**, 2006781.

101 S. Hirata, K. Totani, H. Kaji, M. Vacha, T. Watanabe and C. Adachi, *Adv. Opt. Mater.*, 2013, **1**, 438–442.

102 S. Datta and J. Xu, *ACS Appl. Bio Mater.*, 2023, **6**, 4572–4585.

103 X. Yang, G. I. N. Waterhouse, S. Lu and J. Yu, *Chem. Soc. Rev.*, 2023, **52**, 8005–8058.

104 W. Zhao, Z. He and B. Z. Tang, *Nat. Rev. Mater.*, 2020, **5**, 869–885.

105 D. Malpicci, E. Lucenti, C. Giannini, A. Forni, C. Botta and E. Cariati, *Molecules*, 2021, **26**, 6999.

106 E. Lucenti, A. Forni, C. Botta, L. Carlucci, C. Giannini, D. Marinotto, A. Previtali, S. Righetto and E. Cariati, *J. Phys. Chem. Lett.*, 2017, **8**, 1894–1898.

107 H. Li, L. Lv, K. Yuan, S. Pan and Z. Li, *Sci. Rep.*, 2023, **13**, 12357.

108 S. Cai, X. Yao, H. Ma, H. Shi and Z. An, *Aggregate*, 2023, **4**, e320.

109 S. J. N. Dixit, R. Ghosh and N. Agarwal, *Phys. Chem. Chem. Phys.*, 2025, **27**, 175–181.

110 A. Ahsan, X. Wang, R. Sk, M. Heydari, L. Buimaga-Iarinca, C. Wäckerlin, E. Lucenti, S. Decurtins, E. Cariati, T. A. Jung, U. Aschauer and S.-X. Liu, *J. Phys. Chem. C*, 2023, **127**, 23000–23009.

111 A. Forni, E. Lucenti, C. Botta and E. Cariati, *J. Mater. Chem. C*, 2018, **6**, 4603–4626.

112 D. S. Cati and H. Stoeckli-Evans, *CCDC 227635: CSD Communication*, 2004, DOI: 10.5517/cc7mw2s.

113 T. Itoh, *Chem. Rev.*, 2012, **112**, 4541–4568.

114 M. Kasha, *Faraday Discuss. R. Soc. Chem.*, 1950, **9**, 14–19.

115 S. H. Lee, S. H. Kim, S. K. Kim, J. H. Jung and J. S. Kim, *J. Org. Chem.*, 2005, **70**, 9288–9295.

116 I. Suzuki, M. Ui and A. Yamauchi, *J. Am. Chem. Soc.*, 2006, **128**, 4498–4499.

117 F. M. Winnik, *Chem. Rev.*, 1993, **93**, 587–614.

Open Access Article. Published on 20 January 2025. Downloaded on 1/21/2026 10:55:07 PM. This article is licensed under a Creative Commons Attribution-NonCommercial 3.0 Unported Licence.

118 C. Chen, Z. Chi, K. C. Chong, A. S. Batsanov, Z. Yang, Z. Mao, Z. Yang and B. Liu, *Nat. Mater.*, 2021, **20**, 175–180.
119 C. Chen, K. C. Chong, Y. Pan, G. Qi, S. Xu and B. Liu, *ACS Mater. Lett.*, 2021, **3**, 1081–1087.
120 J. Song, Y. Wang, L. Qu, L. Fang, X. Zhou, Z.-X. Xu, C. Yang, P. Wu and H. Xiang, *J. Phys. Chem. Lett.*, 2022, **13**, 5838–5844.
121 S. Yuan, Y. Zhang, J. Chen, Y. Yu, L. Yue, Q. Sun, H. Zhang, S. Xue and W. Yang, *Adv. Opt. Mater.*, 2022, **10**, 2200090.
122 Y. Zhang, Q. Sun, J. Chen, S. Cui, H. Zhang, S. Xue and W. Yang, *Chem. Eng. J.*, 2022, **447**, 137458.
123 E. Cariati, A. Forni, E. Lucenti, D. Marinotto, A. Previtali, S. Righetto, C. Botta, V. Bold, V. Kravtsov and M. S. Fonari, *Chem. – Asian J.*, 2019, **14**, 853–858.
124 M. S. Fonari, V. C. Kravtsov, V. Bold, E. Lucenti, E. Cariati, D. Marinotto and A. Forni, *Cryst. Growth Des.*, 2021, **21**, 4184–4200.
125 E. Lucenti, E. Cariati, A. Previtali, D. Marinotto, A. Forni, V. Bold, V. C. Kravtsov, M. S. Fonari, S. Galli and L. Carlucci, *Cryst. Growth Des.*, 2019, **19**, 1567–1575.
126 D. Malpicci, E. Lucenti, A. Forni, D. Marinotto, A. Previtali, L. Carlucci, P. Mercandelli, C. Botta, S. Righetto and E. Cariati, *Inorg. Chem. Front.*, 2021, **8**, 1312–1323.
127 A. Forni, E. Cariati, L. Carlucci, E. Lucenti, D. Marinotto, S. Pieraccini and M. Sironi, *Acta Crystallogr., Sect. B:Struct. Sci., Cryst. Eng. Mater.*, 2021, **77**, 865–870.
128 E. Melnic, V. C. Kravtsov, E. Lucenti, E. Cariati, A. Forni, N. Siminel and M. S. Fonari, *New J. Chem.*, 2021, **45**, 9040–9052.
129 D. Malpicci, D. Maver, D. Maggioni, P. Mercandelli, L. Carlucci, E. Cariati, P. Mussini and M. Panigati, *New J. Chem.*, 2023, **47**, 21463–21474.
130 D. Malpicci, D. Blasi, D. Marinotto, A. Forni, E. Cariati, E. Lucenti and L. Carlucci, *Crystals*, 2023, **13**, 149.
131 J.-C. Li, H.-X. Li, H.-Y. Li, W.-J. Gong and J.-P. Lang, *Cryst. Growth Des.*, 2016, **16**, 1617–1625.
132 D. Malpicci, D. Blasi, A. Forni, E. Lucenti, D. Marinotto, M. Formenti, D. Maver, P. Mercandelli, E. Cariati and L. Carlucci, *Eur. J. Inorg. Chem.*, 2024, e202400185.
133 G. Cavallo, P. Metrangolo, R. Milani, T. Pilati, A. Priimagi, G. Resnati and G. Terraneo, *Chem. Rev.*, 2016, **116**, 2478–2601.
134 A. Forni, S. Pieraccini, D. Franchini and M. Sironi, *J. Phys. Chem. A*, 2016, **120**, 9071–9080.
135 A. Forni, S. Pieraccini, S. Rendine, F. Gabas and M. Sironi, *ChemPhysChem*, 2012, **13**, 4224–4234.
136 A. Forni, S. Pieraccini, S. Rendine and M. Sironi, *J. Comput. Chem.*, 2014, **35**, 386–394.
137 Q. J. Shen, X. Pang, X. R. Zhao, H. Y. Gao, H.-L. Sun and W. J. Jin, *CrystEngComm*, 2012, **14**, 5027–5034.
138 P. Smart, Á. Bejarano-Villafuerte, R. M. Hendry and L. Brammer, *CrystEngComm*, 2013, **15**, 3160–3167.
139 V. C. Kravtsov, V. Bold, N. Siminel, Y. Chumakov, M. Gdaniec, E. Lucenti, D. Malpicci, D. Maver and M. S. Fonari, *Cryst. Growth Des.*, 2024, **24**, 4875–4883.
140 V. Kumar, H. Kim, B. Pandey, T. D. James, J. Yoon and E. V. Anslyn, *Chem. Soc. Rev.*, 2023, **52**, 663–704.
141 X. Sun, Y. Wang and Y. Lei, *Chem. Soc. Rev.*, 2015, **44**, 8019–8061.
142 R. Haiges, G. Bélanger-Chabot, S. M. Kaplan and K. O. Christe, *Dalton Trans.*, 2015, **44**, 7586–7594.
143 G. Hervé, C. Roussel and H. Graindorge, *Angew. Chem., Int. Ed.*, 2010, **49**, 3177–3181.
144 P. Peng, N. Ding, C. Zhao, Y. Li, J. Liu, S. Li and S. Pang, *Cryst. Growth Des.*, 2022, **22**, 2158–2167.
145 J. Mei, N. L. C. Leung, R. T. K. Kwok, J. W. Y. Lam and B. Z. Tang, *Chem. Rev.*, 2015, **115**, 11718–11940.
146 W. Xu, M. M. S. Lee, Z. Zhang, H. H. Y. Sung, I. D. Williams, R. T. K. Kwok, J. W. Y. Lam, D. Wang and B. Z. Tang, *Chem. Sci.*, 2019, **10**, 3494–3501.
147 K. K. Ng and G. Zheng, *Chem. Rev.*, 2015, **115**, 11012–11042.
148 F. P. L. Lim and A. V. Dolzhenko, *Eur. J. Med. Chem.*, 2014, **85**, 371–390.
149 M. L. Bochman, K. Paeschke and V. A. Zakian, *Nat. Rev. Genet.*, 2012, **13**, 770–780.
150 S. Marzano, B. Pagano, N. Iaccarino, A. Di Porzio, S. De Tito, E. Vertecchi, E. Salvati, A. Randazzo and J. Amato, *Int. J. Mol. Sci.*, 2021, **22**, 10315.
151 P. Zizza, C. Cingolani, S. Artuso, E. Salvati, A. Rizzo, C. D'Angelo, M. Porru, B. Pagano, J. Amato, A. Randazzo, E. Novellino, A. Stoppacciaro, E. Gilson, G. Stassi, C. Leonetti and A. Biroccio, *Nucleic Acids Res.*, 2016, **44**, 1579–1590.
152 R. Hänsel-Hertsch, J. Spiegel, G. Marsico, D. Tannahill and S. Balasubramanian, *Nat. Protoc.*, 2018, **13**, 551–564.
153 S. Balasubramanian, L. H. Hurley and S. Neidle, *Nat. Rev. Drug Discovery*, 2011, **10**, 261–275.
154 M. Allegretti, A. Fabi, E. Giordani, C. Ercolani, P. Romania, C. Nisticò, S. Gasparro, V. Barberi, M. Ciolina, E. Pescarmona, D. Giannarelli, G. Ciliberto, F. Cognetti and P. Giacomini, *Mol. Cancer*, 2021, **20**, 151.
155 A. R. Duarte, E. Cadoni, A. S. Ressurreição, R. Moreira and A. Paulo, *ChemMedChem*, 2018, **13**, 869–893.
156 T. Santos, G. F. Salgado, E. J. Cabrita and C. Cruz, *Pharmaceuticals*, 2021, **14**, 769.
157 D. Musumeci, J. Amato, P. Zizza, C. Platella, S. Cosconati, C. Cingolani, A. Biroccio, E. Novellino, A. Randazzo, C. Giancola, B. Pagano and D. Montesarchio, *Biochim. Biophys. Acta, Gen. Subj.*, 2017, **1861**, 1341–1352.
158 J. Amato, G. Miglietta, R. Morigi, N. Iaccarino, A. Locatelli, A. Leoni, E. Novellino, B. Pagano, G. Capranico and A. Randazzo, *J. Med. Chem.*, 2020, **63**, 3090–3103.
159 J. Amato, R. Morigi, B. Pagano, A. Pagano, S. Ohnmacht, A. De Magis, Y.-P. Tiang, G. Capranico, A. Locatelli, A. Graziadio, A. Leoni, M. Rambaldi, E. Novellino, S. Neidle and A. Randazzo, *J. Med. Chem.*, 2016, **59**, 5706–5720.
160 J. Amato, C. Platella, S. Iachettini, P. Zizza, D. Musumeci, S. Cosconati, A. Pagano, E. Novellino, A. Biroccio, A. Randazzo, B. Pagano and D. Montesarchio, *Eur. J. Med. Chem.*, 2019, **163**, 295–306.
161 J. Amato, T. W. Madanayake, N. Iaccarino, E. Novellino, A. Randazzo, L. H. Hurley and B. Pagano, *Chem. Commun.*, 2018, **54**, 9442–9445.